Research on Attitude Determination and Step-Length Prediction using Extended Kalman Filter and Artificial Neural Network for Shoe-Type Gait Measurement Device

PhD Thesis

Research on Attitude Determination and Step-Length Prediction using Extended Kalman Filter and Artificial Neural Network for Shoe-Type Gait Measurement Device

Romy Budhi Widodo
14899038

Kyushu Institute of Technology

Graduate School of Life Science and Systems Engineering

Department of Life Science and Systems Engineering

2017

Research on Attitude Determination and Step-Length Prediction using Extended Kalman Filter and Artificial Neural Network for Shoe-Type Gait Measurement Device

by
Romy Budhi Widodo
Student ID number: 14899038

Supervisor: Prof. Chikamune Wada

Abstract

The information of the spatial and temporal gait parameters is useful for the physicians and physical therapists for determining a patient's gait condition. For that purpose, we have developed a shoe-type measurement device to measure several gait parameters. This paper discusses the improvement of a shoe-type measurement device that consists of: 1) the elimination of the effect of external acceleration in attitude calculation; 2) the redesign of ultrasonic sensors positioning in order to predict step-length; and 3) information regarding the plantar center of pressure when people walk. The first improvement resulted from the sensors' fusion, using the extended Kalman filter (EKF) with the proposed external acceleration compensation. The result of attitude determination shows an improvement in performance (mean square error) over the conventional EKF. The second improvement was made by using acoustic simulation and the implementation of the sensors' positions to the actual shoes. The artificial neural network was used to accommodate the step-length prediction using two-layer architecture. The results of the predictive performance of step-length demonstrate an improvement in distance error compared to the previous study. The third improvement was made by redesigning the position of the pressure sensors, calibrating sensors, and calculating the center of pressure using tactile force sensors.

This page intentionally left blank

Acknowledgement

First and foremost, my sincerest thanks to our Father in heaven. I realized how true His blessing in all of my life. It is a humbling experience to acknowledge those people who have helped along the journey of my doctorate degree.

I would like to express my appreciation to my supervisor Professor Chikamune Wada, who has convincingly conveyed a spirit of doing PhD under his supervision. Without his guidance and persistent help this dissertation would not have been possible. Also, I would like to express my appreciation to supervisory committee who give me suggestions to improve the dissertation and give me chance to continually try in this dissertation: Professor Tomohiro Shibata, Professor Hiroyuki Miyamoto, Professor Hiroaki Wagatsuma, and last but not least is Professor Kazuto Takashima.

To my school staff member since the beginning of my journey: Ms. Yasuko Nagamatsu, Ms. Naoko Matsuura, Mr. Atsuki Matsubara, Ms. Haruka Hara, and Ms. Teng Teng Lim, who have help me arrange all the administration during my journey including the scholarship and all student activities; Ms. Yuko Tamari, who arrange the teaching assistant administration for us; Ms. Miho Fujimura, who gave me chance in arrange conference travel, book buying, and journal paper expenses; Ms. Megumi Oga, who gave me the best survey about graduation certificate; and Ms. Michiaki Mori, who arrange the administration during of my research assistant. I'd like to give a warm and special thank you to all for your best services to us.

I'd like to extend a most sincere thank you to Professor Kiyohiko Nunokawa in TIU, Japan, who gave me chance the internship program under his supervision and gave spirit to continue the journey: "Hang in there, and you can do it."

To my laboratory senior and colleague members: Mr. Souta Nakano; who gave me spirit in continuing this journey; Mr. Takayuki Nagasaki, who gave me help and discussion during my journey; Mr. Takeshi Joyashiki; who give a wonderful words "fear is often worse than the danger itself" and give me discussion during the journey especially on weekends. My colleagues: Mr. Hiroyuki Kuraoka and Ms. Jin Fang; I hope we can meet again on the other occasions and all the best for all of you. My colleague Mr. Shogo Okamatsu, thank you for serving us during the last experiment. My colleagues: Mr.

Fukushima, Mr. Junya Hirakawa, Mr. Ahmed Almassri, Mr. Watcharin Tangsuksant, Mr. Tsuyoshi Uezono, Mr. Ryuya Nagasako, Mr. Nishisako, Ms. Sayaka Wada, Mr. Fukumoto, all the best for you all and success for your study and career in the next future. To my seniors: Mr. Suguru Ikeda, Mr. Takigawa, Mr. Edayoshi, Mr. Handa, Mr. Ikeda, Ms. Yasaka, Mr. Arima, Mr. Oda, Ms. Chen, Mr. Matsusawa, Mr. Eguchi, Mr. Tomiyama, Mr. Kodama, Mr. Nishimura, Mr. Kishimoto, and Mr. Yamaguchi. For my seniors: thank you for your guidance and mentoring during my journey. For my colleagues: thank you all for being part of my journey and success for all of you in your career.

Thank you to Mr. Kazuyuki Shiraishi, who gave me spiritual advice during my journey. My friends, Tanaka family, Mr. Higashi Yama, Mr. Hamasaki, all friends in Asahi and Pinokio, thank you for sharing with me your love and your warmth during my journey.

Thank you to my colleagues in Ma Chung university and Harapan Bangsa Sejahera Foundation, including my seniors: Mr. Nagawidjaja, Ms. Leenawaty, Mr. Yufra, Professor Sadtono, Mr. Peter P., Ms. Anna T., Mr. D. Ginting, Professor Handiyo, Mr. Putu I., Mr. Renald S., Mr. Yudhi, Ms. Yudhi, Mr. Sahala M., Mr. Teguh, Mr. Sunday N., Ms. Angel, Ms. Novie, Mr. Tomo, Mr. Jerufael, Mr. Fris, Mr. Budhy, Ms. Putu P., Mr. Sugeng R., Ms. Titik R, Mr. Teddy M., Mr. Windra, Mr. Hendry, Mr. Lucky, Mr. Oesman, Ms. Kestrilia, Mr. Rudy S., Ms. Meifry, Mr. Subiyanto, Mr. Soetam, Mr. Ronald, Ms. Yuliana S., and all members that cannot be mentioned one by one here; thank you for your encouragement.

Last but not least, will be stayed in my heart, thank you to my parents, my mother -throughout the years, you have always been by my side; my dad who was often in my thought in this live-you are missed; my wife Ellia; my sons E.Horsa W. and Peter R. W.; my daughter Elita V. W., all of Widodo family for your patience, your pray, your encouragement and supported me along the way. Thank you.

Wakamatsu, March 2017

List of Figures

List of Tables

Contents

This page intentionally left blank

1. Introduction

1.1 Background of Study

In order to assess spatial and temporal gait data in rehabilitation centers or hospitals, doctors or physical therapists use visual investigation. In some cases, the medic also uses a motion capturing system for a detailed investigation. The reliability and performance of gait assessment using visual investigation is dependent on the expertise of medical personnel. Therefore, data quality cannot be determined from using visual investigation. A motion capturing system, on the other hand, promises the accuracy of the investigation. However, motion capturing systems are not available in every clinic or hospital, and are categorized as costly instruments. The limitation of space in which a patient can move and still be captured by the system is also a shortcoming. To overcome this situation the medics needs a measurement that is independent from this space limitation; therefore, the measurement system that was attached to shoes, *measurement-attach shoe*, was hypothesized as an alternative to solve the problem.

Recently, more and more research has been driven by interest in a gait assessment system using *measurement-attach shoe*. Many terms have been used to describe the measurement apparatus related to gait measurement; previous studies use terms of shoe-type measurement device [1], GaitShoes system [2], foot-worn sensing [3], and on-shoe wearable sensor [4]. In this paper, we will use the term “shoe-type measurement device” to refer to a device that transmitted raw data of walking activity wirelessly to a personal computer. The studies that use “foot-worn sensing” [3] and “on-shoe wearable sensor” [4] concentrate on using inertial sensor (IMU) data to assess spatial parameters of gait, but the discussion of foot pressure as one part of gait analysis is not on hand. The GaitShoes system [2] and our previous shoe-type measurement device have the same sensors, but these have a different purpose; the purpose of the GaitShoes system [2] is to evaluate the patient’s walk, whereas the purpose of our previous system was to give the user information about the feet during walking.

Problems of balance and gait are associated with immobility and falls, which reduced the quality of life. An unhealthy pattern of gait relies on a complex and simultaneous interaction among the motor system, sensory control, and cognitive functions. A population-based study has shown that gait disorders among persons: 1) 15% of 60-years-olds; 2) 35% of 70-years olds, and 3) 80% of 85-years olds [5]. As pitch angle of foot directly related to the ankle angle, two proposed functions of an attitude angle, especially on the sagittal plane (pitch angle) of a shoe-type gait measurement device will be described, i.e. gait alterations monitoring and the

classification of gait disturbances.

First, the information about ankle angle is important for elderly gait alteration monitoring to prevent falls and to design an exercise program activities strengthening related ankle muscle [6]. It was found that gait performance in the elderly was limited by both subtle hip flexion contracture and ankle plantarflexor concentric weakness [6]. The age-associated reduction in peak angle plantarflexion was also found on the other study. The measurement of ankle angle on corresponding study used infrared reflective markers, it indicates that the measurement should in the specific measurement room. It is better that the monitoring is possible in every place that it needs, therefore, the shoe-type measurement device is necessary.

Second, the information about ankle angle could be used as core gait feature in classification of gait disturbances. The classification of gait disturbance as in Jahn [5] and Snijders [7], need gait pattern or core gait features as a beginning of classification such as step-length and ankle angle. Continuing with clinical tests and accompanying findings. The gait-pattern indicated by ankle motion, knee motion, and hip motion also found in Kerrigan et al. [6]. The classification of idiopathic toe walking (ITW) also used kinematic pattern of ankle angle as studied by Alvarez et al. [8].

The attitude information for the purpose of ankle angle determination was prone to errors due to numerical integration, the lack of an estimator, and the effect of external acceleration which may also have influenced the attitude estimation. The contained several drawbacks upon which the current study will have the opportunity to improve. The first is attitude information (roll and pitch angle) of human walk. In addition on the previous study [1], the ultrasonic receivers and transmitters sensors are perishable and fragile, so the measurement of step-length is prone to error. The term *step-length* refers to the distance from the heel of the trailing limb to the heel of the leading one [9].

1.2 Purposes of the Study

Based on the above background, the objective of this study is to develop the shoe-type gait measurement device in order to give information about the feet during walking to the medics, so as to improve the quality of life. The list of details is as follows:

- To build and analyze a shoe-type measurement device by focusing the work on three parts: IMU, ultrasonic sensors, and pressure sensors.

- The work in the IMU component will be concentrated on compensating for the influence of external acceleration in attitude estimation. The results of the IMU work will be validated against results from a motion capturing system.

- The work on ultrasonic sensors will focus on the improvement of step-length prediction of human walking, including the simulation of ultrasonic sensors to implement on actual shoes. The results of the step-length prediction work will also be validated against a motion capturing system.

- The work on pressure sensors will aim to calibrate the tactile force sensors in each insole board of the shoe-type measurement device in order to give some information on the center of pressure of the plantar surface during walking. The result of the in-shoe center of pressure will be validated against a force platform system.

1.3 The Present Configuration of the Paper

This paper is organized in six chapters. The content of each chapter is as follows:

Chapter 1 explains the study's background with a brief literature review and discusses the purposes of the study.

Chapter 2 presents related previous studies, discusses the problems involved in these previous studies, and proposes methods for solving those problems. The discussion is divided into three parts: 1) the issue of attitude determination, 2) the issue of step-length prediction, and 3) the issue of pressure sensing in a shoe-type measurement device.

Chapter 3 presents the theoretical concept of attitude (roll and pitch angle) sensing, the proposed external acceleration compensation and modified-extended Kalman Filter (EKF) for determining attitude. This chapter is divided into six parts: the first part of the chapter explains the representation of the rotational kinematic equation in a directional cosine matrix, Euler angles, and Quaternions. The second part of the chapter includes the testing of the theoretical concept as a preliminary result of attitude determination using an accelerometer, a gyro, and a sensor fusion, accompanied by explanations. The third part will discuss about how to determine the position of inertial sensor on the shoe including the specification of the inertial sensor. The fourth part of the chapter explains the proposed external acceleration compensation model and its implementation for EKF. Also in the fourth part, three other modes from previous studies are presented as a comparison, thereby finally resulting in five modes. *Mode 1* is the standard EKF

without compensating for external acceleration. *Mode 2* is the EKF containing the proposed external acceleration compensation, with a pre-processing technique for accelerometer data using the proposed model. *Mode 3* is derived from a *two-step EKF* that adjusts the measurement noise covariance using the *weighted-switching* approach [10]. *Mode 4* is the quaternion-based EKF, which uses a *threshold-based* approach to set the measurement error covariance [16]. *Mode 5* uses an unscented Kalman filter (UKF) [17]. This method is threshold-based, combined with a softened part of measurement noise covariance matrix adjustment. The fifth part of Chapter 3 explains the implementation results, including various test conditions, test setup, and test results of the five modes. The sixth part discusses the experimental results of each mode, the limitations of the study, and the conclusions.

Chapter 4 explains human step-length prediction using ultrasonic sensors attached on shoe soles. This chapter is divided into four parts. The discussion begins with the simulation to find the optimum sensors' numbers, position, and angles. The second part of this chapter contains the results of the simulation implemented on the actual shoe-type measurement device. The third part contains a step-length prediction that uses two architecture models of an artificial neural network to find the optimum result of prediction. The last part of this chapter explains the discussion, limitations, and conclusions.

To assess the pressure distribution when people walk, Chapter 5 is divided into five parts that explains the background of pressure sensor selection, the design of the sensors' placement, the calibration of the load cell as a reference apparatus, the sensors' calibration procedure, and the validation of the experimental result using force platform system. The first part of this chapter explains the technology behind pressure sensing, leading up to the decision to select a tactile-based sensor for shoe-type measurement device. The second part discusses the calibration of the load cell as a reference for calibrating the tactile-based sensor. In the third part, in order to assess the pressure distribution, each sensor was calibrated to SI units using the polynomial of degree-1, degree-2, and degree-3. The fourth part of this chapter explains the calculation of the center of pressure acting on a foot plantar; the force platform is used to validate the result of experiment. Finally the chapter is concluded with a discussion about the results of the center of pressure and the limitation.

Chapter 6 includes the conclusion in addition to future work direction.

The outline of this dissertation is as follows:

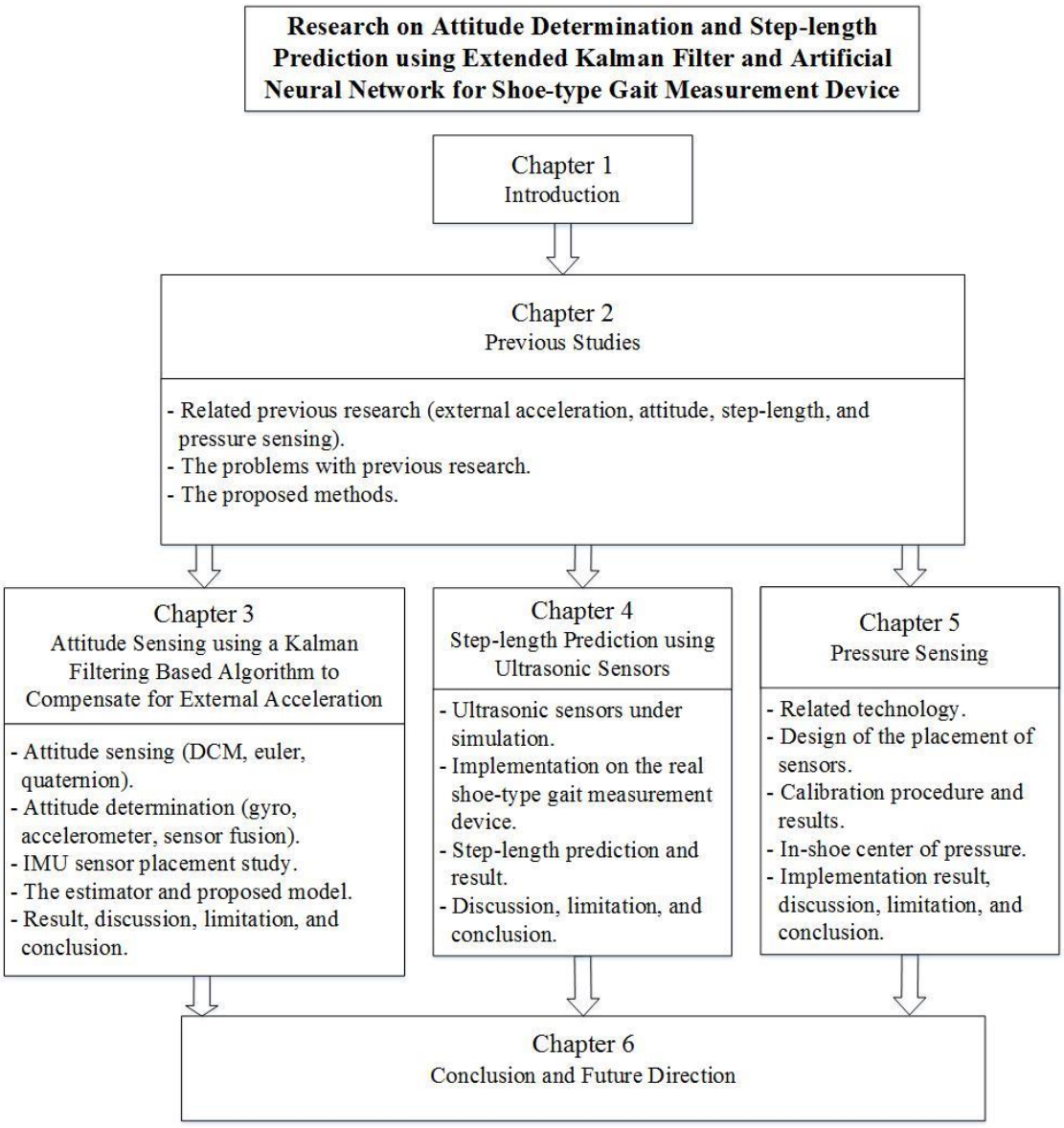

Figure 1.1 Dissertation chapter overview.

This page intentionally left blank

2. Previous Studies

This chapter discusses related previous studies, the concerning problems of the previous studies, and proposals to mediate the limitations therein.

2.1 Related Previous Research

2.1.1 External Acceleration and Attitude Determination

The term external acceleration in this study refers to another forces sensed by the accelerometer aside from the gravitational acceleration. An accelerometer measures specific forces that contain the gravitational acceleration, including the effects of velocity and the angular velocity in each axis [31]. In others studies, the term of external acceleration recently has been used [10, 11, 12], while others used terms with the same meaning as external acceleration: “acceleration” only in Luinge et al. [13], “bodily acceleration” in Sabatini et al. [16], and “disturbing motion, such as mechanical vibration, wind effects, and human activity,” in Groves [14]. Figure 2.1 illustrates the variety of forces that were measured by an accelerometer: a) gravitational acceleration, which is measured purely when in static condition; b) the effects of velocity, and c) the effects of angular velocity.

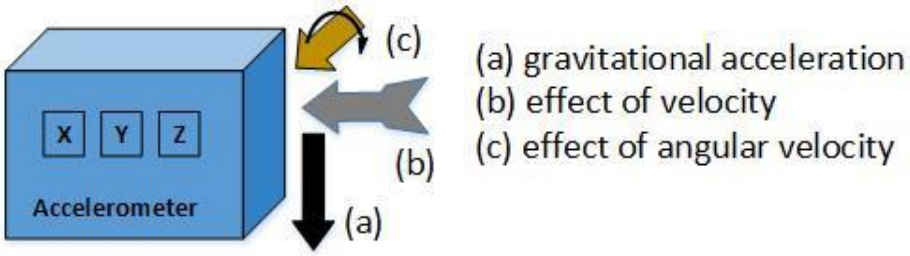

Figure 2.1 Forces measures by an accelerometer.

The IMU typically determines attitude, the roll and pitch while walking, by fusing accelerometer and gyro data. However, the most notable disturbance of attitude determination is external acceleration [10], which is caused by a change of velocity in magnitude or direction [14]. The attitude solution provided by the gyro is prone to being unbounded, to bias, and to random-walk errors. In one study [2], the pitch angle provided by integrating the gyro signal required a special signal processing technique to compensate for the drift. In static or slow movement, the accelerometer measures roll and pitch by leveling in order to correct the gyro-unbounded error. This is due to the trustworthiness of the gravitational measurement. Therefore, a proper fusion of IMU data and the algorithm to compensate for external acceleration is needed to overcome

the shortcomings of each sensor and the effects of external acceleration. The resulting fusion technique evolved along two major paths: one approach incorporates the use of a Kalman filter [10, 15-17], while the other algorithm consists of a complementary filter [18, 19].

In other studies, methods to deal with external acceleration can be categorized into two major paths: the threshold-based approach and the acceleration model based approach. The threshold-based approach works based on the switching algorithm, for example, the method works when the norm of accelerometer data in each axis exceeds a threshold value. Based on our reference studies, Table 2.1 represents threshold-based conditions from other reports.

Table 2.1 Threshold-based approach in the literature

Reference	Threshold condition	Estimate parameter	Action
Suh et al. [10]	$\left\|f_x^2 + f_y^2 + f_z^2 - 1\right\| > \delta$ f_x , f_y , f_z : accelerometer output. δ : threshold.	direct	Modify measurement noise covariance matrix
Sabatini [16]	${}^{R}\sigma_a^2 = \begin{cases} \sigma_a^2, \left\|\left\|\mathbf{a}_{j+1}\right\| - \left\|\mathbf{g}\right\|\right\| < \varepsilon_{th} & \forall j \in [k - k_a, k] \\ \infty, otherwise \end{cases}$ ${}^{R}\sigma_m^2 = \begin{cases} \sigma_m^2, \left\|\left\|\mathbf{m}_{k+1}\right\| - \left\|\mathbf{h}\right\|\right\| < \varepsilon_m \cap \left\|\hat{\theta}_{dip} - \theta_{dip}\right\| < \varepsilon_{dip} \\ \infty, otherwise \end{cases}$ $\varepsilon_{th}, \varepsilon_m$: accelerometer and magnetometer threshold. ${}^{R}\sigma_a^2, {}^{R}\sigma_m^2$: measurement variance $\mathbf{h}$: earth's magnetic field a_j, m_k: accelerometer and magnetometer output. θ_{dip}, dip angle: angle formed by the earth's magnetic field relative to the horizontal.	direct	Modify measurement noise covariance matrix

Table 2.1 continued			
Harada et al. [17]	$\left\|\left\|\mathbf{a}_{\mathrm{k}}\right\|-\left\|\mathbf{g}\right\|\right\|<\varepsilon_{th}$ $\sigma_{a,k}^2=\sigma_{a0}^2+\alpha_a\left\|{}^{\mathrm{b}}\mathbf{a}_{\mathrm{k}}-{}^{b}\mathbf{g}_k\right\|^2$ $\sigma_{a,k}^2$: measurement variance $\alpha_a\left\|{}^{\mathrm{b}}\mathbf{a}_{\mathrm{k}}-{}^{b}\mathbf{g}_k\right\|^2$: softened part ${}^{b}\mathbf{g}_k$: predicted acceleration	direct	Modify measurement noise covariance matrix
Suh [11]	No external acceleration mode: $if\ \max_{\mathrm{i}}(\lambda_{i,j}-\mu_{i,j})<\gamma\ (\mathrm{j}=\mathrm{k},\mathrm{k}-1,\ldots,\mathrm{k}-\mathrm{M}_2)\rightarrow\hat{Q}_{ab,k}=0$ External acceleration mode: $\hat{Q}_{ab,k}=\sum_{i=1}^{3}\max(\lambda_{i,k}-\mu_{i,k},0)u_{i,k}u'_{i,k}$ where $\mu_{i,k}\underline{\underline{\Delta}}u'_{i,k}\left(H_{a,k}P_k^{-}H'_{a,k}+R_a\right)u_{i,k}$ $\hat{Q}_{ab,k}$: time-varying covariance of external acceleration a_b. $\lambda_{i,k}$: eigen value of the approximation of measurement error covariance matrix.	indirect	Time varying covariance of external acceleration prediction.

As shown in Table 2.1, Suh et al. [10], Sabatini [16], and Harada et al. [17], proposed the adapted measurement noise covariance matrix in Kalman filtering to overcome certain disturbances, including external acceleration. Suh et al. [10] adapted an algorithm that was based on the weighted-switching approach. In contrast, Sabatini [16] used a threshold-based approach, while Harada et al. [17] proposed a threshold-based approach combined with softening. Suh [11] proposed a time-varying covariance of external acceleration predictions, which is different from the previous three approaches. Another difference between the aforementioned literature [10, 16, 17] and Suh et al. [11], is the former used the direct method in Kalman filtering, in which the estimation parameter is the same as the attitude parameter itself, or parameters from inertial sensors. However, Suh [11] used indirect Kalman filtering, which used the error of the attitude parameter. The advantage of an indirect filter is that the state dimension is smaller and its response is fast [11].

The second approach to deal with external acceleration is the acceleration-model approach, which does not rely on conditional switching. Luinge et al. [13] proposed the model of the acceleration of a body segment as low pass filtered white noise. The estimator is categorized as indirect because it estimates the orientation error. Lee et al. [12] used the same model of external acceleration as in Luinge et al., but the difference is in the structure of Kalman filtering. Lee et al. used linear Kalman direct filtering; whereas Luinge et al. employed linear Kalman indirect filtering. Both Lee [12] and Luinge [13] utilized the external acceleration model as in the Eq. (2-1):

$$ {}^{G}\mathbf{a}_{t} = c_{a} . {}^{G}\mathbf{a}_{t-1} + \mathbf{w}_{a,t} \qquad (2\text{-}1) $$

where c_a denotes a dimensionless constant between 0 and 1 that determines the cutoff frequency; $\mathbf{w}_{a,t}$ is the time-varying error of the acceleration model.

Inspired by the previous studies, especially regarding the external acceleration model approach; the present study aimed to develop a new algorithm. The algorithm extracted external acceleration from the accelerometer signal with a model, and used it to adjust the measurement noise covariance matrix in an attitude estimation based on the extended Kalman filter (EKF) [20]. In this study, the proposed algorithm is based on the disturbance rejection model, as will be explained in detail in subsection 3.4.2. Although Lee et al. [12] and Luinge et al. [13] use the acceleration model approach, our focus is to develop a new approach that is different from the aforementioned models and compared explicitly with the threshold-based approach. The comparison with the work of Luinge et al. and Lee et al. was not executed due to the different parameter estimations and estimator types. Table 2.2 describes the consideration of other literature selections as a comparison for our study; the ☑ mark indicates the possibility for comparison between the proposed method and related previous literature. Section 3.4 will discuss the standard extended Kalman filtering as *Mode 1*, the proposed algorithm as *Mode 2*, and the comparison using the proposed method by Suh et al. [10] as *Mode 3*; the proposed method by Sabatini [16] as *Mode 4*; and the proposed method by Harada et al. [17] as *Mode 5*.

Table 2.2 The consideration of comparison selection.

Reference	Parameter estimation	Estimator type	Approach	Action	Mark
This study	Direct	Non linear	Model – based	Modify the measurement noise covariance matrix.	
Luinge et al. [13]	Indirect	Linear	Model – based	Modify the measurement noise covariance matrix.	☒
Lee et al. [12]	Direct	Linear	Model – based	Modify the measurement noise covariance matrix.	☒
Suh et al. [10]	Direct	Non linear	Threshold – based	Modify the measurement noise covariance matrix.	☑
Sabatini [16]	Direct	Non linear	Threshold – based	Modify the measurement noise covariance matrix.	☑
Harada et al. [17]	Direct	Non linear	Threshold – based	Modify the measurement noise covariance matrix	☑
Suh [11]	Indirect	Linear	Threshold – based	Time varying covariance of external acceleration prediction.	☒

2.1.2 Step-Length

Step-length measurement as a spatial gait parameter is useful for physicians and physical therapists to determine the patient's gait condition. For that purpose, the previous study in [1] and [41] developed a shoe-type measurement device which one of the specifications is to measure the step-length. The previously designed shoe contains ultrasonic receivers and transmitters, pressure sensors, and IMU. For step-length prediction, it uses seven ultrasonic transmitters (Tx) and twelve receivers (Rx). The sensors are perishable and fragile, so the measurement of gait parameters is prone to error. The step-length was measured by integrating the ultrasonic sensors and gyro data using a particle filter method [41]. In order to streamline the sensors and reduce their number, a simulation technique was needed before implementation. Using the new position, number, and angle of ultrasonic sensors determined from the simulation [21], a method to process the distance data from the ultrasonic receivers was needed to predict the step-length [22]. Therefore, the simulation and step-length prediction method are a challenge in this study. Another study about step-length prediction uses inertial sensors; however, the complexity of inertial sensor data processing requires more computational time [39]. Another step-length prediction method is proposed by Terrier, et al. [53], and

uses DGPS (differential global positioning system); however, GPS has shortcomings such as high cost and its recommendation for outdoor analysis.

2.1.3 Pressure Sensing

As one of the aims of a shoe-type measurement device is to measure the pressure distribution, embedding a pressure distribution sensor sheet into shoe insoles makes measurement possible without space limitations. Fabrication products such as the Pedar® system (Novel Co.,Ltd.) are accurate and reliable pressure distribution measuring systems for monitoring local loads between the foot and the shoe. The other such product is F-Scan II® by Nitta, Inc., Japan and ParoTec® by Paromed, Germany. Using these fabrication products on the shoe-type measurement device significantly raises the cost of the shoes, and data integration with other sensors such as IMU and ultrasonic sensor from other part of the shoes might become more difficult.

When people walk, their foot pressure distribution information is one of the important indicators for doctors or physical therapists. It is important to diagnose foot problems at an early stage to prevent injury [57]. One of the previous studies uses force sensitive resistors (FSR) in order to assess heel-strike timing, toe-off timing, and force distribution [2]. For gait analysis, the center of pressure (CoP) must be taken into account; this information is not available in the previous study. Another study introduces the textile fabric sensor array to measure mean pressure, peak pressure, CoP, and shift speed of CoP [58]. However, the sensor scopes were only located in the heel and forefoot areas, and the study failed to report the trajectory of CoP when people walk. Another study used CoP calculation to balance the exoskeleton for paraplegic patients [59]. However, only two sensors were used on the heel and forefoot, causing lower spatial sensitivity in CoP.

The present study aims to improve the pressure sensor placement and design from the previous studies [1, 41, 58, 59]. The estimation of CoP is also a challenge this study hopes to solve, along with the determination of the CoP trajectory. This information is primarily based on the related technology that should be chosen, how to arrange the placement of force sensors in the insole board, the capacity of the sensors, and the calibration of the sensors.

2.2 The Problems with Previous Research

From the previous section, the problems can be summarized as follows:

- The attitude information of human walk is prone to errors due to numerical integration, the lack of an estimator, and the effect of external acceleration, which reduces the performance of attitude estimation.

- The previously designed shoe contains ultrasonic receivers and transmitters; the sensors are perishable and fragile, so the measurement of step length is prone to error. The number, positions, and angles of the sensors should be redesigned and implemented into the actual shoes as well as the method to determine the step-length.

- The information of foot plantar pressure is important to diagnose foot problems. Other studies have reported the CoP calculation of in-shoe measurement systems; however, the sensor placement and the number of sensors need to be reconsidered.

- There is no complete discussion about the integration of attitude estimation, step-length prediction, and center of pressure measurement in the measurement-attach shoe research.

2.3 The Proposed Method

The method for attitude determination through sensor fusion will be developed with a deepened focus on compensating for external acceleration using a model-based approach. The sensor fusion technique using an extended Kalman filter will be presented using the proposed process and measurement model. The compensation for the external acceleration using the proposed model will be used to modify the measurement noise covariance matrix.

The previous positions of the ultrasonic sensors will be redesigned to increase the performance of step-length prediction. On the first step, the ultrasonic acoustic wave will be simulated using acoustic simulation software in order to find the ideal number, angle, and position of the ultrasonic sensors in the scope of human walking. The second step is implementation in actual shoes and processing the data from the ultrasonic sensors using an artificial neural network to determine the step-length.

To sense the pressure of the foot plantar, the present study's approach is to redesign the sensor placement according to anatomical foot areas. In the second step, each sensor will be calibrated to accommodate the person's body weight. Thirdly, information about

the center of pressure trajectory will be presented when the user walks using this shoe-type measurement device.

3. Attitude Sensing using a Kalman Filtering Based Algorithm to Compensate for External Acceleration

This chapter includes four sections. First, the representation of attitude using direction cosine matrices, Euler angles, and quaternions will be presented. Second, the pros and cons of attitude sensing using a gyro, an accelerometer, and a fusion of gyro and accelerometer data will be discussed. Third, since the application for attitude sensing in this study is for a shoe-type measurement device, the conducted study about the inertial sensor's placement on the shoe is substantial. The study of inertial sensor placement and its specification was included in this part. Fourth, the use of an extended Kalman filtering technique and the proposed external acceleration compensation model will be discussed.

3.1 Attitude Sensing

There are many ways to describe attitude mathematically, such as direction cosine matrices, Euler angles, and quaternions [29]. Each of these methods has both advantages and shortcomings depending on perspectives, such as reliability, accuracy, computational efforts, number of parameters, and approximation error. To express an attitude, a reference is needed; in this discussion the reference frame is denoted by *I*, and the body or body-fixed frame, denoted by *B*, is attached to the object [30]. In application, the body frame is fixed to the sensor and translates or rotates along with the sensor. Ultimately, the attitude of an object is represented as the attitude of the object frame relative to the reference frame. The attitude of an object is one part of the rotational kinematic equation. This section will discuss the rotational kinematic equation that contains the attitude parameter according to each of the three representations: directional cosine matrix, Euler angles, and quaternions.

3.1.1 Direction Cosine Matrix

The representation of a two-dimensional frame is easier to understand than a three-dimensional one, as shown in Fig. 3.1; by coinciding two origins from the reference and body frame, the attitudes of the frames are distinguished more clearly.

The presentation of a direction cosine matrix or rotational matrix is a 2 by 2 matrix and a 3 by 3 matrix for two- and three-dimensional frames, respectively. The relative attitude of frame *B* with respect to frame *I* for two dimensional frames as in Eq. (3-1) and three-dimensional frames as in Eq. (3-2) is:

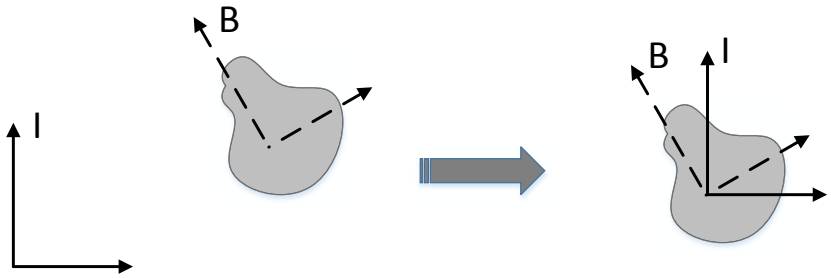

(a) (b)

Figure 3.1 Two-dimensional frame**:** (a) reference and body frame; (b) coinciding two origins but relative attitude remains the same

$$C^{B/I} = \begin{bmatrix} C_{11} & C_{12} \\ C_{21} & C_{22} \end{bmatrix} \tag{3-1}$$

$$C^{B/I} = \begin{bmatrix} C_{11} & C_{12} & C_{13} \\ C_{21} & C_{22} & C_{23} \\ C_{31} & C_{32} & C_{33} \end{bmatrix} \tag{3-2}$$

Equations (3-1) and (3-2) indicate $C^{I/B}$ as the opposite viewpoint, and the matrix $C^{I/B}$ is the transposition of matrix Eqs. (3-1) and (3-2); this is because the direction cosine matrix is an orthonormal matrix. Equations (3-1) and (3-2) represent a mathematical array, and the physical information such as attitude is not seen explicitly; that's why in this case parameters are needed to express the information about attitude. Most sets of parameters consists of three or four parameters; any number of parameters less than three is not enough to fully describe a direction cosine matrix, and a number more than four likely contains redundancy [30]. The most frequently used attitude parameter is Euler angles and quaternions consisting of three and four parameters, respectively. The form of Eq. (3-3) represents the composed directional cosine matrix of the Euler and quaternions parameters.

$$\begin{aligned} C^{B/I} &= C^{B/I}(\phi, \theta, \psi) \\ &= C^{B/I}(q_1, q_2, q_3, q_4) \end{aligned} \tag{3-3}$$

To represent the rotational kinematic, this paper uses an angular velocity notation, $\vec{\omega}^{B/I}$, which is the relative angular velocity of frame *B* with respect to frame *I*. The equation of motion is a first order ordinary differential equation; therefore, the change in

the direction cosine matrix can be represented as the following:

$$\begin{bmatrix} \dot{C}_{11} & \dot{C}_{12} & \dot{C}_{13} \\ \dot{C}_{21} & \dot{C}_{22} & \dot{C}_{23} \\ \dot{C}_{31} & \dot{C}_{32} & \dot{C}_{33} \end{bmatrix} = \begin{bmatrix} 0 & \omega_z & -\omega_y \\ -\omega_z & 0 & \omega_x \\ \omega_y & -\omega_x & 0 \end{bmatrix} \begin{bmatrix} C_{11} & C_{12} & C_{13} \\ C_{21} & C_{22} & C_{23} \\ C_{31} & C_{32} & C_{33} \end{bmatrix} \tag{3-4}$$

where ω_x, ω_y, and ω_z are the angular velocity in each axis in the body frame.

3.1.2 Euler Angles

The Euler angles actually consist of three angles that correspond to three rotations of the reference frame. Figure 3.2 presents two three-dimensional frames of reference, with an IMU as a body object in this figure. By rotating frame *I* about the X axis, Y axis, and Z axis, it is possible to make it coincide with frame *B*. The sequence of rotation is not unique, but there is a rule of thumb to decide the sequence: the same rotation about the same axis as the adjacent rotation is not counted as a possible rotation. Therefore, there will be 12 possibilities of rotation as in Table 3.1 [30]; the discussion in this study will use the sequence Z→Y→X. Corresponding to Euler angles yaw (ψ), pitch (θ), and roll (ϕ), the direction cosine matrix of rotational on each axis is as follows:

$$C_X = C^{B/I}(\phi) = \begin{bmatrix} 1 & 0 & 0 \\ 0 & \cos\phi & \sin\phi \\ 0 & -\sin\phi & \cos\phi \end{bmatrix} \tag{3-5}$$

$$C_Y = C^{B/I}(\theta) = \begin{bmatrix} \cos\theta & 0 & -\sin\theta \\ 0 & 1 & 0 \\ \sin\theta & 0 & \cos\theta \end{bmatrix} \tag{3-6}$$

$$C_Z = C^{B/I}(\psi) = \begin{bmatrix} \cos\psi & \sin\psi & 0 \\ -\sin\psi & \cos\psi & 0 \\ 0 & 0 & 1 \end{bmatrix} \tag{3-7}$$

Table 3.1 All possible sequences of rotational axis in Euler angle

No	**1st rotation**	**2nd rotation**	**3rd rotation**	**Rotation sequence**
1	X	Y	Z	X→Y→Z
2			X	X→Y→X
3		Z	X	X→Z→X
4			Y	X→Z→Y
5	Y	X	Y	Y→X→Y
6			Z	Y→X→Z
7		Z	X	Y→Z→X
8			Y	Y→Z→Y
9	Z	X	Y	Z→X→Y
10			Z	Z→X→Z
11		Y	Z	Z→Y→Z
12			X	Z→Y→X

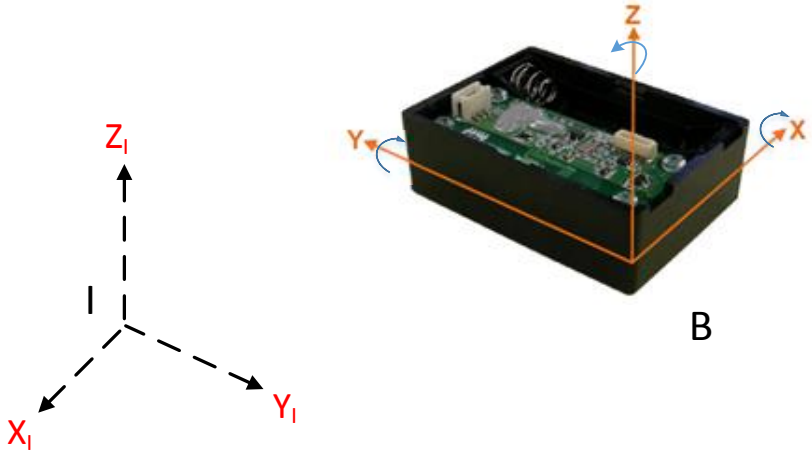

Figure 3.2 Two three-dimensional frames of reference: reference frame (*I*) and body/sensor frame (*B*)

The well-known direction cosine matrix, with the function of rotational order about the Z, Y, and X axis is as follows:

$$C^{I/B}(\phi,\theta,\psi) = \begin{pmatrix} C_X(\phi) & C_Y(\theta) & C_Z(\psi) \end{pmatrix}^T$$

$$C^{I/B}(\phi,\theta,\psi) = \begin{bmatrix} c\theta\, c\psi & -c\phi\, s\psi + s\phi\, s\theta\, c\psi & s\phi\, s\psi + c\phi\, s\theta\, c\psi \\ c\theta\, s\psi & c\phi\, c\psi + s\phi\, s\theta\, s\psi & -s\phi\, c\psi + c\phi\, s\theta\, s\psi \\ -s\theta & s\phi\, c\theta & c\phi\, c\theta \end{bmatrix} \quad (3\text{-}8)$$

where s and c are the short forms of sine and cosine, respectively. It seen that every element of the matrix is composed of functions of the Euler angles.

The kinematic equation for the previous Euler angles with the rotational sequence is Z→Y→X is as follows:

$$\begin{bmatrix} \dot{\phi} \\ \dot{\theta} \\ \dot{\psi} \end{bmatrix} = \frac{1}{\cos\theta} \begin{bmatrix} \cos\theta & \sin\phi\sin\theta & \cos\phi\sin\theta \\ 0 & \cos\phi\cos\theta & -\sin\phi\cos\theta \\ 0 & \sin\phi & \cos\phi \end{bmatrix} \begin{bmatrix} \omega_x \\ \omega_y \\ \omega_z \end{bmatrix} \quad (3\text{-}9)$$

From Eq. (3-9), the singular point occurs when $\theta = \pm 90^o$; this means that the attitude cannot be defined when the pitch angle is 90^o. To overcome this problem, another rotational sequence can be used in this instance instead of the Z→Y→X sequence.

3.1.3 Quaternions

Unlike the Euler angles, which stem from three rotations, quaternions are the parameters that stem from the axis and angle of single rotation. Quaternions' parameter begins from Eigen axis rotation theory. According to Euler, the attitude can be determined not only from three rotations of frame as in the Euler angles representation, but also with only one rotation. The axis that must only be rotated once is called the Eigen axis or the Euler axis. To describe an axis of rotation, three direction components and one variable are required for the angle. The quaternions are based on the Eigen axis and the angle of rotation about this axis. The quaternions parameter (q_1, q_2, q_3, and q_4) is as follows [30]:

$$\begin{aligned} q_1 &= e_1 \sin\frac{\theta}{2} \\ q_2 &= e_2 \sin\frac{\theta}{2} \\ q_3 &= e_3 \sin\frac{\theta}{2} \\ q_4 &= \cos\frac{\theta}{2} \end{aligned} \quad (3\text{-}10)$$

where θ denotes the rotation angle and e_1, e_2, and e_3 are the unit vector's components

along the Eigen axis, which satisfy $e_1^2 + e_2^2 + e_3^2 = 1$. The only one direction cosine matrix for quaternions is as follows:

$$C^{I/B} = \left(C^{B/I}(q_1, q_2, q_3, q_4)\right)^T = \begin{bmatrix} 1-2(q_2^2+q_3^2) & 2(q_1q_2 - q_3q_4) & 2(q_1q_3 + q_2q_4) \\ 2(q_1q_2 + q_3q_4) & 1-2(q_1^2+q_3^2) & 2(q_2q_3 - q_1q_4) \\ 2(q_1q_3 - q_2q_4) & 2(q_2q_3 + q_1q_4) & 1-2(q_1^2+q_2^2) \end{bmatrix} \quad (3\text{-}11)$$

The quaternions should always satisfy the following condition:

$$q_1^2 + q_2^2 + q_3^2 + q_4^2 = 1 \quad (3\text{-}12)$$

The advantage of quaternion representations over Euler angles is that quaternions can describe all possible attitudes and need not employ trigonometric functions.

The kinematic equation for the quaternions is arranged from Eq. (3-4) to solve for ω_x, ω_y, and ω_z. Substituting Eq. (3-11) in for every ω_x, ω_y, and ω_z results in the following equation:

$$\begin{bmatrix} \dot{q}_1 \\ \dot{q}_2 \\ \dot{q}_3 \\ \dot{q}_4 \end{bmatrix} = \frac{1}{2} \begin{bmatrix} q_4 & -q_3 & q_2 & q_1 \\ q_3 & q_4 & -q_1 & q_2 \\ -q_2 & q_1 & q_4 & q_3 \\ -q_1 & -q_2 & -q_3 & q_4 \end{bmatrix} \begin{bmatrix} \omega_x \\ \omega_y \\ \omega_z \\ 0 \end{bmatrix} \quad (3\text{-}13)$$

The kinematic equation above can also be rearranged to form the following:

$$\begin{bmatrix} \dot{q}_1 \\ \dot{q}_2 \\ \dot{q}_3 \\ \dot{q}_4 \end{bmatrix} = \frac{1}{2} \begin{bmatrix} 0 & \omega_z & -\omega_y & \omega_x \\ -\omega_z & 0 & \omega_x & \omega_y \\ \omega_y & -\omega_x & 0 & \omega_z \\ -\omega_x & -\omega_y & -\omega_z & 0 \end{bmatrix} \begin{bmatrix} q_1 \\ q_2 \\ q_3 \\ q_4 \end{bmatrix} \quad (3\text{-}14)$$

3.2 Attitude Determination

An accelerometer or a gyro is sometimes called an inertial navigation sensor because it measures some parameters with respect to the inertial frame. Inertial navigation measures the position and attitude with inertial sensors. The term attitude in this study corresponds to horizontal attitude, so the roll and pitch angles are here the consideration angles.

This subsection will discuss some methods for calculating horizontal attitude with a gyro or an accelerometer independently and by blending the two sensors. The gyro and accelerometer data comes from the IMU sensor designed by Logical Product, Japan. The ± 16 [G] of accelerometer and ± 1500 [deg/s] of the gyroscope is used in this

theoretical study. The sensor specification comes from the empirical study that will be discussed in the subsection 3.3.

The current study uses a servo motor as a test bed and places the IMU on the servo's arm. Some reflective markers welded together using an acrylic torch are then attached to the IMU to provide movement data to the motion capturing system as shown in Fig. 3.3. The servo was moved clockwise and counter-clockwise continuously.

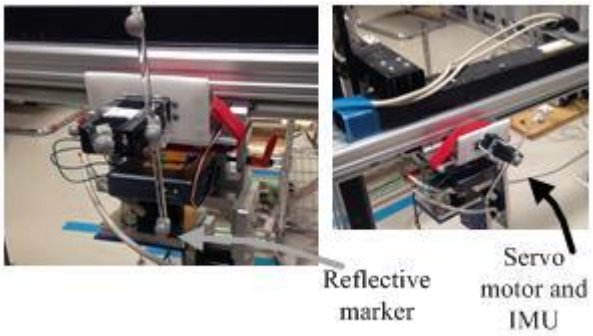

Figure 3.3 Test bed for attitude determination in theoretical study of attitude sensing

3.2.1 Attitude Determination using Gyro

Kinematic Eq. (3-9) represents a rate of change in the Euler angles and angular velocities. Attitude can be measured by integrating the results with respect to time. However, the numerical integration process leads to local and global truncation errors. Figure 3.4 shows that the attitude determination using only gyro led to some errors over time compares to the reference from a motion capturing system. A gyro is therefore accurate only for short period measurement and inaccurate for long period variation.

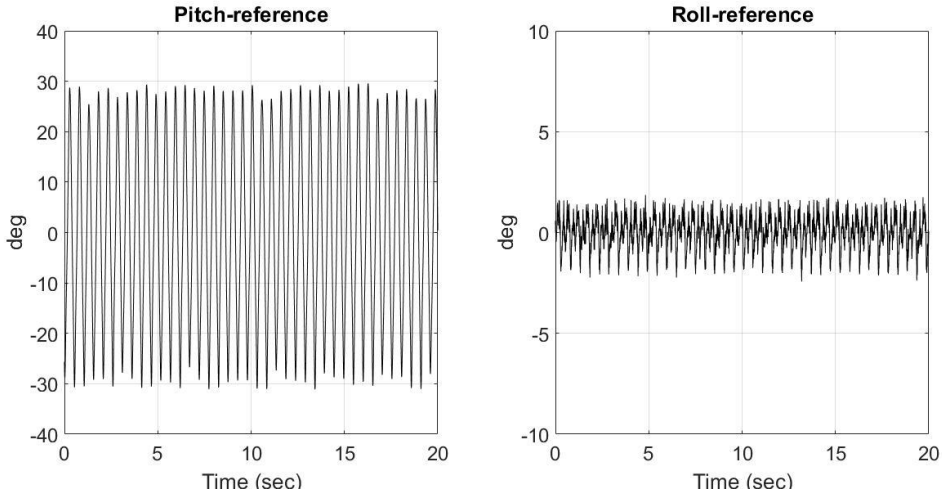

(a)

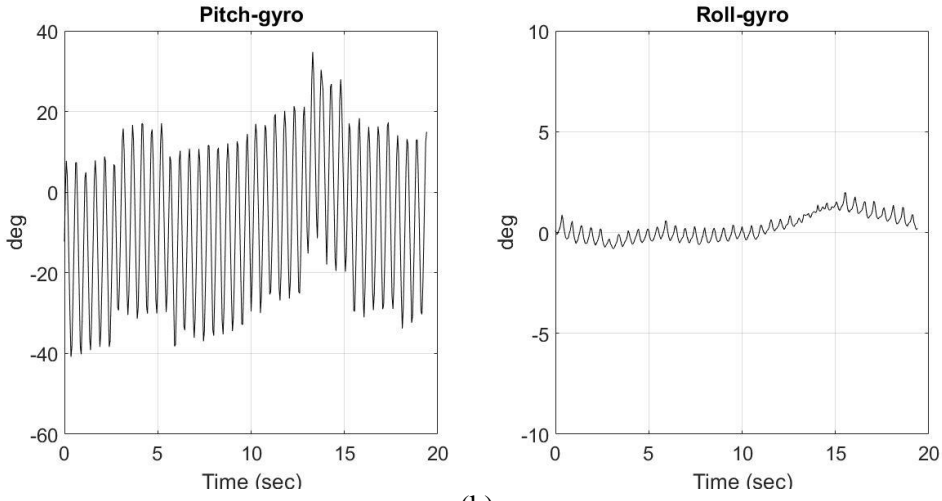

(b)

Figure 3.4 Attitude determination using gyro: (a) The reference angle; (b) the attitude determination from the gyro.

3.2.2 Attitude Determination using Three-Axis Accelerometer

An accelerometer can be used to measure a tilt angle, while a single axis accelerometer is limited in that it can only measure one axis tilt. Therefore, many applications use a three-axis accelerometer. An accelerometer measures specific forces (f_x, f_y, and f_z) that contain the gravitational acceleration, including the effect of velocity and the angular velocity in each axis [31]. The following equation is a model of accelerometer measurement:

$$\begin{bmatrix} f_x \\ f_y \\ f_z \end{bmatrix} = \begin{bmatrix} \dot{u} \\ \dot{v} \\ \dot{w} \end{bmatrix} + \begin{bmatrix} 0 & w & -v \\ -w & 0 & u \\ v & -u & 0 \end{bmatrix} \begin{bmatrix} p \\ q \\ r \end{bmatrix} + \begin{bmatrix} -r^2 - q^2 & pq - r^2 & pr + \dot{q} \\ pq + \dot{r} & -p^2 - r^2 & rq - \dot{p} \\ pr - \dot{q} & rq + \dot{p} & -q^2 - p^2 \end{bmatrix} \begin{bmatrix} l_x \\ l_y \\ l_z \end{bmatrix} + g \begin{bmatrix} \sin\theta \\ -\cos\theta \sin\phi \\ -\cos\theta \cos\phi \end{bmatrix} \tag{3-15}$$

where (u, v, and w) are the velocities along each axis in the body frame; (l_x, l_y, and l_z) are the accelerometer's coordinates along each axis in the body frame with its origin at the center of gravity; the (p, q, and r) are the angular velocities about each axis. The velocities and angular velocities along each axis in the body frame are difficult to obtain from a low-cost IMU. However, by assuming that the system is stationary or moving with a constant velocity, it is possible to find attitude (θ and ϕ). In the case of the stationary assumption, velocities and acceleration in each frame are zero, i.e., $u = v = w = 0$. In the case of constant velocity, the angular velocity and acceleration in each axis are also zero, i.e., $p = q = r = 0$ and $\dot{u} = \dot{v} = \dot{w} = 0$. With this simplification, Eq. (3-15) becomes as follows:

$$\begin{bmatrix} f_x \\ f_y \\ f_z \end{bmatrix} = g \begin{bmatrix} \sin\theta \\ -\cos\theta \sin\phi \\ -\cos\theta \cos\phi \end{bmatrix} \tag{3-16}$$

From Eq. (3-16), the roll and pitch, which are commonly called leveling, will be as follows:

$$\phi = \sin^{-1}\left(\frac{-f_y}{g\cos\theta}\right), \quad \theta = \sin^{-1}\left(\frac{f_x}{g}\right) \tag{3-17}$$

The leveling equation assumes that the accelerometer is stationary, so only the reaction of gravity is measured; thus, any external acceleration disrupts the leveling process. A 1 [m/s^2] forward acceleration will lead to a pitch determination error of about 100 [mrad] (5.7^o) [14].

Leveling Eq. (3-17) can be written using atan2, which allows for the calculation of the four-quadrant arctangent [14, 31]:

$$\phi = \text{atan2}\left(f_y, f_z\right), \quad \theta = \text{atan2}\left(-f_x, \sqrt{f_y^2 + f_z^2}\right) \tag{3-18}$$

Figure 3.5 shows the result of attitude determination via the three-axis accelerometer compared with the reference from the motion capturing system. The focus is on the pitch angle, as the movement of the axis is on the y-axis. The ideal value of the roll angle is zero, so the roll angle from reference and attitude determination also works as

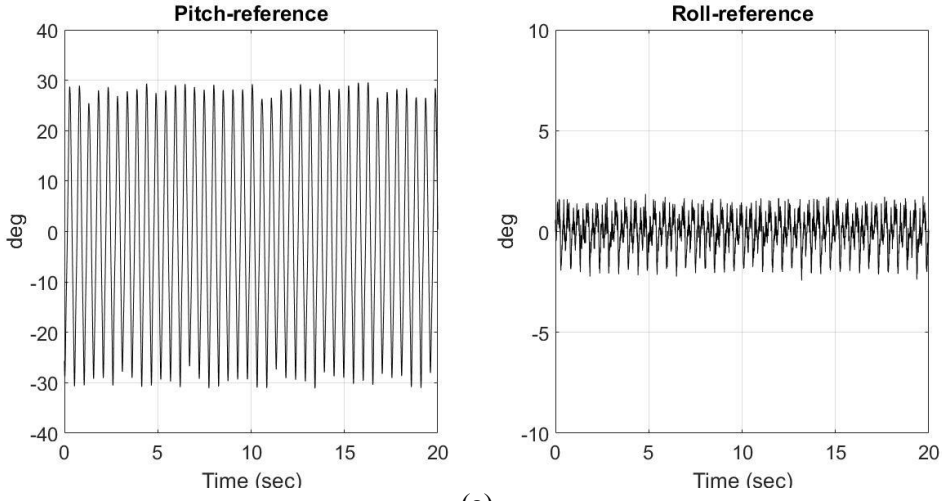

(a)

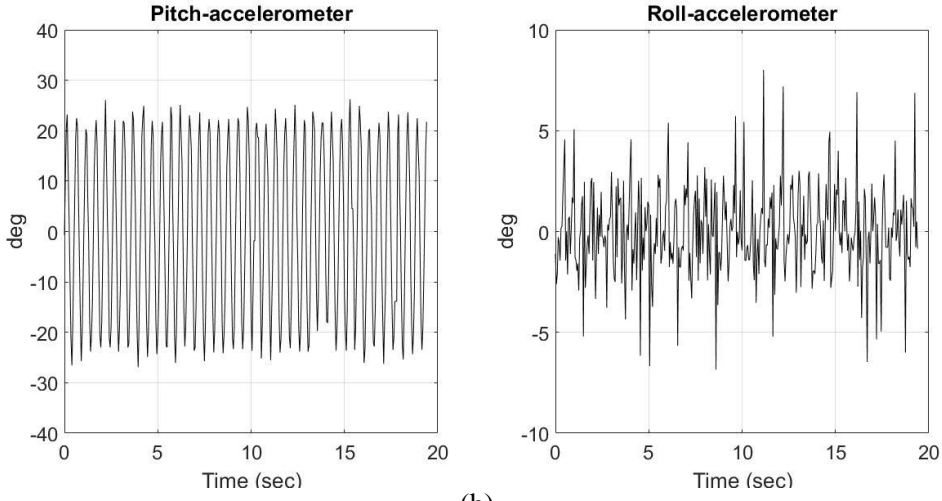

(b)

Figure 3.5 Attitude determination using accelerometer: (a) The reference angle; (b) the attitude determination from the accelerometer.

expected. However, for the pitch angle from the accelerometer using Eq. (3-17), the maximum value is $\pm 23^{o}$, which is below the reference value of $\pm 30^{o}$. The accuracy of the accelerometer in determining attitude is therefore not high, because either Eq. (3-17) or Eq. (3-18) is an approximation that is only valid under specific conditions.

3.2.3 Attitude Determination using Accelerometer and Gyro

The idea of combining accelerometer and gyro data comes from the results in the previous subsection. The attitude determined by the accelerometer is stable without growing along time; however, the attitude from the gyro is therefore prone to being

unbounded, bias, and random-walk errors [32]. On the other hand, acceleration data is unreliable in the presence of external acceleration or sometimes vibrations; however, gyro data can be trusted in the presence of external acceleration. Combining the sensors' data through sensor fusion yields a better performance that is impossible to achieve by an independent sensor. The estimator's algorithm evolved along two major paths: the Kalman filter and the complementary filter [19].

Figure 3.6 shows the attitude estimation using fusion data, which employs the Kalman filtering method, the discussion of which is in the next subsection. The pitch angle estimation is almost the same, with a value of reference that is $\pm 30^{o}$, while the roll angle estimation ranged around zero-degree. The advantages of each sensor have been blended to mitigate their disadvantages using the fusion technique.

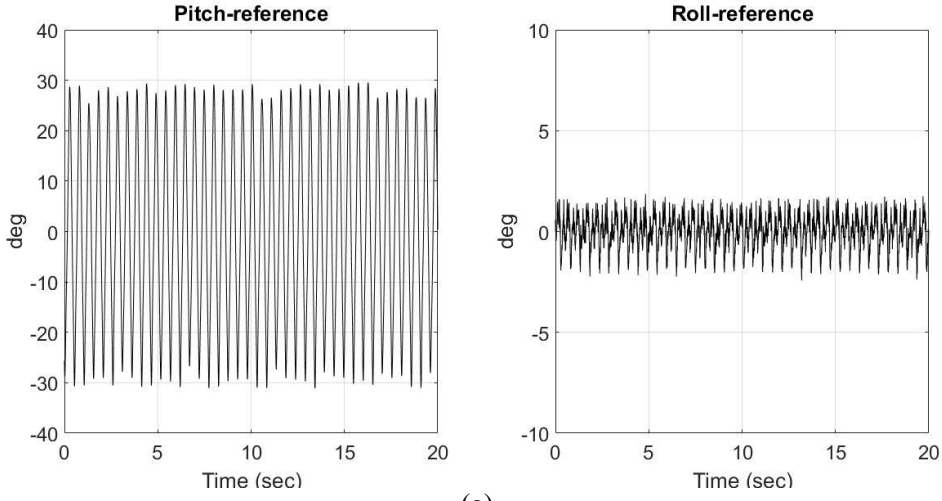

(a)

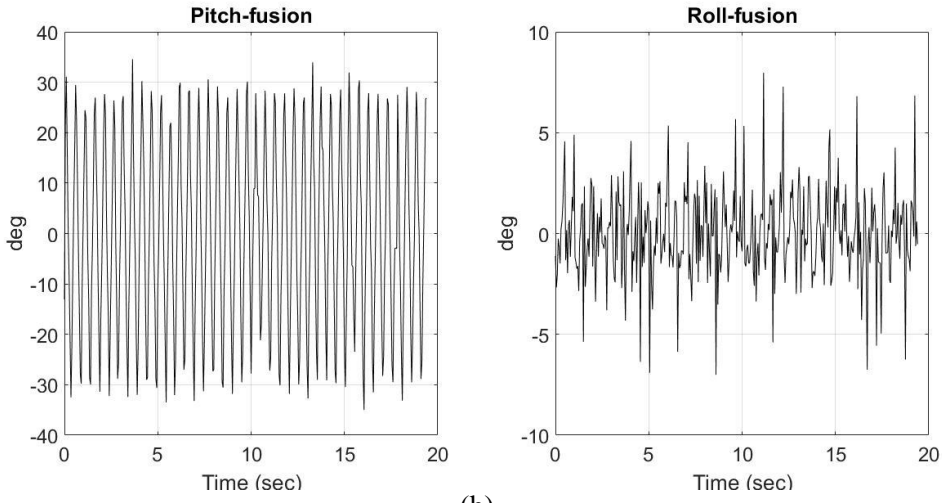

(b)

Figure 3.6 Attitude determination using sensor fusion: (a) The reference angle; (b) the attitude determination from sensor fusion.

3.3 Study of Inertial Sensor Placement and Specification

This subsection concerns the IMU (inertial measurement unit) sensor placement that will be used in the walking experiment in subsection 3.5.5. The purpose of the IMU placement on the shoe is categorized into the following two objectives regarding the ankle movement: 1) to assess the pitch angle of the foot when the ankle movements are dorsiflexion and plantar flexion, and 2) to assess the roll angle of the foot when the ankle movements are inversion and eversion, as shown in Fig. 3.7.

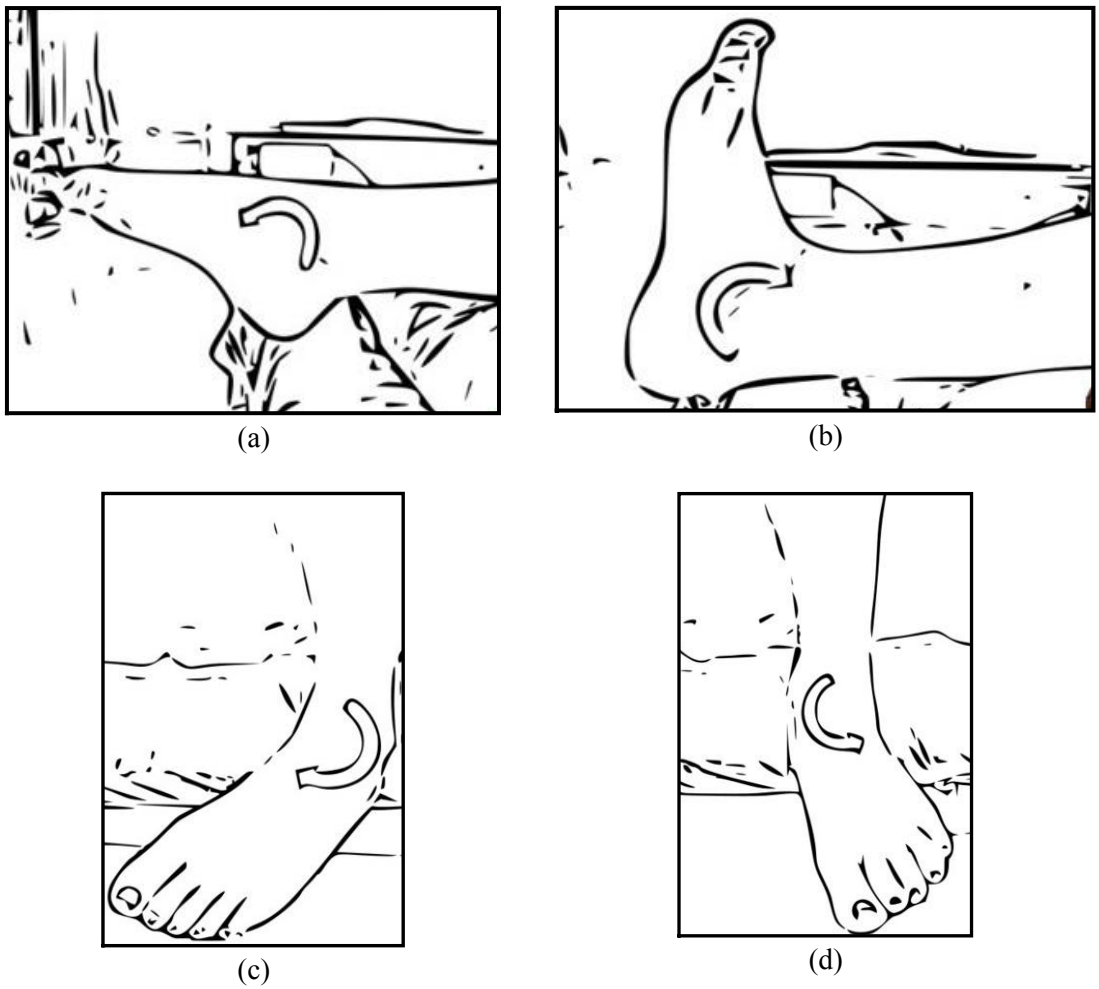

Figure 3.7 The four ankle movements that caused the pitch and roll angle: a) plantar flexion, b) dorsiflexion, c) inversion, and d) eversion.

The position of the IMU to assess the human gait can be categorized into the following five segments, as illustrated in Fig. 3.8:

a) the back of the shoe [2, 39]; in this study, the name of this position is "heel,"

b) two positions integrated in the heels [23]: the position on the medial side of shoe will be called "in-heel 1," and the position on the lateral side of shoe will be called "in-heel 2,"

c) upper part of the shoe [3, 4, 24-28]; this position will be called "mid,"

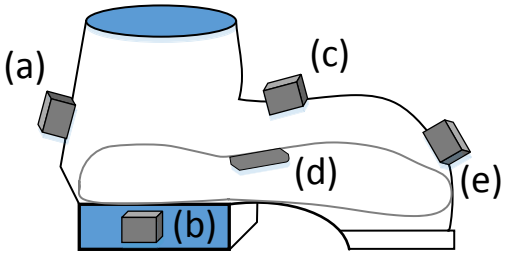

Figure 3.8 The possibility of the IMU sensor position: (a) at the back of the shoe (heel), (b) integrated in the heels (in-heel 1 and in-heel 2), (c) upper part of the shoe (mid), (d) integrated in the insole board (in-sole), and (e) on the toe position (toes).

d) the insole board (Veristride, Salt Lake City, UT, USA); this position will be named as "in-sole,"

e) toe position; the name of this position is "toes."

We will examine the position of each candidate, six in total.

3.3.1 Experimental Design for IMU Sensor Placement

The purposes of the experiment are: 1) to determine the IMU sensor position based on the acceleration data, and 2) to determine the IMU specification based on acceleration and angular velocity data. As all vibration acceleration also forms a part of

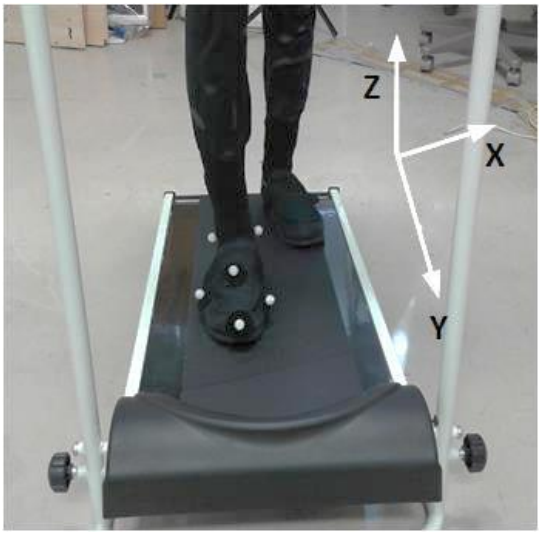

Figure 3.9 Experimental setup: walking trial on a treadmill while wearing an experimental shoe.

the external acceleration, as in Groves [14], that will reduce the attitude estimation in the method. In this study, we avoided the position that considered of higher measured acceleration. The effects of vibration were measured using the acceleration on the vertical axis (*z*-axis), coronal plane (*y*-axis), and sagittal plane (*x*-axis), as in Saade [68] and Abercromby [69]. We hypothesis that the position that the IMU was far away from the ground will be reduced the effect of vibration acceleration on the *z*-axis. The z-axis is the main direction of human walking especially on the heel-strike time.

To select the IMU position among the positions of the candidate in Fig. 3.8: (a) heel, (b) in-heel 1 and in-heel 2, (c) mid, (d) in-sole, and (e) toes, we conducted a walking trial on a treadmill while wearing a shoe equipped with reflective markers, as shown in Fig. 3.9. The position of markers represents the candidate position of the IMU sensor, due to the purpose of counting the rotation matrix of the foot segment coordinate system. Table 3.2 represents the markers name and the function of each marker.

Table 3.2 Abbreviations for Calibration Markers

Marker	Description	Function
$\mathbf{P}_{RMA}$	Right medial malleolus	Coordinate system transformation
$\mathbf{P}_{RLA}$	Right lateral malleolus	Coordinate system transformation
$\mathbf{P}_{RMH5}$	Right fifth metatarsal head	Coordinate system transformation
$\mathbf{P}_{RMH1}$	Right first metatarsal head	Coordinate system transformation
$\mathbf{P}_{RToe}$	Right toe	Candidate position of IMU
$\mathbf{P}_{RHeel}$	Right heel	Candidate position of IMU
$\mathbf{P}_{RMid}$	Right tarso metatarsal joint	Candidate position of IMU
$\mathbf{P}_{R\text{in-heel1}}$	Right medial integrated heel position	Candidate position of IMU
$\mathbf{P}_{R\text{in-heel2}}$	Right lateral integrated heel position	Candidate position of IMU
$\mathbf{P}_{R\text{in-sole}}$	Right integrated in-sole position	Candidate position of IMU

The acceleration and angular velocity were calculated in the foot segment local coordinate system (LCS) by first calculating the rotation matrix. The method to define the foot segment LCS used three non-collinear points, as suggested in [61]. Refer to the marker positions and names in Fig. 3.10 and Table 3.2. The origin of the LCS is as follows [61]:

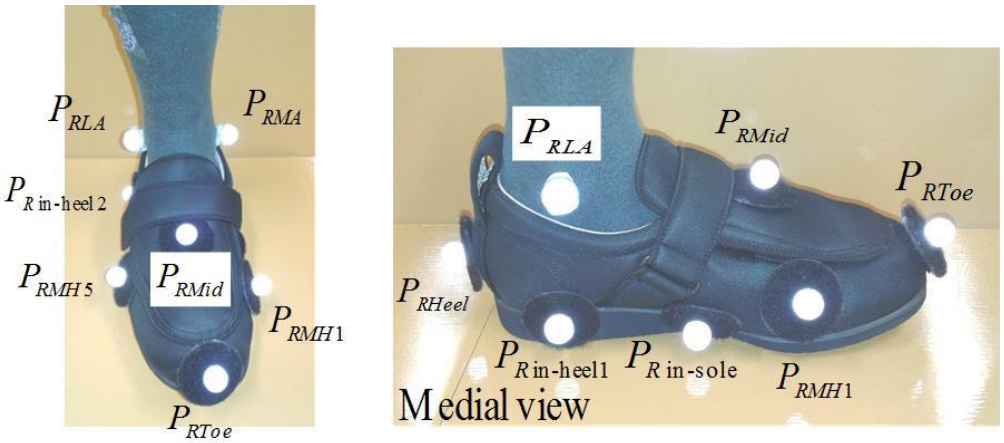

Figure 3.10 Calibration markers position on the frontal and sagittal plane.

$$\mathbf{O}_{RFoot} = 0.5(\mathbf{P}_{RLA} + \mathbf{P}_{RMA}) \tag{3-19}$$

The axially-directed unit vector:

$$\hat{\mathbf{k}}' = \frac{\mathbf{O}_{RFoot} - 0.5(\mathbf{P}_{RMH5} + \mathbf{P}_{RMH1})}{\left|\mathbf{O}_{RFoot} - 0.5(\mathbf{P}_{RMH5} + \mathbf{P}_{RMH1})\right|} \tag{3-20}$$

A unit vector passing from medial malleolus to the lateral malleolus:

$$\hat{\mathbf{v}} = \frac{(\mathbf{P}_{RLA} - \mathbf{P}_{RMA})}{\left|\mathbf{P}_{RLA} - \mathbf{P}_{RMA}\right|} \tag{3-21}$$

An anterior unit vector created from the cross product of the $\hat{\mathbf{k}}'$ and $\hat{\mathbf{v}}$ unit vectors:

$$\hat{\mathbf{j}}' = \hat{\mathbf{k}}' \times \hat{\mathbf{v}} \tag{3-22}$$

The third unit vector, derived from the cross product:

$$\hat{\mathbf{i}}' = \hat{\mathbf{j}}' \times \hat{\mathbf{k}}' \tag{3-23}$$

The rotation matrix converting the coordinates of a point ***P*** in the GCS (global coordinate system) to ***P'*** in the LCS can be expressed as:

$$\mathbf{R}_{\mathbf{Foot}} = \begin{bmatrix} \hat{\mathbf{i}}'_{\mathbf{x}} & \hat{\mathbf{i}}'_{\mathbf{y}} & \hat{\mathbf{i}}'_{\mathbf{z}} \\ \hat{\mathbf{j}}'_{\mathbf{x}} & \hat{\mathbf{j}}'_{\mathbf{y}} & \hat{\mathbf{j}}'_{\mathbf{z}} \\ \hat{\mathbf{k}}'_{\mathbf{x}} & \hat{\mathbf{k}}'_{\mathbf{y}} & \hat{\mathbf{k}}'_{\mathbf{z}} \end{bmatrix} \tag{3-24}$$

Using Eq. (3-24), the acceleration measured from the motion capturing system will be transformed to the LCS as follows:

$$\mathbf{a}' = \mathbf{R}_{\mathbf{Foot}}\,\mathbf{a} \tag{3-25}$$

The angular velocity (in degree/second) that was experienced by the foot will be used to determine the specification of the IMU sensor. The angular velocity of the shoe movement relative to the laboratory GCS is derived from differentiating the rotation matrix using finite differences [61]. The angular velocity $\boldsymbol{\omega}_i$ at time t_i is computed as follows:

$$\mathbf{R}_{\Delta} = \mathbf{R}_{\mathbf{t+1}}\,\mathbf{R}_{\mathbf{t-1}} \tag{3-26}$$

$$\left|\boldsymbol{\omega}_{\mathbf{i}}\right| = \frac{\delta}{t_{i+1} - t_{i-1}} \tag{3-27}$$

where $\delta = \cos^{-1}\left(\dfrac{\mathbf{R}_{\Delta 11} + \mathbf{R}_{\Delta 22} + \mathbf{R}_{\Delta 33} - 1}{2}\right)$

The unit vector is computed as:

$$\hat{\mathbf{v}} = \frac{\begin{bmatrix} \mathbf{R}_{\Delta 23} - \mathbf{R}_{\Delta 32} \\ \mathbf{R}_{\Delta 31} - \mathbf{R}_{\Delta 13} \\ \mathbf{R}_{\Delta 12} - \mathbf{R}_{\Delta 21} \end{bmatrix}}{2\sin\delta} \tag{3-28}$$

The angular velocity in the LCS is as follows:

$$\boldsymbol{\omega}_{\mathbf{i}}' = \left|\boldsymbol{\omega}_{\mathbf{i}}\right| \hat{\mathbf{v}} \tag{3-29}$$

3.3.2 Data Collection and Statistical Analyses

The experimental design is as follows: The walking trials consisted of ten tasks, and each trial was executed in approximately 20 to 50 seconds by one subject. Therefore each candidate position has ten samples. The average walking speed was 1.2 to 1.8 [m/s] or 4.5 to 6.7 [km/h].

Based on the markers testing position, as shown in Fig. 3.10, we selected six markers data as representative of the IMU position in the heel, in the mid of the shoe, in the toe position, in the in-sole, in the in-heel 1, and in the in-heel 2; those markers are $\mathbf{P}_{RHeel}$, $\mathbf{P}_{RMid}$, $\mathbf{P}_{RToe}$, $\mathbf{P}_{R\text{in-sole}}$, $\mathbf{P}_{R\text{in-heel1}}$, and $\mathbf{P}_{R\text{in-heel2}}$. The markers data were analyzed using Venus3D software (Nobby Tech. Ltd. Japan) to provide the position, acceleration, and velocity data in the global coordinate system following the Eqs. (3.19) to (3.29). For further statistical processing IBM SPSS Statistics ver. 21 and JMP® ver. 13.0.0 for nonparametric analysis were used.

The total groups are three: 1) X-axis, 2) Y-axis, and 3) Z-axis; each group contains six categorical positions. Basic descriptive statistics were conducted: deviation from the normal distribution or tests of normality was conducted using Kolmogorov-Smirnov test, the null hypothesis is the data from a normally-distributed population.

The group that the assumption of normality has been rejected will be analyzed using non-parametric test, in this case the independent-samples Kruskal-Wallis test with Steel-Dwass method for multiple comparisons. On the other hand, the group that has the normal distribution will be analyzed using one-way ANOVA with Tukey post-hoc tests.

3.3.3 Statistical Results

First of all, the descriptive statistic using a boxplot is presented in the Fig. 3.11. Test of normality using Kolmogorov-Smirnov test was summarized in the Table 3.3.

Table 3.3 Kolmogorov-Smirnov Test of Normality

Position (X-axis)	Kolmogorov-Smirnov	Position (Y-axis)	Kolmogorov-Smirnov	Position (Z-axis)	Kolmogorov-Smirnov
	Sig.		Sig.		Sig.
Xheel	.200	Yheel	.200	Zheel	.200
Xmid	.200	Ymid	.200	Zmid	.145
Xtoes	.200	Ytoes	.156	Ztoes	.024
Xin-sole	.200	Yin-sole	.200	Zin-sole	.200
Xin-heel1	.001	Yin-heel1	.200	Zin-heel1	.200
Xin-heel2	.200	Yin-heel2	.200	Zin-heel2	.200

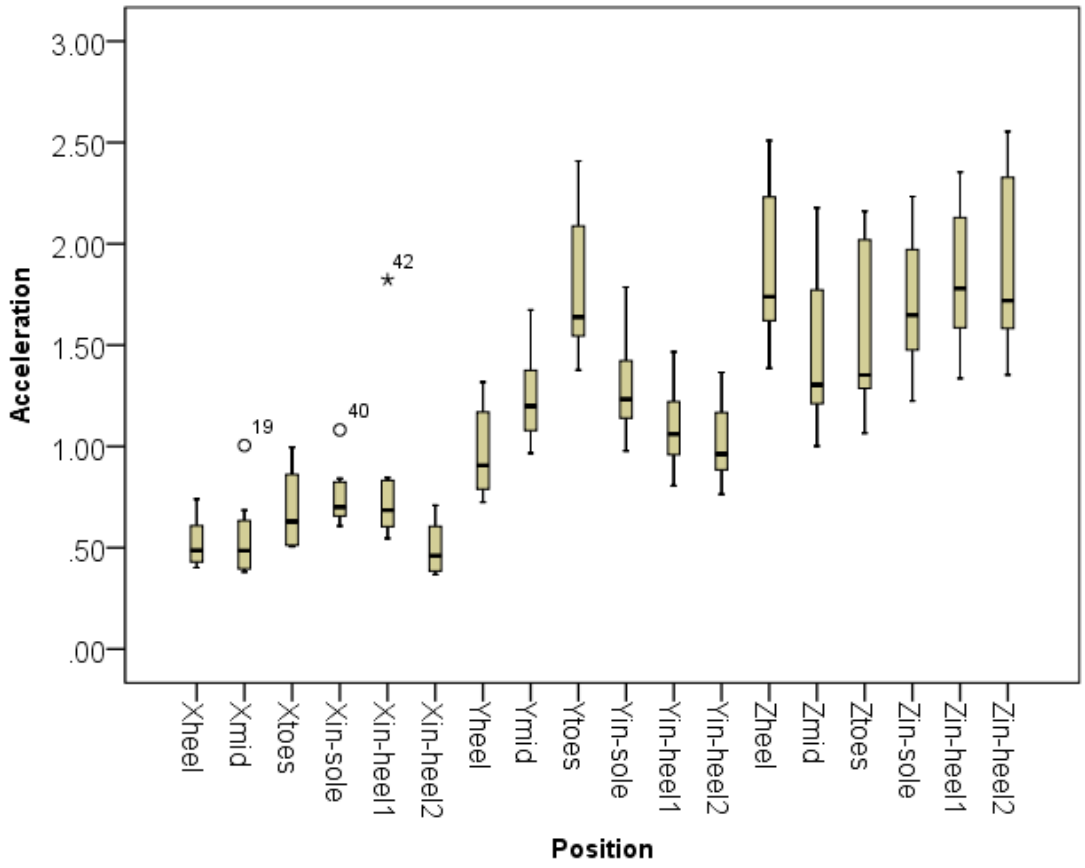

Figure 3.11 The boxplot of all data distribution

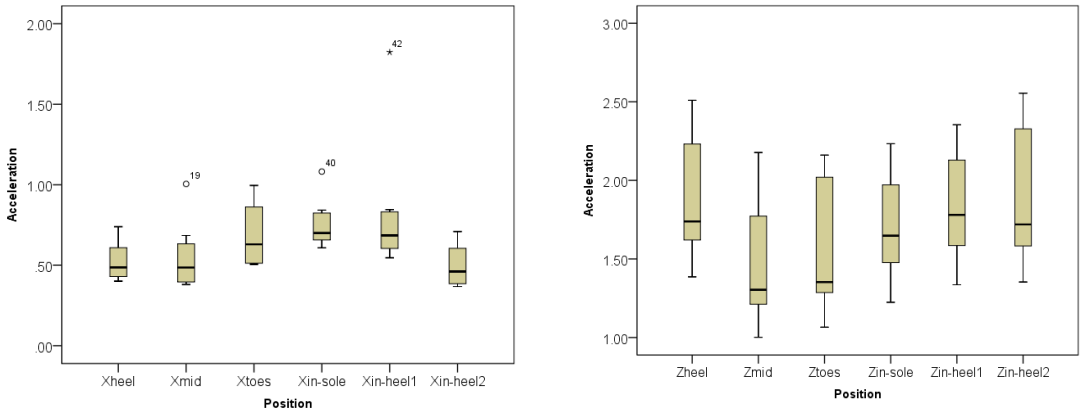

(a) (b)

Figure 3.12 The boxplot of a) X-axis and b) Z-axis data distribution; for the purpose of similarity test.

3.3.3.1 X-Axis and Z-Axis Statistical Results

From Table 3.3, the "Xin-heel1" and "Ztoes" position indicated that the data is not in normal distribution ($p < .05$); therefore, the independent-samples Kruskal-Wallis test will be executed for X-axis and Z-axis position.

Kruskal-Wallis test null hypothesis: "The distribution of Acceleration is the same across categories of Position." The result of test including the mean rank and median was summarized in Table 3.4. The detailed boxplot of X-axis and Z-axis position is presented again in Fig 3.12 to test the similarity shaped. From Fig. 3.12, it shown that the distributions of Acceleration scores were not similar for all categories in the X-axis, as assessed by visual inspection of this boxplot. The skewness is not the same among the categories and also the whiskers length indicated non uniformity among categories. Therefore, the inferences will be based on mean ranks rather than based on the differences in medians. However in the Z-axis, the distributions of Acceleration scores were similar for all categories. Therefore, the inferences will be based on differences in medians.

Table 3.4 Report of Kruskal-Wallis Test Results

	Position	N	Mean Rank	Test Statistics	
Acceleration	Xheel	10	21.10	Chi-Square	21.073
	Xmid	10	22.10		
	Xtoes	10	36.30	df	5
	Xin-sole	10	44.00		
	Xin-heel1	10	41.30	Asymp. Sig.	.001
	Xin-heel2	10	18.20		
	Position	N	Median	Test Statistics	
Acceleration	Zheel	10	1.73	Chi-Square	11.250
	Zmid	10	1.30		
	Ztoes	10	1.36	df	5
	Zin-sole	10	1.65		
	Zin-heel1	10	1.78	Asymp. Sig.	.047
	Zin-heel2	10	1.72		

Our report for the results in Table 3.4 (X-axis and Z-axis):

The mean ranks of Acceleration values were statistically significantly different between categories, ($\chi^2(5) = 21.073$, $p = .001$) and ($\chi^2(5) = 11.25$, $p = .047$) for X-axis and Z-axis, respectively. The post-hoc test using Steel-Dwass method multiple comparisons will be conducted to interpret all pairwise comparisons.

The final report of the X-axis difference test is as follows:

A Kruskal-Wallis H test was conducted to determine if there were differences in Acceleration value between categories that differed in their position. Values are mean ranks unless otherwise stated. Distributions of Acceleration values were not similar for all categories, as assessed by visual inspection of a boxplot in Fig. 3.12(a). Acceleration value increased from Xin-heel2 (18.2), to Xheel (21.1), to Xmid (22.1), to Xtoes (36.3), to Xin-heel1 (41.3), to Xin-sole (44.0) position categories. Acceleration values were statistically significantly different between the different position categories, $\chi^2(5) = 21.073$, $p = .001$. Subsequently, multiple comparisons results are as follows:

1) Engagement scores for *Xin-sole* (mean rank = 44.00) were statistically significantly higher than for *Xheel* (mean rank = 21.10), $z = 3.062$, $p = .0268$.

2) Engagement scores for *Xin-sole* (mean rank = 44.00) were statistically significantly higher than for *Xin-heel2* (mean rank = 18.20), $z = 2.986$, $p = .0337$.

The final report of the Z-axis difference test is as follows:

A Kruskal-Wallis H test was conducted to determine if there were differences in Acceleration value between categories that differed in their position. Distributions of Acceleration values were similar for all categories, as assessed by visual inspection of a boxplot in Fig. 3.12(b). Median score of Acceleration values were statistically significantly different between the different position categories, $\chi^2(5) = 11.250$, $p = .047$. The multiple comparisons results were performed using Steel-Dwass method indicates that there is no significant difference among categories. However, the tendency of p-value indicates that the pair of ***Zmid*** **and** ***Zheel*** and the pair of ***Zmid*** **and** ***Zin-heel2*** are the lowest among another pairs, i.e.: $p = .1916$.

3.3.3.2 Y-Axis Statistical Results

The one-way ANOVA will be used to understand whether there is a difference in mean of acceleration value in the candidate position. The null hypothesis is H_0: all sensor position category acceleration means are equal (i.e., $\mu_{Yheel} = \mu_{Ymid} = \mu_{Ytoes} = \mu_{Yin\text{-}sole} = \mu_{Yin\text{-}heel1} = \mu_{Yin\text{-}heel2}$). The alternative hypothesis is H_A: at least one category mean is different (i.e., they are not all equal).

The boxplot visual inspection in Fig. 3.11 confirmed that there were no outliers in the Y-axis. Either the Kolmogorov-Smirnov's test as shown in the Table 3.3, confirmed that the Y-axis data is normally distributed.

Test of homogeneity of variances was concluded in the Table 3.5. As shown in Table 3.5, the Levene's test is not statistically significant (i.e., $p > .05$); the variances of categories in Y-axis are equal. Therefore, the assumption of homogeneity of variances is met.

Table 3.5 Test of Homogeneity of Variances

Acceleration Y-axis

Levene Statistic	df1	df2	Sig.
1.963	5	54	.099

The one-way ANOVA result was shown in Table 3.6.

Table 3.6 The one-way ANOVA results

Acceleration Y-axis

	Sum of Squares	df	Mean Square	F	Sig.
Between Groups	4.552	5	.910	14.975	.000
Within Groups	3.283	54	.061		
Total	7.835	59			

The result in Table 3.6 has shown that the acceleration was statistically significantly different for different sensor position category, $F(5,54) = 14.975$, $p < .0005$, for Y-axis. The Tukey post hoc test to determine where exactly the differences lie was conducted in all categories of Y-axis.

The multiple comparisons table in Tukey post hoc test revealed that there are statistically significant result between "Ytoes position" and another position, as well between "Yin-sole" and "Yheel" position.

The final report of the Y-axis difference test is as follows:

The category means were statistically significantly different ($p < .0005$) and, therefore, we can reject the null hypothesis and accept the alternative hypothesis.

A one-way ANOVA was conducted to determine if the acceleration value on Y-axis was different for category with different position of IMU sensor on the shoe. Positions were classified into six categories: Yheel, Ymid, Ytoes, Yin-sole, Yin-heel1, and Yin-heel2. There were no outliers, as assessed by boxplot; data was normally distributed for each group, as assessed by Kolmogorov-Smirnov test ($p > .05$); and there was homogeneity of variances, as assessed by Levene's test of homogeneity of variances ($p = .099$). Data is presented as mean ± standard deviation. Acceleration was statistically significantly different between different position of sensor categories, $F(5, 54) = 14.975$, $p < .0005$. Tukey post hoc analysis revealed that the mean difference among these pairs was statistically significant: **Ytoes and Yheel** ($p < .0005$), **Ytoes and Ymid** ($p < .0005$), **Ytoes and Yin-sole** ($p < .0005$), **Ytoes and Yin-heel1** ($p < .0005$), **Ytoes and Yin-heel2** ($p < .0005$), and **Yin-sole and Yheel** ($p = .048$), but no other position category differences were statistically significant.

The RMS value of acceleration in the entire walking task is presented in the local coordinate system, as shown in Fig. 3.13.

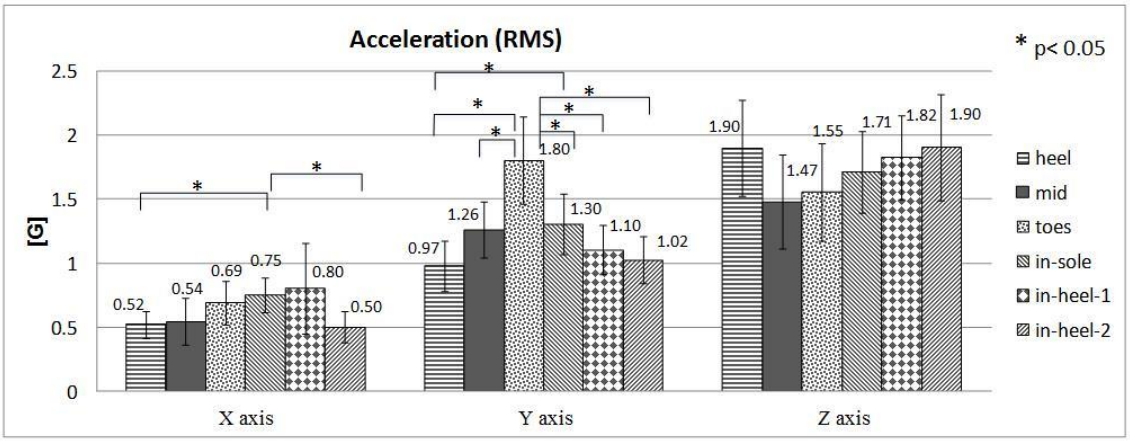

Figure 3.13 The root mean square of the walking task acceleration.

In order to determine the maximum value of acceleration experienced by the foot during walking, the maximum acceleration in each axis is presented in Fig. 3.14.

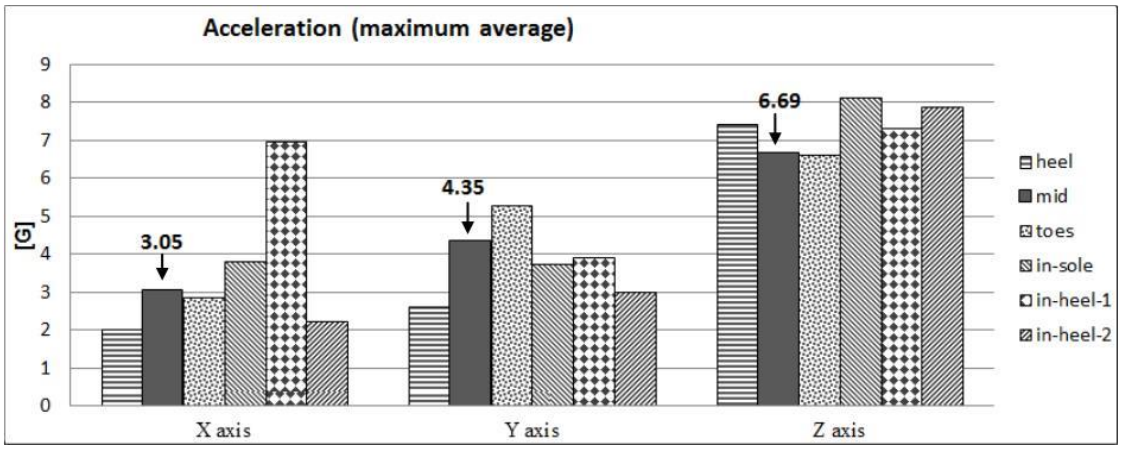

Figure 3.14 The maximum acceleration of the walking task on each candidate positions.

3.3.3.3 Angular Velocity Statistical Results

The other result concerning the angular velocity of foot segment during walking task will be analyzed as follows. The statistical analysis would be used to understand whether there is a difference in angular velocity in three categories (i.e., *X*-axis, *Y*-axis, and *Z*-axis). The null hypothesis is H_0: angular velocity in all axes categories means are equal (i.e., $\mu_{X\text{-axis}} = \mu_{Y\text{-axis}} = \mu_{Z\text{-axis}}$). The alternative hypothesis is H_A: at least one category mean is different (i.e., they are not all equal). The normality test was conducted using Shapiro-Wilk test and the statistical analysis was conducted using one-way ANOVA with Tukey post-hoc tests. The visual boxplot concerning angular velocity data is shown in Fig. 3.15.

The final report of the angular velocity difference test is as follows:

The category means were statistically significantly different ($p < .0005$) and, therefore, we can reject the null hypothesis and accept the alternative hypothesis.

A one-way ANOVA was conducted to determine if the angular velocity value was different for category with different axis. Axes were classified into three categories: X-axis, Y-axis, and Z-axis. There were no outliers, as assessed by boxplot; data was normally distributed for each group, as assessed by Shapiro-Wilk test ($p > .05$); and there was homogeneity of variances, as assessed by Levene's test of homogeneity of variances ($p = .07$). Data is presented as mean ± standard deviation. Angular velocity was statistically significantly different between different axis categories, $F(2, 27) = 395.53$, $p < .0005$. Tukey post hoc analysis revealed that the mean difference among these pairs was statistically significant: **X-axis and Y-axis** ($p < .0005$), **X-axis and Z-axis** ($p < .0005$), and **Y-axis and Z-axis** ($p < .0005$). Figure 3.16 shows the conclusion remarks of statistical test.

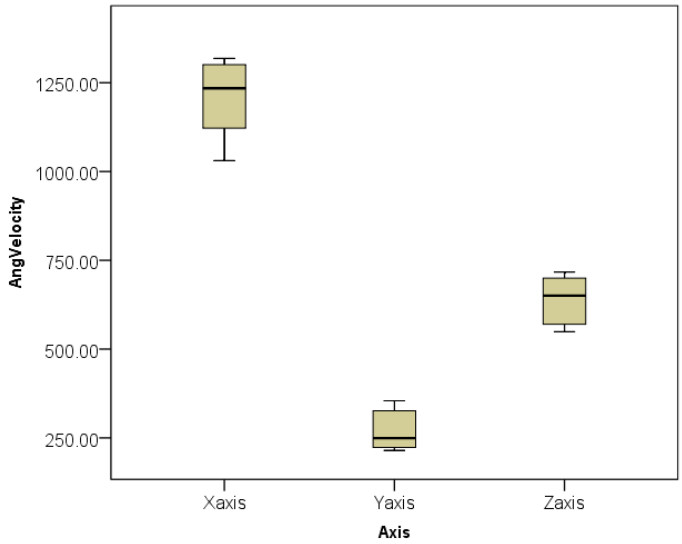

Figure 3.15 The boxplot of angular velocity data distribution.

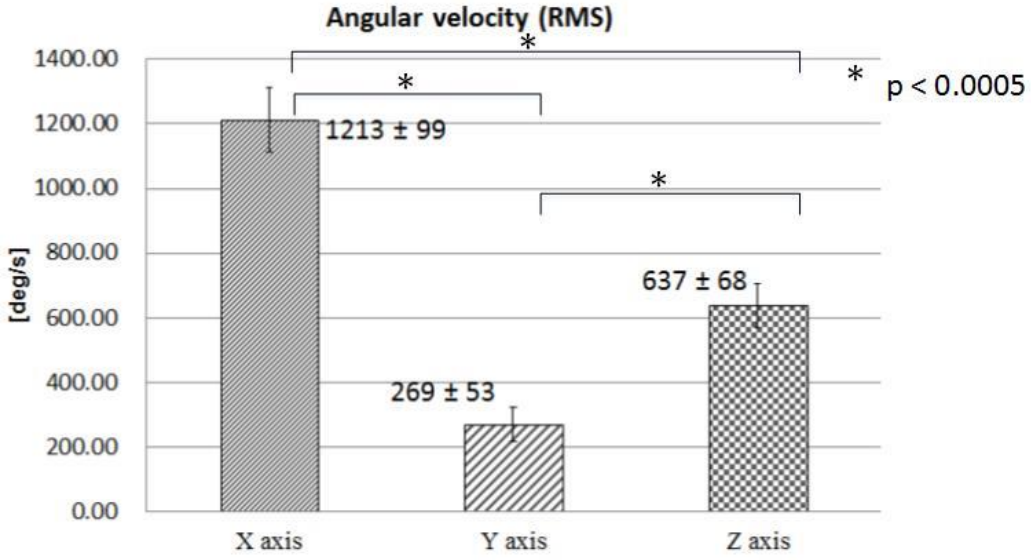

Figure 3.16 The root mean square value of foot angular velocity during the walking task on each axis of movement.

3.3.4 The Decision of IMU Sensor Placement and IMU Specification

Based on the experimental results in the previous subsection, we have two discussions: 1) the determination of IMU sensor placement based on acceleration data, and 2) the determination of IMU sensor specification based on angular velocity analyses.

The first discussion is the acceleration of the six markers in the six candidate

positions. As shown in Fig. 3.13, the acceleration on the *z*-axis is always the highest among other axes. When the subject walks, the impact between the shoes and treadmill mat will cause the vibration acceleration on the *z*-axis. The acceleration on the *z*-axis is the combination between true acceleration of movement and vibration acceleration. From Fig. 3.13, the lowest acceleration in the *z*-axis is "mid" position, although not statistically significantly different from another position but there is a tendency that the *p*-value between "mid" position and "heel" and also "mid" position and "in-heel2" ($p = .192$) is the lowest among another pairs.

The tendency of the acceleration on the *y*-axis is greater than the acceleration on the *x*-axis; this is in line, as the *y*-axis is a forward direction of movement, and the foot movement when walking is dominated by pitch angle. As shown on the *y*-axis, the "heel" position is the lowest followed by the "in-heel 2," "in-heel 1," and "mid" positions. However, on the *x*-axis, "in-heel 2" is shown to be the lowest, followed by the "heel" and "mid" positions, respectively. The content of acceleration on the *x*-axis and *y*-axis will be influenced by the movement itself and the vibration in its related direction; therefore, the position with the lowest value is the good candidate to be chosen.

The decision of the IMU position will consider the following matters:

1) On the *z*-axis, the vibration acceleration in the "mid" position showed the lowest tendency followed by the "toes" position. These positions are strong candidates to be selected for the place of the sensor.

2) The shoe-type gait measurement device consists of a rehabilitation shoes and an off-the-shelf IMU sensor. The placement of the IMU sensor in the "mid" position is considered to be stable, as the installation of the IMU used an elastic strap, as shown in Fig. 3.23.

3) Considering the tendency of the lowest vibration acceleration on the *z*-axis is "mid" position, the moderate level on the *x*-axis and *y*-axis is also "mid" position, and the stable mounting of the sensor in the "mid" position; this position is considered to be acceptable compared to other positions in our application.

The second discussion is the specification of the IMU sensor. Based on the empirical evidence in Fig. 3.14, it was found that the maximum acceleration is 6.69 [G] on the selected position. Concerning angular velocity, as shown in Fig. 3.16, 68% of angular velocity in the dataset lies between (1,213 – 99 = 1,114 [deg/s]) and (1,213 + 99 = 1,312 [deg/s]), for normal distribution dataset. Based on the empirical results, we ultimately chose an inertial sensor within the specification, as shown in Table 3.7, the sensors produced by Logical Product., Inc, Japan. The specification of the sensors is sufficient for this study.

Table 3.7 Inertial sensors specification

No	**Sensors**	**Range**	**Condition**
1	Acceleration	±16 [G]	9-axis wireless
2	Gyroscope	±1,500 [deg/s]	9-axis wireless
	Sampling frequency	100 [Hz]	Adjustable 1-1,000 [Hz]
	Power	1 x AAA battery	1.2 [V]

3.4 The Estimator and the Proposed External Acceleration Model

The results of determining attitude through an accelerometer and a leveling equation have been discussed in the subsection 3.2. The leveling equation makes the assumption that the accelerometer is stationary, so only the reaction of gravity is measured. One study reported that a 1 [m/s^2] forward acceleration would lead to a pitch determination error of about 100 [mrad] (5.7^o) [14]. Also, the error in the roll and pitch axis was too large because those two axes are mutually affected. When movement occurs in the roll axis, the pitch axis also moves up and down with respect to the horizontal plane, and vice versa. On the other hand, attitude determination from the gyro accumulated errors along the process of numerical integration, but the gyro was sensitive to the change of rotation while the attitude determination by the accelerometer did not show the accumulation errors or divergence.

The need for sensor fusion between the gyro and accelerometer is a major requirement for obtaining the performance that is impossible to achieve with an independent sensor. In this study, the extended Kalman filter (EKF) will be used due to the nonlinearity of the system [33, 34]. The algorithm will be divided into three categories: 1) *Initial values* of states $(\hat{\mathbf{x}}_0)$ and error covariance (P_0) ; 2) *Time update*, which consists of the prediction of states and of the error covariance; and 3) *Measurement update*, which consists of the Kalman gain calculation, the estimation of state, and the error covariance estimation. Figure 3.17 shows the structure of the proposed algorithm combined with the extended Kalman filter algorithm. The notations $\hat{\mathbf{x}}_k^-, P_k^-, K_k, \hat{\mathbf{x}}_k$, and P_k refer to prediction of state, prediction of the error covariance, Kalman gain, estimation of states, and the estimate of the error covariance, respectively. In Figure 3.17, the measurement comes from the accelerometer, and some modification to filter's parameter comes from the external acceleration model ($\mathbf{a}_k$). Based on the Table 2.2, the discussion below will explain the attitude estimation consisting of a standard EKF (*Mode 1*) and the EKF using the proposed external acceleration compensation model (*Mode 2*). As comparisons, another three methods other researchers have used to compensate for the external acceleration will be discussed (*Mode 3, 4, 5*).

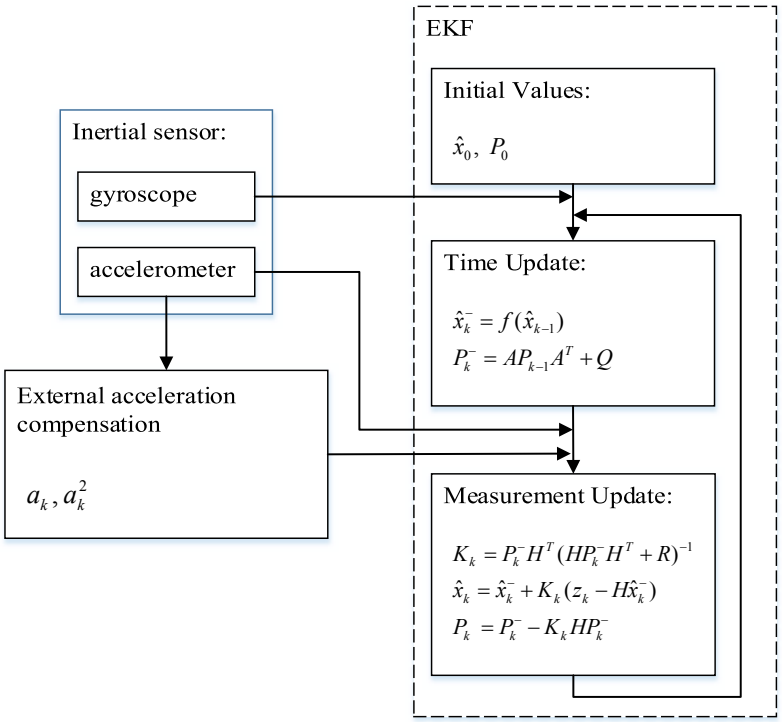

Figure 3.17 Structure of the proposed algorithm and EKF [20].

3.4.1 Standard EKF Model (*Mode 1*)

In this section, the standard EKF using the proposed system model without compensating for the external acceleration will be discussed; the term *Mode 1* is sometimes used for simplicity.

3.4.1.1 Process and Measurement Models

The first step is defining states and observation variables for the system model. The attitude and gyro bias is set as state variables, since the bias errors are a highly complex function to the ambient temperature. The Euler angle was the angle representation. The state variable ***x(t)*** and the measurement variable ***z(t)*** are defined as follows:

$$\mathbf{x} = [\phi \quad \theta \quad \psi \quad b_x \quad b_y \quad b_z]^T, \quad \mathbf{z} = [\phi_a \quad \theta_a \quad \psi_a]^T \tag{3-30}$$

Where ϕ (roll) and θ (pitch) are the rotation angles about the x and y axes, and ψ is yaw angle, but is not of concern in this study. These come from the integration of the rate of change from gyros, while b_x, b_y, b_z are biases from gyro in x, y, and z axis, respectively. The measurement variables are obtained from the accelerometer in order to calculate ϕ_a, θ_a, and ψ_a. The system equation is given by

$$\dot{\mathbf{x}}(t) = f(x(t)) + \mathbf{w}(t) \tag{3-31}$$

$$\mathbf{z}(t) = H\mathbf{x}(t) + \mathbf{v}(t) \tag{3-32}$$

Where *f(x(t))* is a nonlinear function representing the relation between gyros data and kinematic equation for the Euler angles (Z→Y→X); H is state to measurement matrix as shown in Eq. (3-33); and **w***(t)* and **v***(t)* are process noise and measurement noise, respectively, which are assumed to be uncorrelated Gaussian distributed white noise.

$$f(x) = \begin{bmatrix} 1 & s\phi\, t\theta & c\phi\, t\theta & 0 & 0 & 0 \\ 0 & c\phi & -s\phi & 0 & 0 & 0 \\ 0 & s\phi\, sc\theta & c\phi\, sc\theta & 0 & 0 & 0 \\ 0 & 0 & 0 & 1 & 0 & 0 \\ 0 & 0 & 0 & 0 & 1 & 0 \\ 0 & 0 & 0 & 0 & 0 & 1 \end{bmatrix} \begin{bmatrix} p - b_x \\ q - b_y \\ r - b_z \\ b_x \\ b_y \\ b_z \end{bmatrix}; H = \begin{bmatrix} 1 & 0 & 0 & 0 & 0 & 0 \\ 0 & 1 & 0 & 0 & 0 & 0 \\ 0 & 0 & 1 & 0 & 0 & 0 \end{bmatrix} \tag{3-33}$$

In Eq. (3-33), *p*, *q*, and *r* are angular velocities measured from the gyro along the *x*, *y*, and *z* axes, respectively. Symbols of *s, c, t,* and *sc* are short form of sine, cosine, tangent, and secant, respectively. This process model is nonlinear since it contains trigonometric functions. Therefore, we use Jacobian values of the nonlinear model of $f(x)$ to replace state transition matrix (A), where the values in that matrix are obtained by applying the previous estimated states in the EKF process. In contrast, matrix H is the linear expression.

The measurement from the accelerometer which is used to calculate ϕ_a and θ_a as measurement variables, as shown in Eq. (3-34) and (3-35) is a common initialized leveling equation [14, 36].

$$\phi_a = a\tan_2(f_y, f_z) \tag{3-34}$$

$$\theta_a = a\tan\left(\frac{-f_x}{f_y s\phi_a + f_z c\phi_a}\right) \tag{3-35}$$

3.4.1.2 Error Covariance

In Fig. 3.17, the estimated error covariance is computed by $P_k = P_k^- - K_k H P_k^-$. Error covariance indicates the difference between state estimation ($\hat{\mathbf{x}}_k$) and the unknown true

state value ($\mathbf{x}_k$). It also can be defined as the following [34],

$$P_k = E\left\{\left(\mathbf{x}_k - \hat{\mathbf{x}}_k\right)\left(\mathbf{x}_k - \hat{\mathbf{x}}_k\right)^T\right\} \tag{3-36}$$

The error covariance of attitude states was initialized by calculating the angle variance using Eqs. (3-34) and (3-35). The rest of the error covariance of the bias states was approximated from gyro data. All the covariance were calculated using Eq. (3-37) and (3-38). Equation (3-37) was used to calculate the estimated mean value and Eq. (3-38) was used to calculate its covariance.

$$E\{\mathbf{n}_k\} = \frac{1}{N}\sum_{i=1}^{N}\mathbf{n}_{k_i} \tag{3-37}$$

$$\operatorname{cov}\{\mathbf{n}_k\} = \frac{1}{N}\sum_{i=1}^{N}(n_{k_i} - E\{\mathbf{n}_k\})(n_{k_i} - E\{\mathbf{n}_k\})^T \tag{3-38}$$

Where N is a number of samples and $\mathbf{n}_k$ is a vector of accelerometer data or gyro data on the *x, y*, and *z* axes.

All calculations were taken from IMU and placed on the table without movement for approximately one minute with sampling period *T = 0.05* [s]. Figure 3.18 shows the accelerometer and gyroscope signals in static conditions on all three axes. The

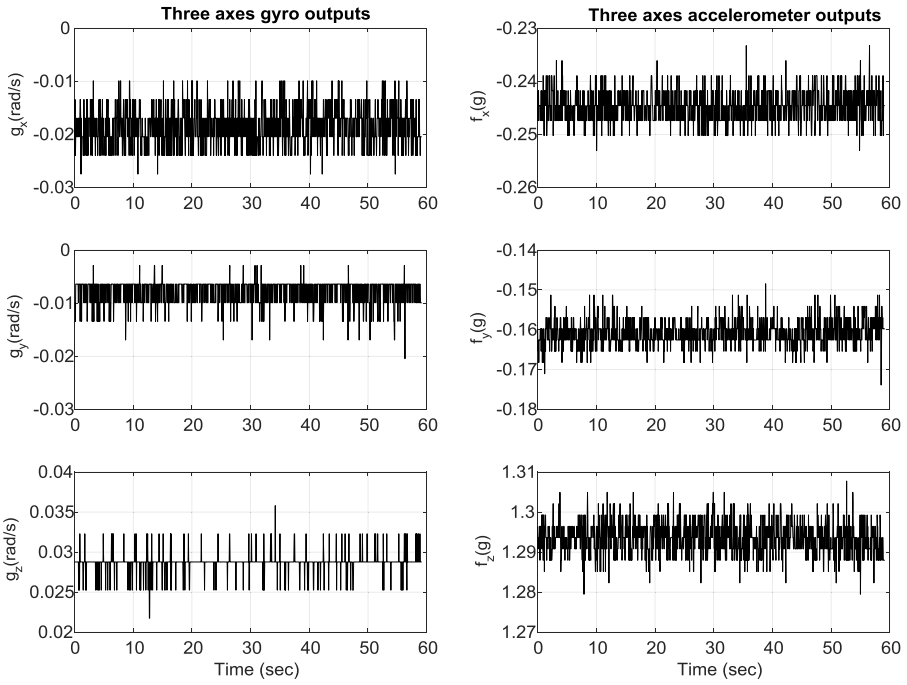

Figure 3.18 Three axes gyroscope and accelerometer in static condition [20].

experimentally determined variance values for attitude states are $\sigma_{\phi}^2 = 6.05x10^{-6}$ and $\sigma_{\theta}^2 = 4.98x10^{-6}$ in [rad^2]. And for the gyroscope along the *x, y,* and *z* axes, the values are $\sigma_{\mathrm{bx}}^2 = 0.046$, $\sigma_{\mathrm{by}}^2 = 0.018$, and $\sigma_{\mathrm{bz}}^2 = 0.005$ in [rad^2/s^2]. These values will be the diagonal elements of the initial P_k.

3.4.1.3 Initial Values and Covariance of the Noise

The initial value of the bias gyro was determined based on static IMU data in [rad/s] unit. The initial value for attitude states was chosen as one degree for each state. The initial states value in EKF model is as follows:

$$\mathbf{x}_{k=1} = \begin{bmatrix} \phi & \theta & \psi & b_x & b_y & b_z \end{bmatrix}^T = \begin{bmatrix} 1 & 1 & 1 & -0.019 & -0.008 & 0.029 \end{bmatrix}^T \qquad (3\text{-}39)$$

Since the noise is assumed to be in normal distribution and independent on each axis, the variance of noise **w***(t)* and **v***(t)* is used. Noise process matrix (Q) was selected as q_{11}, q_{22}, and q_{33} are 1, and q_{44}, q_{55}, and q_{66} are 0.3. These values were chosen because it produced the best estimation result in the experiment.

The measurement noise covariance matrix (R_{nom}) is defined by Eq. (3-40) and the measurement comes from the attitude in Eq. (3-34) and (3-35); however, the measurement noise covariance matrix is obtained by calculating the variance of accelerometer signal through Eqs. (3-37) and (3-38). These signals have a direct relation to the attitude measurement.

$$R_{nom} = E[\mathbf{v}_k \quad \mathbf{v}_k^T] \qquad (3\text{-}40)$$

To determine the diagonal element of R_{nom}, the variance of f_x, f_y, and f_z, are calculated: $r_{11} = 9.04x10^{-6}$, $r_{22} = 1.04x10^{-5}$, and $r_{33} = 1.80x10^{-5}$ [G^2]. Since the accelerometer is sensitive to disturbances, finally we tuned the value of R_{nom} and keep the same R_{nom} value in other experiment types.

The above process and measurement models construct the procedure of the EKF as follows:

1. Set the initial values for states and error covariance

   $\hat{\mathbf{x}}_0$, P_0

2. Predict states and error covariance

$$\hat{\mathbf{x}}_k^- = f(\hat{\mathbf{x}}_{k-1})$$
$$P_k^- = AP_{k-1}A^T + Q$$

3. Compute the Kalman gain

$$K_k = P_k^- H^T (HP_k^- H^T + R)^{-1}$$

4. Compute the states estimate

$$\hat{\mathbf{x}}_k = \hat{\mathbf{x}}_k^- + K_k(\mathbf{z}_k - H\hat{\mathbf{x}}_k^-)$$

5. Compute the error covariance

$$P_k = P_k^- - K_k HP_k^-$$

3.4.2 External Acceleration Compensation Model

In this section, the method for compensating the external acceleration will be introduced. The method is based on the view that external acceleration is a disturbance in the original signal, and therefore should be removed from the original signal. The disturbance rejection model was derived from a control ratio model [35]. From this point on, the term "compensation model" will be used to replace the term "disturbance rejection model." The three-axes accelerometer data is input for the compensation model. Each axis will be treated in the same step; therefore, for the simplicity, only the *x*-axis will be discussed. In Eq. (3-41), ideally the compensated *x*-axis accelerometer signal (f^*x_k) was determined by subtracting the compensation model in the *x*-axis (a_k) from the original signal (fx_k).

$$f^*x_k = fx_k - a_k \tag{3-41}$$

The external acceleration (a_k) is extracted from (fx_k) by the compensation model. Figure 3.19 shows the ideal model diagram of Eq. (3-41). However, due to the dynamism of the system and many uncertainties, there is no ideal model. Consequently, we will use the result of the compensation model as one parameter for adjusting the noise covariance matrix in sensor fusion in the next section. The design approach for a compensation model is based on the specification that the model should not be affected by the disturbance input, *d(t)*. In other words, the steady-state output should be zero if

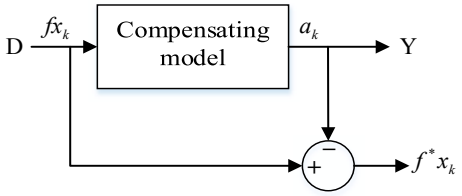

Figure 3.19 The input-output diagram of external acceleration compensation.

possible or a small constant, $y(t)_{ss} = 0$, $d(t) \neq 0$. A control ratio in the s domain [35] is commonly written as follows:

$$\frac{Y(s)}{D(s)} = \frac{K\left(s^w + c_{w-1}s^{w-1} + \ldots + c_1 s + c_0\right)}{s^n + q_{n-1}s^{n-1} + \ldots + q_1 s + q_0} \tag{3-42}$$

Assuming a step disturbance signal $D(s) = D_0/s$, the output will be

$$Y(s) = \frac{KD_0\left(s^w + c_{w-1}s^{w-1} + \ldots + c_1 s + c_0\right)}{s\left(s^n + q_{n-1}s^{n-1} + \ldots + q_1 s + q_0\right)} \tag{3-43}$$

Where K is gain constant, $K > 0$, c and q are constant coefficients, and D_0 is the final value of step disturbance. The condition $y(t)_{ss} = 0$ will be achieved if $c_0 = 0$ and requires the numerator of $Y(s)/D(s)$ have at least one zero at the origin of the s-plane. On the other side, the location of the poles on the s-plane determined its corresponding response. To produce the damped response, the poles should be on the left–half of s-plane. There are two possibilities for poles locations on the left-half side, such as complex-conjugate poles and real poles, which have the output characteristics of exponentially damped sinusoid and damped exponential, respectively. In this model, the damped exponential response is chosen because the disturbance should be suppressed without a sinusoidally oscillating component. Finally, the transfer function of the model is determined as: there is one zero at the origin and one real pole on the left-half of the s-plane, which is based on Eq. (3-42) and becomes as follows:

$$\frac{Y(s)}{D(s)} = \frac{K\,s}{s + q_0} \tag{3-44}$$

The compensating model in Eq. (3-44) attenuates low frequencies and as a result a high frequency signal is obtained. This is in line with the fact that the external acceleration occurs when the change of velocity in magnitude and/or direction of each axis exceeds a certain limit.

The analysis of the stability of model Eq. (3-44) will be introduced in the time domain as follows. In the time domain, the stability will be achieved based on the principle that there is a limited response to the limited input. The discussion of the time-response of singularity input functions to this model, such as step, ramp, rectangular pulse, and parabolic functions are as follows.

The time response model Eq. (3-44) for a unit step input, $u(t)$, is $y(t) = Ke^{-q_0 t}$. The steady-state response for $y(t)$ and the steady-state error as in Eq. (3-45) and (3-46), respectively.

$$y(t)_{ss} = \lim_{t\to\infty} K\, e^{-q_0 t} = 0 \tag{3-45}$$

$$err(t)_{ss} = \lim_{t\to\infty} (1 - K\, e^{-q_0 t}) = 1 \tag{3-46}$$

The time response for ramp input ($d(t)=t$) is $y(t) = K / q_0 \left(1 - e^{-q_0 t}\right)$. The steady-state output and error is calculated as follows:

$$y(t)_{ss} = \lim_{t\to\infty} \frac{K}{q_0}\left(1 - e^{-q_0 t}\right) = \frac{K}{q_0} \tag{3-47}$$

$$err(t)_{ss} = \lim_{t\to\infty} \frac{K}{q_0}\left(e^{-q_0 t} - 1\right) + t = \infty \tag{3-48}$$

A rectangular pulse of amplitude *1/a* and of duration *a*, $d(t) = \dfrac{u(t) - u(t-a)}{a}$, has a *zero* steady-state output and also a *zero* steady-state error.

For a parabolic function input, $d(t)=0.5t^2$, the time response is calculated as in Eq. (3-49), with an infinity steady-state output and infinity steady-state error.

$$y(t) = \frac{K}{q_0} t + \frac{K}{q_0^{\,2}}\left(e^{-q_0 t} - 1\right) \tag{3-49}$$

These four kinds of singularity inputs and their combination represent the possibility of disturbance waveforms. All of them have the tendency to be rejected and damped by model Eq. (3-44). The response of the parabolic input has not shown constant steady-state output; however, it represented the exponentially damped factor. Figures 3.20 (a, b, c, and d) illustrate all time responses for each basic input signal, using model Eq. (3-44) within *K=1*. Each figure has two outputs, i.e., $y_1(t)$ and $y_2(t)$, where q_0 in $y_1(t)$ is greater than q_0 in $y_2(t)$.

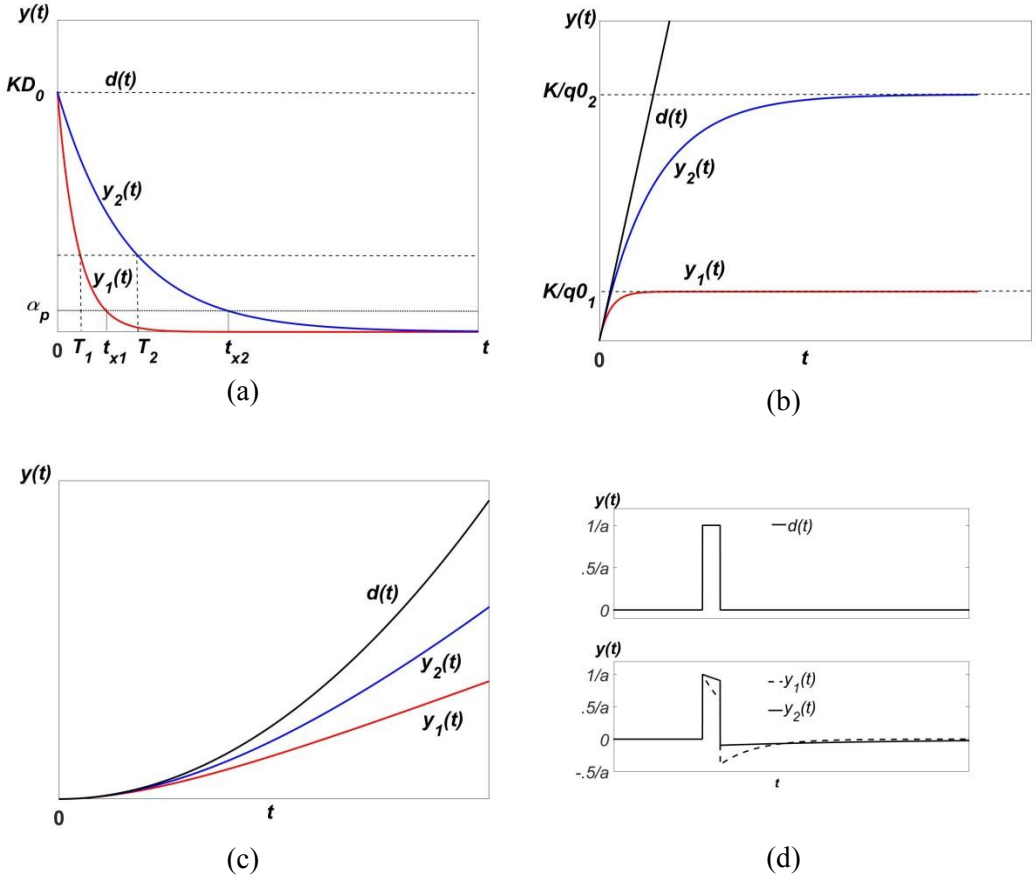

Figure 3.20 Time response plot corresponding to compensation model in Eq. (3-44) for some basic input signals: (a) step function, (b) ramp, (c) parabolic, and (d) pulse. Model parameter q_0 in $y_1(t)$ is greater than q_0 in $y_2(t)$ [20].

3.4.3 Proposed EKF using the Compensation Model (*Mode 2*)

In this subsection, the implementation of the external acceleration compensation method will be discussed. The result of the compensation model will be used to modify parameter in the Kalman filter. The step of filtering algorithm is the same as the previous standard EKF but the modification occurs on the Eq. (3-40) depend on the results of the external acceleration model.

Related to the proposed model in Eq. (3-44), the result of this model, which is called a_k , is uncorrelated to noise v_k, and the discrete form of R is now modified to be as follows

$$R_k = R_{nom} + \lambda \mathbf{a}_k^2 \tag{3-50}$$

The λ is a constant coefficient which was experimentally chosen by testing a range of trial and error that gives satisfactory result. In *Mode 1*, λ is set to zero, therefore there is no compensation of external acceleration. Particularly in *Mode 2*, R is tuned based on

the external acceleration model and $\mathbf{a}_k^2$ is the element of the diagonal matrix, which consists of a_y^2, a_x^2, and a_z^2. The diagonal matrix of $\mathbf{a}_k^2$ in Eq. (3-50) plays a key role in compensating for the external acceleration by increasing the R_k value. During static conditions or slow movement (i.e., $\mathbf{a}_k^2 \approx 0$), the covariance matrix will be the same as R_{nom}.

3.4.4 Different Method of External Acceleration Compensation as Comparisons

Some researchers have been worked to minimize the effect of external acceleration as has been shown in the Table 2.2. In this study, three comparisons method have been developed, which will be called as *Mode 3, Mode 4,* and *Mode 5*.

3.4.4.1 Two-Step EKF (*Mode 3*)

The two-step EKF in [10] used separate measurements between the gyro and accelerometer. The external acceleration compensation technique is based on *weighted-switching* in setting the noise covariance of those measurements was proposed by Suh et al.

The state $\mathbf{x}(t)$ for *Mode 3* is $\mathbf{x}(t) = [\theta \ \phi \ p \ q \ r]^T$ and the measurement variable $\mathbf{z}(t)=[f_x \ \ f_y \ \ p \ \ q \ \ r]^{\mathrm{T}}$. The system equation is given by

$$\dot{\mathbf{x}}(t) = A(t)\mathbf{x}(t) + \mathbf{w}(t) \tag{3-51}$$

$$\mathbf{z}(t) = f(x(t)) + \mathbf{v}(t) \tag{3-52}$$

Where

$$A(t) = \begin{bmatrix} 0 & 0 & 0 & c\phi & -s\phi \\ 0 & 0 & 1 & s\phi\, t\theta & \mathrm{c}\phi\, t\theta \\ 0 & 0 & 0 & 0 & 0 \\ 0 & 0 & 0 & 0 & 0 \\ 0 & 0 & 0 & 0 & 0 \end{bmatrix} \qquad f(x(t)) = \begin{bmatrix} s\theta \\ s\phi c\theta \\ p \\ q \\ r \end{bmatrix} \tag{3-53}$$

In *Mode 3*, there will be a setting for the measurement noise covariance matrix, in which r_1 and r_2 belong to the accelerometer and r_3 belongs to the gyroscope, as in Eq. (3-54).

$$R = \begin{bmatrix} r_1 & 0 & 0 & 0 & 0 \\ 0 & r_2 & 0 & 0 & 0 \\ 0 & 0 & r_3 & 0 & 0 \\ 0 & 0 & 0 & r_3 & 0 \\ 0 & 0 & 0 & 0 & r_3 \end{bmatrix} \tag{3-54}$$

The two-step measurement updated Kalman Filter was used to update the Kalman gain, state estimation, and measurement noise covariance matrix. *First*, the measurement was updated only for variance of the error measurement in the gyroscope (r_3). *Second*, the measurement was updated for r_1 and r_2 using a *weighted-switching* rule as in Eq. (3-57), based on the threshold rule of Eq. (3-56) to detect external acceleration. The threshold rule is derived from a necessary condition for acceleration free movement, as in Eq. (3-55). The *weighted-switching rule* works on the principle that when there is external acceleration, the gyroscope outputs should be trusted more. This can be done by making r_1 and r_2 larger. For a more detailed explanation, the discussion is in [10].

$$f_x^2 + f_y^2 + f_z^2 = 1 \tag{3-55}$$

$$\left| f_x^2 + f_y^2 + f_z^2 - 1 \right| > \delta \tag{3-56}$$

$$\begin{bmatrix} r_{1,k} \\ r_{2,k} \end{bmatrix} = \max\left(\alpha_1 \begin{bmatrix} r_{1,k-1} \\ r_{2,k-1} \end{bmatrix} + \alpha_2 \left(\mathbf{z}_{k,1} - C_{1,k} \hat{x}_{k,g} \right), \begin{bmatrix} r_{1,nom} \\ r_{2,nom} \end{bmatrix} \right) \tag{3-57}$$

where f_x, f_y, f_z : accelerometer output; δ : threshold; α_1 and α_2 are scalar parameters; $C_{1,k}$ is the partition of the Jacobian matrix of $f(x(t))$.

3.4.4.2 Threshold-based External Acceleration Compensation (*Mode 4*)

Mode 4 is proposed by Sabatini et al. [16] using quaternion-based EKF. The discrete state for *Mode 4* is composed of the rotation quaternion ($\mathbf{q}$), accelerometer ($^{a}\mathbf{b}$), and magnetometer ($^{m}\mathbf{b}$) bias vectors $\mathbf{x}_{k+1} = [\mathbf{q}_{k+1} \;\; {}^{a}\mathbf{b}_{k+1} \;\; {}^{m}\mathbf{b}_{k+1}]^{T}$. The measurement model is constructed by accelerometer and magnetometer measurement vectors $\mathbf{z}_{k+1} = [\mathbf{a}_{k+1} \;\; \mathbf{m}_{k+1}]^{T}$. The mechanism of adaptation of the measurement noise covariance matrix of acceleration is implemented using a *threshold-based* approach.

$${}^{R}\sigma_a^2 = \begin{cases} \sigma_a^2, \left\| \|\mathbf{a}_{j+1}\| - \|\mathbf{g}\| \right\| < \varepsilon_{th} & \forall j \in [k - k_a, k] \\ \infty, otherwise \end{cases} \tag{3-58}$$

where ε_{th} : accelerometer threshold; $\mathbf{a}_{\mathrm{j}}$: accelerometer output; and ${}^{R}\sigma_a^2$: measurement variance.

The measured acceleration magnitude is tested in advance to recognize deviations from gravity. If there is deviation greater than the threshold, the observation variance ${}^{R}\sigma_a^2$ is set to a high value.

3.4.4.3 Threshold-based Combined with Softened Part (*Mode 5*)

Mode 5 is proposed by Harada et al. [17] using quaternion-based unscented Kalman filter (UKF). The method is threshold-based combined with a softened part of the measurement covariance matrix adaptation. The output of the accelerometer is detected as reliable if it satisfies the condition: $\left\|\left\|\mathbf{a}_{\mathrm{k}}\right\|-\left\|\mathbf{g}\right\|\right\|<\varepsilon_{th}$, where $\mathbf{a}_{\mathrm{k}}$ is the output of the accelerometer on the body frame. The mechanism of the adaptation of the measurement covariance matrix is as follows:

$$\sigma_{a,k}^2=\sigma_{a0}^2+\alpha_a\left\|{}^{\mathrm{b}}\mathbf{a}_{\mathrm{k}}-{}^{b}\mathbf{g}_k\right\|^2 \tag{3-59}$$

Where σ_{a0} is the offset and $\alpha_a\left\|{}^{\mathrm{b}}\mathbf{a}_{\mathrm{k}}-{}^{b}\mathbf{g}_k\right\|^2$ is the softened part of the adaptation mechanism. The ${}^{b}\mathbf{g}_k$ is the predicted acceleration that comes from $R(\mathbf{q}).\mathbf{g}$. If the orientation quaternion $\mathbf{q}=\left[\mathbf{e}^T,q_4\right]$, where $\mathbf{e}=\left[q_1,q_2,q_3\right]^T$ is the vector part and q_4 is the scalar part of the quaternion, then

$${}^{b}\mathbf{g}_k=\frac{1}{\sqrt{\left\|\mathbf{e}\right\|^2+q_4^2}}\begin{bmatrix}2(q_1q_3-q_2q_4)\\2(q_2q_3-q_1q_4)\\-q_1^2-q_2^2+q_3^2+q_4^2\end{bmatrix} \tag{3-60}$$

3.5 Implementation Results

3.5.1 Various Test Conditions and Statistical Analysis

There will be three tests in each mode, aimed at studying the performance under various dynamic conditions, which are Test A, Test B, and Test C. Test A is a one direction test, Test B is a multidirectional test, and Test C is a walking test.

Test A was performed by placing the IMU sensor on the slider table of a MISUMI RSH3 single-axis robot. By moving the slider back and forth with the robot controller, external acceleration is applied on the *x*-axis of the IMU sensor. Test A intended to test proposed method on the lateral movement as is done in [10], which will affect the pitch angle. In Test A, we conducted the trial by using such conditions as follows: 1) four acceleration coefficients in ascending order from the MISUMI software settings, i.e., 0.1, 0.75, 1.5, and 2.5 [m/s^2]; 2) four q_0 parameter values, i.e., 0.5, 0.1, 0.05, and 0.01; 3) six λ values, i.e., 35, 80, 100, 150, 170, and 200. The independent-samples Kruskal-Wallis test was conducted to determine if there were differences in MSE value between categories. Next, the nonparametric multiple comparisons Steel-Dwass and or Dunn all pairs for joint ranks were conducted to interpret all pairwise comparisons.

Test B involved movement using free hand in the *x* and *y*-axes of the IMU as perform in the previous study [18]. The movement along the *x*-axis was considered as roll and the movement along the *y*-axis was considered as pitch angle. In contrast with Test A, Test B was performed using external acceleration on a combination of axes.

Test C was executed based on the application of attitude estimation on a shoe-type measurement device. An IMU sensor was placed on the top of one shoe. The subject was asked to walk straight, 3-4 strides, at a normal speed. The IMU placement comes from the result of the study in subsection 3.3.

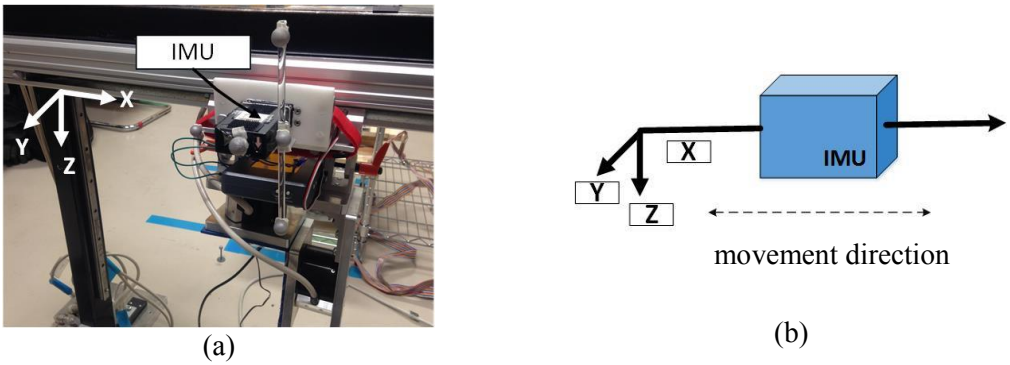

(a) (b)

Figure 3.21 Test A set-up for validating attitude estimation. (a) The RSH3 table slider moves along the *x*-axis, (b) The illustration of the movement direction.

3.5.2 Test Setup

To verify and validate the proposed method, all tests were conducted using an IMU sensor consisting of an accelerometer (±16 [G]), a gyro (±1500 [deg/s]), and a magnetometer (±0.9 [Ga]) (from Logical Product, Japan). Sensor data were transmitted to the PC wirelessly. A combination of NI LabVIEW® and Simulink® was used for data acquisition and the MATLAB® program was used to execute the proposed method.

In Test A, the MISUMI RSH3 single-axis robot (from MISUMI Group Inc., Japan) had a max. speed of 300 [mm/s], an effective stroke of 500 [mm] and was controlled by the RS-Manager support software used as a testbed, as in Fig. 3.21 (a). Figure 3.21 (b) is an illustration of movement direction on the Test A. Note that the attitude is not changed because the IMU sensor was moving in a lateral direction without rotation; that is, in order to validate the proposed method, the reference values are $\theta = 0^o$ and $\phi = 0^o$.

In Test B, the IMU sensor was placed in plastic jar surrounded by styrofoam to avoid magnetic interference between the IMU and the electromagnetic motion tracking system receiver (Fastrak® from Polhemus Inc., USA). The Fastrak® as the reference is used by recording the roll and pitch angles of the receiver using C# data acquisition program. Fastrak® attitude data were transmitted to the PC via a cable using an RS-232 protocol as shown in Fig. 3.22.

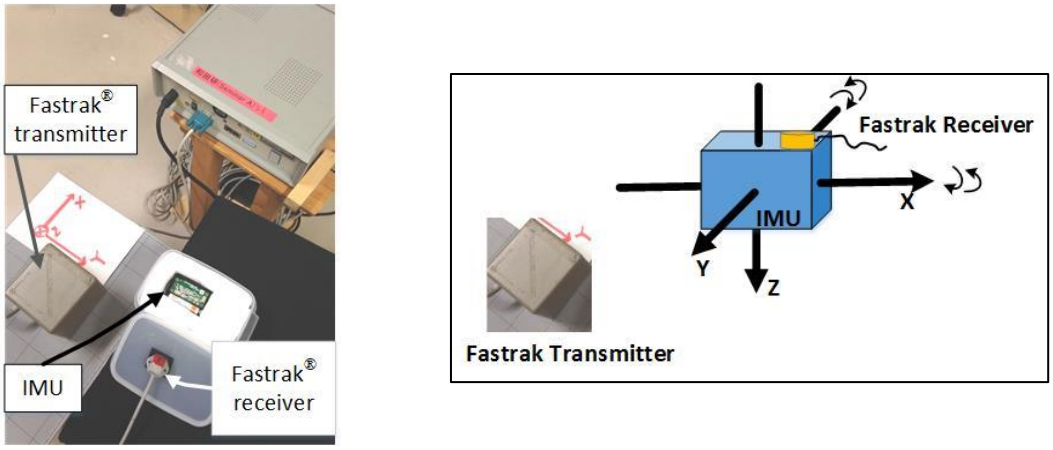

(a) (b)

Figure 3.22 Test B set-up. (a) Fastrak® attitude reference system and IMU inside a plastic jar; (b) The illustration of the movement direction.

In Test C, the IMU sensor was mounted on the shoe based on the study in the subsection 3.3. For a reference measurement, the experiment setup contained six OptiTrack® cameras, and four reflective markers were placed at the fore foot and heel. Figure 3.23 (a and b) shows the measurement set-up for validating Test C. In Tests B

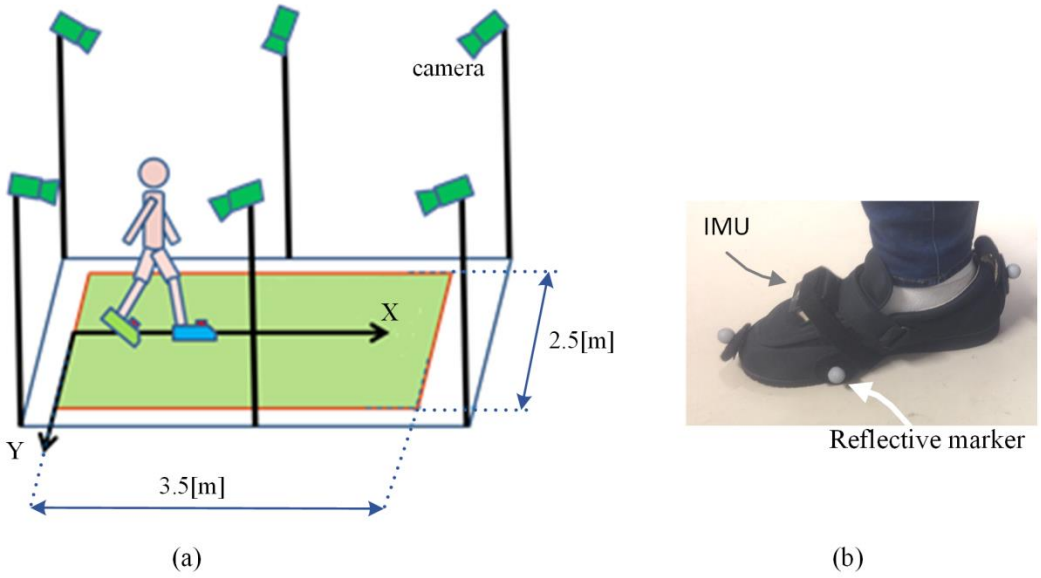

Figure 3.23 Measurement set-up for Test C. (a) room set-up for recording the attitude; (b) four reflective markers were placed on the forefoot and heel [20].

and C we calculated cross-correlation in order to compare references and IMU data from different data acquisition programs. The time when the correlation was maximal will be used to synchronize both measurements. To accomplish time normalization between the reference and the IMU sensor, cubic spline data interpolation was employed.

The quantitative performance assessment for Test A, Test B, and Test C is using mean squared error (MSE or *S*) in [degree^2], and maximum error (*M*) in [degree] between predicted attitude and reference attitude as described in Eqs. (3-61) and (3-62), respectively.

$$S_\theta = \frac{1}{N}\sum_{k=1}^{N}\left(\hat{\theta}(kT)-\theta(kT)\right)^2 \tag{3-61}$$

$$M_\theta = \max_k\left|\hat{\theta}(kT)-\theta(kT)\right| \tag{3-62}$$

3.5.3 Experiment Results of Test A

Mode 1 is not related to the compensation model in Eq. (3-44) because it used standard EKF algorithm, while the measurement noise covariance in Eq. (3-50) was set to R_{nom} = 1.5, which was experimentally chosen since it produced the best estimation result, and $\lambda = 0$. As with *Mode 1*, the compensation model was not used in *Mode 3*, the constant parameters were chosen based on the best estimation result; i.e., δ = 0.1 [G^2],

Table 3.8 Test A: MSE (S) of *Mode 1*, *Mode 3*, *Mode 4*, and *Mode 5* in detail, presented in [deg^2].

Acc	*Mode 1*		*Mode 3*		*Mode 4*		*Mode 5*	
[m/s^2]	Pitch	Roll	Pitch	Roll	Pitch	Roll	Pitch	Roll
0.1	9.60	2.92	9.31	2.71	99.42	26.73	9.04	2.89
0.75	24.77	3.22	24.66	3.20	92.56	183.10	22.92	2.82
1.5	29.79	3.59	29.41	4.02	113.20	227.13	28.79	2.86
2.5	36.84	4.88	34.49	5.60	44.94	168.43	33.82	4.03
mean(sd)	25.25	3.65	24.47	3.88	87.53	151.35	23.64	3.15
	(10)	(0.8)	(9.4)	(1.1)	(25.7)	(75.1)	(9.3)	(0.5)

α_1 = 0.4, and α_2 = 80. In *Mode 4,* the threshold ε_{th} used is 0.02 and σ_a^2=1.5 as used in *Mode 1* and *Mode 2*. To meet the mechanism of external acceleration Eq. (3-59) in *Mode 5*, σ_{a0}^2 is 1.5, which is the same value as we used in *Mode 1* and *Mode 2*. The α_a is determined to be 5, which comes from experiments using a range of α_a = 2 to 10 that gives the smallest MSE. The MSE will decrease in value when α_a becomes greater, although the MSE decrease is smooth; it is in line to the function of α_a as the softened part of adaptation mechanism.

Overall the results of *Modes 1, 3, 4*, and *5* are shown in Table 3.8. The mean MSE of *Mode 5* is the lowest among *Modes 1, 3*, and *4*; i.e., 23.64 and 3.15 [deg^2] for pitch and roll, respectively.

The experiment result of *Mode 2* is as follows, for the purpose of looking at the effect of the reduction of external acceleration, the *Mode 2* experiment was performed using a different compensating parameter value. Table 3.9 concludes the result by showing the average MSE of the attitude estimation from four different accelerations, with some variation in the values of q_0 and λ. The variation value of q_0 is 0.5, 0.1, 0.05, and 0.01, all of them using $K = 1$. While the variation value of λ is 35, 80, 100, 150, 170, and 200, in ascending order; the value settings of the EKF parameters are R_{nom} = 1.5, which is the same as we used in *Mode* 1 and *Mode* 3.

Table 3.9 Test A: MSE of *Mode 2* during the variability of q_0 and λ, presented as mean (standard deviation).

MSE	q_0	λ= 35	λ= 80	λ= 100	λ= 150	λ= 170	λ= 200
Pitch [deg^2]	0.5	15.28 (6.95)	12.94 (5.86)	12.31 (5.56)	11.2 (5.02)	10.86 (4.86)	10.44 (4.65)
	0.1	13.77 (6.11)	11.52 (5.08)	10.93 (4.80)	9.89 (4.30)	9.58 (4.15)	9.17 (3.94)
	0.05	13.50 (6.04)	11.29 (5.02)	8.9 (5.88)	9.67 (4.23)	9.35 (4.07)	8.94 (3.86)
	0.01	13.13 (6.12)	10.94 (5.06)	10.36 (4.76)	9.31 (4.21)	8.99 (4.03)	**8.57 (3.81)**
Roll [deg^2]	0.5	2.62 (0.96)	2.32 (1.02)	2.25 (1.04)	2.13 (1.09)	2.10 (1.10)	2.07 (1.12)
	0.1	2.39 (1.00)	2.11 (1.07)	2.04 (1.09)	1.94 (1.12)	1.91 (1.13)	1.87 (1.14)
	0.05	2.27 (1.02)	1.99 (1.08)	1.81 (1.20)	1.82 (1.11)	1.79 (1.12)	1.75 (1.12)
	0.01	1.91 (1.04)	1.67 (1.08)	1.62 (1.09)	1.53 (1.10)	1.51 (1.10)	**1.48 (1.11)**

As shown in Table 3.9, the relationship between λ and q_0 in one-axis movement test is as follows. The MSE trend decreases as the value of λ increases or q_0 decreases. The best combination for one-axis movement in this experiment is λ = 200 and q_0 = 0.01, the MSE is 8.57 and 1.48 [deg^2] for pitch and roll, respectively.

Figures 3.24 (a) to (j) shows example of the attitude estimation. We choose the largest acceleration of the MISUMI table slider (2.5 [m/s^2]) in this test as a figure of attitude example. As can be seen, the *Mode 2* (as compared to *Modes 1*, *3, 4,* and *5*) has the smallest MSE; i.e., 13.47 [deg^2].

Table 3.10 concludes the MSE result of Test A for all modes. By using the value λ = 200 and q_0 = 0.01, *Mode 2* has the lowest MSE among the modes.

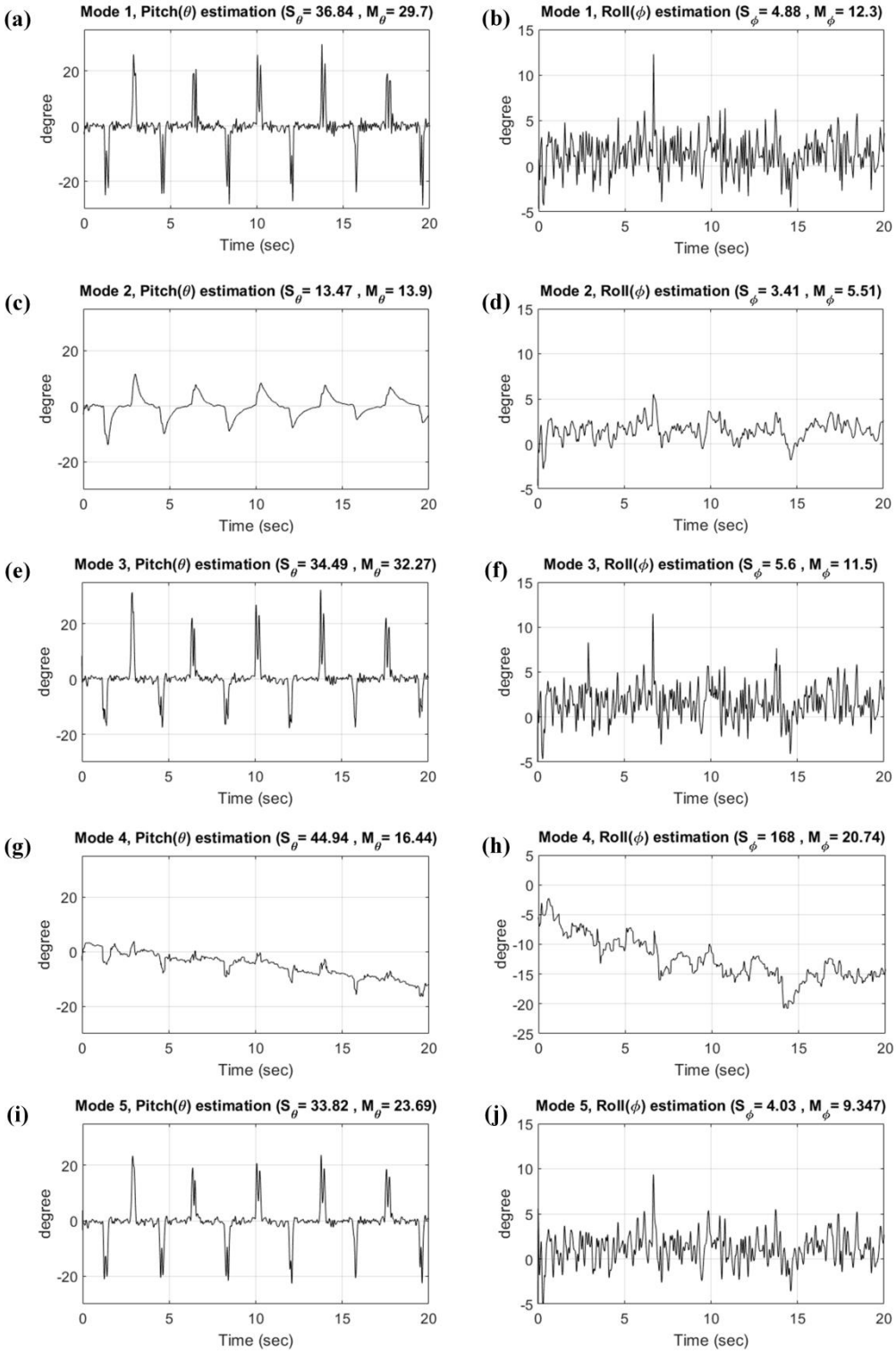

Figure 3.24 The MSE (S) in [deg^2] and maximum error (M) in [deg] of pitch and roll estimation by five modes in Test A, acceleration = 2.5 [m/s^2]. Specifically for *Mode 2*: q_0= 0.05, λ=150. *Mode 1* in (a) and (b), *Mode 2* in (c) and (d), *Mode 3* in (e) and (f), *Mode 4* in (g) and (h), and *Mode 5* in (i) and (j) [20].

Table 3.10 Test A: MSE of all modes, presented as mean (standard deviation).

MSE	Mode 1	Mode 2	Mode 3	Mode 4	Mode 5
Pitch [deg^2]	25.25 (10)	8.57 (3.8)	24.47 (9.4)	87.53 (25.7)	23.64 (9.3)
Roll [deg^2]	3.65 (0.8)	1.48 (1.1)	3.88 (1.1)	151.35(75.1)	3.15 (0.5)

3.5.4 Experiment Results of Test B

Test B was executed by rotating the IMU sensor in a random manner by hand along the *x* and *y*-axis. In order to determine the optimal q_0 value for *Mode 2*, we conduct the variability of the q_0 test to calculate the MSE and maximum error along the timeline of the whole experiment. Table 3.11 presents the MSE and maximum errors using different values of q_0. It found that $q_0 = 0.05$ has an optimum performance among all the possible choices.

Figures 3.25(a), 3.25(b), and 3.25(c) show the influence of q_0 variability to the square-output of the proposed compensation model a_k, as in the proposed model of *Mode 2* in Eqs. (3-44) and (3-50). Figures 3.26 (a) to (f), Figs. 3.27 (a) to (d), and Figs.

Table 3.11 Test B: MSE (S) (in [deg^2]) and maximum error (M) (in [deg]) of attitude estimation of *Mode 2* at various values of q_0 during all periods of time.

q_0	*Mode 2*			
	S_θ Pitch	S_ϕ Roll	M_θ Pitch	M_ϕ Roll
0.01	13.92	11.54	11.91	**13.92**
0.03	13.21	**11.48**	11.44	14.19
0.05	**13.14**	11.58	**11.42**	14.42
0.1	13.70	11.96	12.63	14.92
0.15	14.48	12.23	13.93	15.28
0.2	15.14	12.45	14.81	15.54
0.25	15.68	12.62	15.40	15.73
0.3	16.11	12.76	15.86	15.90

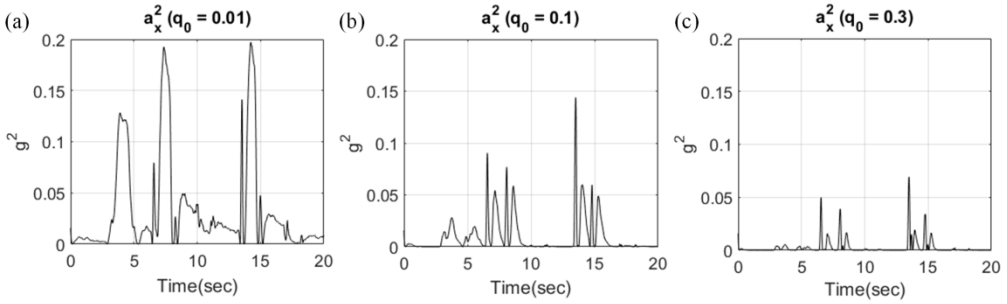

Figure 3.25 Graphs of the square of compensation model output of various value of q_0 along the x-axis: (a) q_0=0.01, (b) q_0=0.1, (c) q_0=0.3 [20].

3.28 (a) to (l) are produced by using this parameter value to present the analysis and the result of attitude estimation.

Figures 3.26 (a, b, and c) present the accelerometer signal and Figs. 3.26 (d, e, and f) present the compensation model signal along the x, y, and z-axis of the accelerometer, using model parameter $K = 1$ and $q_0 = 0.05$. When the sensor is not experiencing external acceleration, the compensating signal tends to be around zero. While the sensor is being moved quickly, it experiences two major external acceleration periods along the

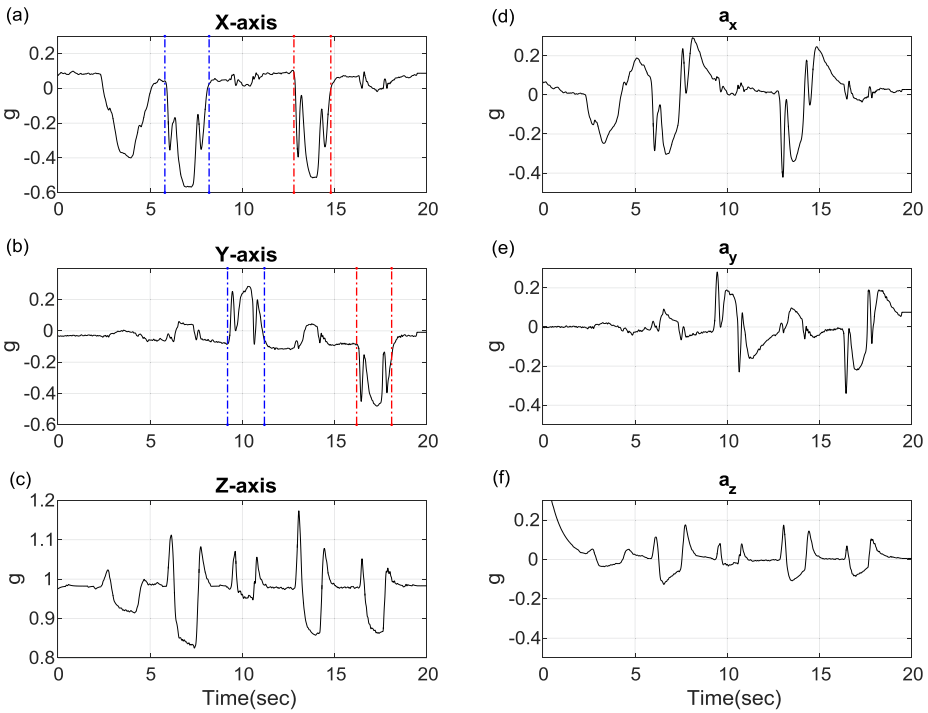

Figure 3.26 External acceleration compensation: original accelerometer signal is shown in (a), (b), and (c); Compensation model output is shown in (d), (e), and (f) along the x, y, z-axis respectively. In (a), the dash-dot line indicates *phase I* and *II*, respectively; while in (b), the dash-dot line indicates *phase III* and *IV*, respectively [20].

x and *y*-axes as shown in Figs. 3.26 (a and b). In Fig. 3.26(a), we call the periods *Phase I* and *Phase II* (indicated by the dash-dot line); *Phase I* for 2.4 [s] during 5.8–8.2 [s] and followed by *Phase II*, 2 [s] during 12.8–14.8 [s]. Observing along the *y*-axis in Fig. 3.26(b), we use *Phase III* and *Phase IV* (indicated by the dash-dot line) to refer to the external acceleration experienced for 2 [s] during 9.2–11.2 [s] and 1.9 [s] during 16.2–18.1 [s], respectively. The external acceleration during *Phases I* and *II* is closely related to the pitch angle while the *Phases III* and *IV* are related to the roll angle.

Mode 2 works as based on an automatically adjusted measurement noise covariance matrix as on Eq. (3-50). The square of compensation model output was needed to adjust the measurement error covariance matrix and the squared signal output shown in Figs. 3.27 (a, b, and c). The timing of the occurrence of the enlarged amplitude of the square of the signal is aligned with the timing of the external acceleration in *phases I* to *IV*. This means that R_k in Eq. (3-50) will increase during the dynamic condition of this phase. While Fig. 3.27(d) presents the necessary condition of *Mode 3* as a comparison.

Parameter values are used in each mode in Test B. *Mode 1* uses R_{nom} = 1.5, while *Mode 2* uses q_0 = 0.05, R_{nom} = 1.5, and λ= 3.5. *Mode 3* uses threshold δ = 0.1 [G^2], α_1 =

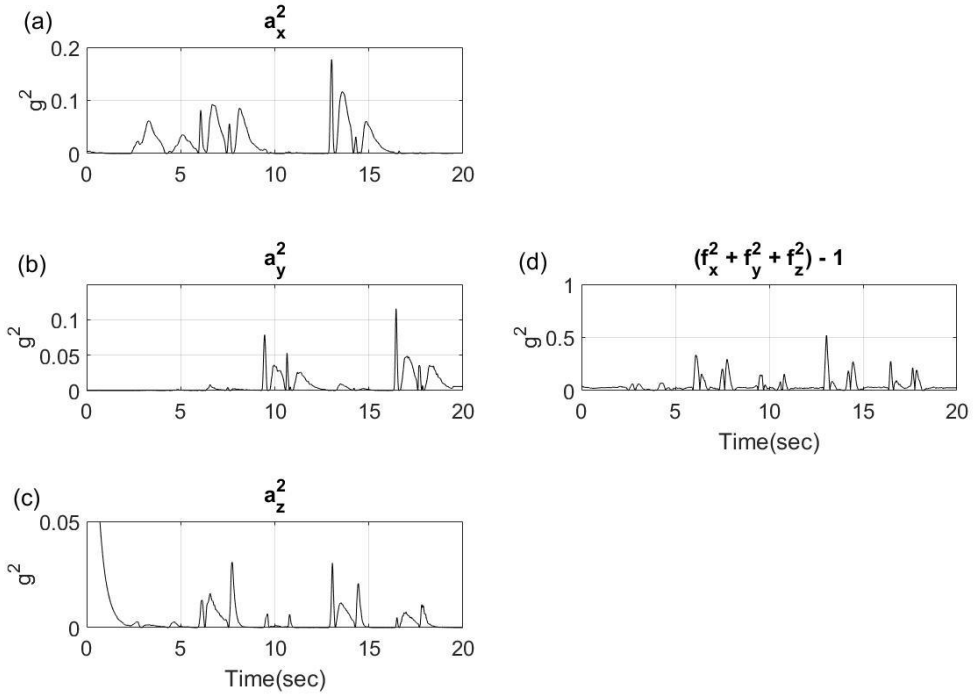

Figure 3.27 (a), (b), (c): Graphs of the square of compensation model output for *x*, *y*, and *z*-axis of *Mode 2*. As a comparison is shown in (d): necessary condition of *Mode 3* [20].

0.4, α_2 = 0.3, and (r_1 = 0.093, r_2 = 0.034, and r_3 = 1.5). *Mode 4* uses the threshold ε_{th} = 0.1 and σ_a^2 = 0.3. We did experiments with some value of σ_a^2: 0.2, 0.3, and 0.4; the σ_a^2 = 0.3 produced a minimum MSE. *Mode 5* works using σ_{a0}^2 = 1.5 and the factor of softened part α_a = 3. All parameters value in these modes was determined using the similar value from the previous test; however, the value of some parameters has been changed in order to give satisfactory result. One of the results of Test B using five modes is presented in Figs. 3.28 (b, c, d, e, and f) for pitch and Figs. 3.28 (h, i, j, k, and l) for roll estimation. Also the attitude reference signal from Fastrak® is shown in Figs. 3.28 (a and g) for pitch and roll, respectively.

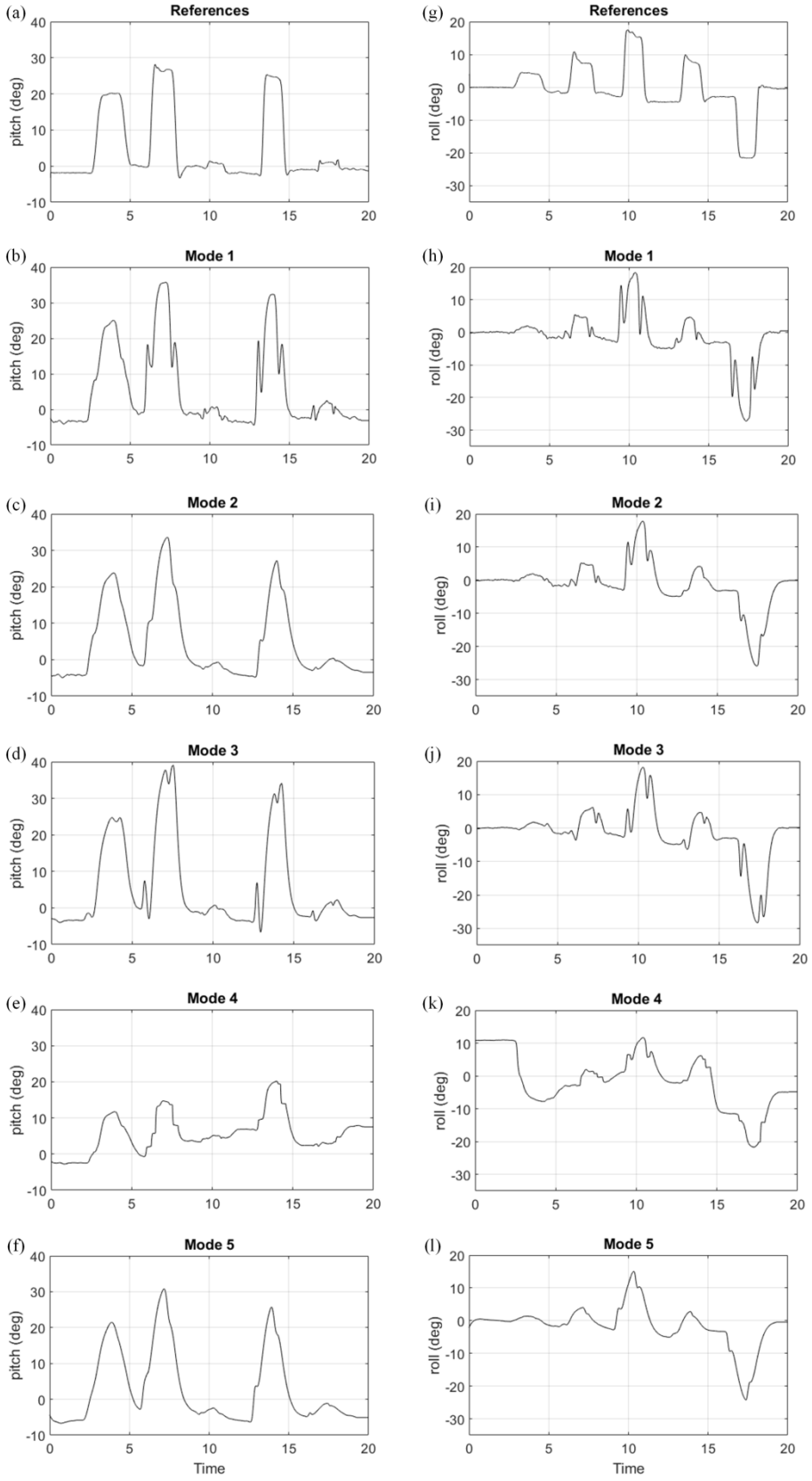

Figure 3.28 Test B attitude estimation result: Five modes in comparison to the references (a and g) for pitch (left column) and roll (right column) [20].

The quantitative evaluation using MSE between each mode at the time the external acceleration occurred, i.e., during *Phase I* to *Phase IV* is shown in Table 3.12.

Table 3.12 Test B: MSE (S) (in [deg^2]) and maximum error (M) (in [deg]) for all modes during major external acceleration periods (in detail).

External	Mode 1		Mode 2		Mode 3		Mode 4		Mode 5	
acceleration	S_θ Pitch	M_θ Pitch	S_θ Pitch	M_θ Pitch	S_θ Pitch	M_θ Pitch	S_θ Pitch	M_θ Pitch	S_θ Pitch	M_θ Pitch
period	[deg^2]	[deg]	[deg^2]	[deg]	[deg^2]	[deg]	[deg^2]	[deg]	[deg^2]	[deg]
Phase I	74.59	18.51	42.03	11.42	51.92	12.47	123.83	19.45	30.46	10.31
Phase II	70.59	21.70	26.69	10.45	33.07	12.39	66.92	13.48	27.98	9.69
	S_ϕ Roll	M_ϕ Roll	S_ϕ Roll	M_ϕ Roll	S_ϕ Roll	M_ϕ Roll	S_ϕ Roll	M_ϕ Roll	S_ϕ Roll	M_ϕ Roll
	[deg^2]	[deg]	[deg^2]	[deg]	[deg^2]	[deg]	[deg^2]	[deg]	[deg^2]	[deg]
Phase III	50.34	17.29	37.85	14.42	15.12	8.57	48.16	10.08	25.46	8.13
Phase IV	47.63	16.95	22.63	9.51	24.35	11.48	42.07	11.78	18.96	9.18

Figures 3.29 (a and b) present the column bar of Table 3.12 for the MSE of pitch and roll, respectively.

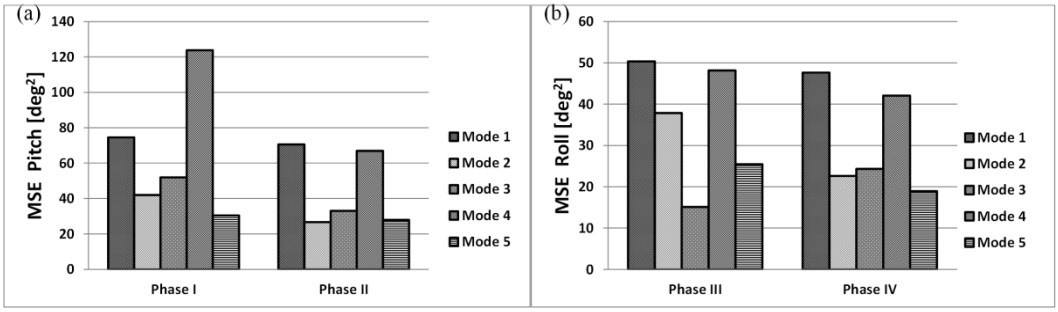

Figure 3.29 Test B: (a) MSE Pitch of five modes, (b) MSE Roll of five modes during external acceleration, all in [deg^2].

In Table 3.13 and Fig. 3.30 we conclude the MSE result of Test B, the average MSE of *Phase I* and *II* as pitch estimation error and the average of *Phase III* and *IV* as roll estimation error.

Table 3.13 Test B: MSE of all modes in [degree^2].

MSE	Mode 1	Mode 2	Mode 3	Mode 4	Mode 5
Pitch [deg^2]	72.59	34.36	42.49	95.37	29.22
Roll [deg^2]	48.98	30.24	19.73	45.11	22.21

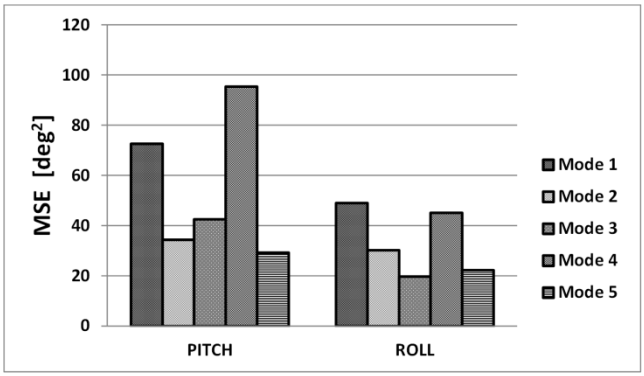

Figure 3.30 Test B: The final MSE Pitch and Roll of each mode during external acceleration in [deg^2].

3.5.5 Experiment Results of Test C

Test C was executed by walking straight forward three strides along the x-axis of the measurement room coordinate frame. Figures 3.31 (a) to (l) show the result of attitude estimation using five modes and the MSE result is presented in Table 3.14.

Some parameters values are used in Test C for each mode. *Mode 1* uses R_{nom} = 1.5, while *Mode 2* uses q_0 = 20, R_{nom} = 1.5, and $\lambda = 3x10^4$. *Mode 3* uses threshold δ = 0.2 [G^2], α_1 = 0.8, α_2 = 0.3, and (r_1 = 0.093, r_2 = 0.034, and r_3 = 1.5). *Mode 4* uses the threshold ε_{th} = 0.8 and σ_a^2 = 60. *Mode 5* works using σ_{a0}^2 = 1.5 and the factor of softened part α_a = 50. The parameter values were determined using the similar values in Test B; however, the value of some parameters has been tuned in order to get the minimum MSE.

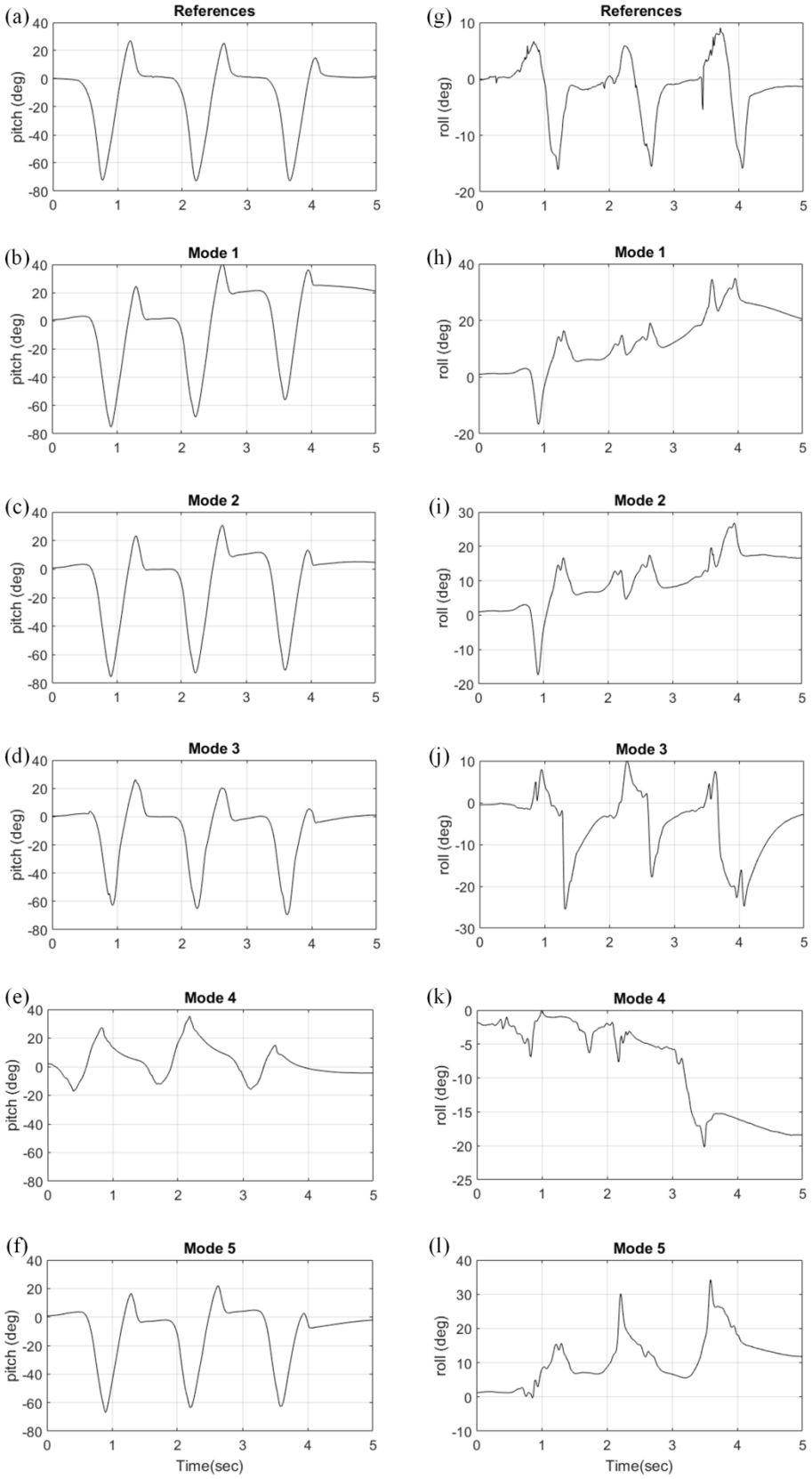

Figure 3.31 Test C attitude estimation result: Five modes in comparison to the motion capture system as references (a) and (g) [20].

Table 3.14 Test C: MSE in [degree^2] of all modes.

MSE	Mode 1	Mode 2	Mode 3	Mode 4	Mode 5
Pitch [deg^2]	395.35	175.97	147.92	1036.2	160.87
Roll [deg^2]	367.57	245.80	55.24	141.35	217.94

3.6 Discussion on Results

3.6.1 Mode 1

External acceleration compensation does not play a role in *Mode 1*. *Mode 1* used R_{nom} in the measurement noise covariance matrix, as in Eq. (3-40), and did not use the external acceleration compensation model. An experiment result of *Mode 1* in Test A was presented in Table 3.8. The comparison in Table 3.10 shows that the MSE of pitch and roll estimation is 25.25 and 3.65 [deg^2], respectively. The attitude estimation accuracy of *Mode 1* is lower than *Mode 2*. This result confirms the findings presented in the literature [10], where the standard EKF has lower accuracy in the one-axis test type.

The result of *Mode 1* in Test B, as shown in Figs. 3.28 (b and h), demonstrate that the effect of external acceleration during *phase I to IV* on the pitch and roll estimation is still dominant. The final result of *Mode 1* in Test B as shown in Table 3.13 and Fig. 3.30 indicates that *Mode 1* estimation accuracy is also lower than *Mode 2, Mode 3,* and *Mode 5*. Kalman filtering employs a compensation mechanism that surpasses *Mode 1*'s accuracy, in except *Mode 4*. *Mode 1* has a MSE of pitch 36% greater than that of *Mode 2*, 26% greater than that of *Mode 3,* and 43% greater than that of *Mode 5.* The result of *Mode 1* in Test C is also in line with the result in Test B, which is that *Mode 1* estimation accuracy is lower than in *Modes 2, 3,* and *5.*

3.6.2 Mode 2

The proposed algorithm in *Mode 2* involved the external acceleration compensation models Eq. (3-44) and covariance matrix updating process Eq. (3-50), which plays an important role in improving the attitude estimation accuracy during fast movement. If *K=1* was imposed for all experiments, then the only setting parameters are q_0 and λ.

The two parameters q_0 and λ are chosen empirically based on the best estimation result. However, there is some consideration when choosing these parameters. As shown

in Eq. (3-44), a smaller q_0 reduces the cutoff frequency. The value of q_0 that determines the cutoff frequency affects the value of the compensating model output, a_k, where the effect continues to the value of the measurement noise covariance matrix (R) in attitude estimation. The impact of the q_0 variability to the square-output of a_k along the x-axis was presented in Fig. 3.25. It appears that the smaller value of q_0 has increasing amplitude of a_k^2, which will simultaneously increase the value of the measurement error covariance matrix. In the meantime, the effect of the λ is as an amplified factor for the softened part (λa_k^2). The increasing value of λ simultaneously increases the value matrix R, which reduces the Kalman gain. Therefore, the contribution of the measurement to the estimation process also decreases; thus, the estimate is less affected by measurement from an accelerometer.

The result of *Mode 2* in Test A is shown in Table 3.10 as a concluding table. As can be seen in the Table 3.10, the *Mode 2* MSE of pitch is 8.57 and 1.48 [deg^2], which is the lowest among all those tested.

For Test A, the variability of q_0 influences the estimation error; however, the attitude reference is always zero degrees, and therefore we cannot observe the effect of the q_0 variability to the attenuation of some important signal by model Eq. (3-44). Therefore, we need a test like Test B and Test C to observe the variability effect of q_0 on the appearance of the signal.

In Test B, quantitative assessment of MSE on pitch and roll is done in *Phases I* to *IV*, as shown in Table 3.13 and Fig. 3.30. *Mode 2* has a MSE value of 34.36 and 30.24 [deg^2] for pitch and roll estimation, respectively. The MSE of pitch is lower than in *Modes 1, 3,* and *4*, and *Mode 5*'s accuracy surpasses the accuracy of *Mode 2*. In roll estimation, the accuracy of *Mode 2* outperformed the accuracy of *Modes* 1 and 4. It was observed that *Mode 2* is able to reduce the effect of external acceleration on the correct timing when it occurs; i.e., during *Phases I*, *II*, *III*, and *IV*. The results of real world application, such as in Test C, are in Table 3.14 and Figs. 3.31; the MSE of *Mode 2* is 175.97 [deg^2] and 245.8 [deg^2] in pitch and roll estimation, respectively. This means that the average estimation error in every point calculation is around 13.3 [deg] and 15.7 [deg]. In Test C, *Mode 2* accuracy outperformed the accuracy of *Mode 1* and *Mode 4* in pitch estimation, and outperformed *Mode 1* in roll estimation. Overall, for Test C, *Mode 3* outperformed the accuracy of other modes both on pitch and roll angle estimation.

3.6.3 Mode 3

In our Test A and Test B experiment, *Mode 3* has lower estimation accuracy in pitch estimation (a bigger MSE) as compared to *Mode 2* and *Mode 5*, as shown in Table 3.10 and Table 3.13. It is important that we do not make the criticism that *Mode 2* is superior to *Mode 3* in Test B, since different settings on the combinations of δ, α_1, and α_2 as in Eq. (3-56) and (3-57) might result in a better performance.

The result in Table 3.14 for Test C indicates that *Mode 3* outperformed all modes. The number of setting parameters in *Mode 3* is more than in other modes (i.e., three setting parameters); which provides a more rigorous setting. However, this also requires more effort than in the other modes. Our proposed algorithm in *Mode 2* has fewer parameter settings; i.e., q_0 and λ. Furthermore, the execution of the compensation algorithm is fully dependent on the existence and magnitude of the square of external acceleration model, as in Eqs. (3-44) and (3-50), rather than threshold-based, as in Eq. (3-56). However, we observed that the measurement model in *Mode 3* (as in Eq. (3-53)) has an advantage over *Mode 2*. This model incorporates the data from gyro as well as accelerometer data. Therefore, the setting mechanism of matrix R consists of two parts: accelerometer and gyro. When the level of trust in the accelerometer lowers then it is possible to set the level of trust higher in gyro.

3.6.4 Mode 4

Of all the tests, the estimation accuracy of *Mode 4* is the lowest. We suspect that this is caused by the presence of magnetometer measurement vectors in the measurement model of *Mode 4*. The earth's magnetic vector, ${}^{b}\mathbf{m}$, has a magnitude that is always changing over a large range of time [29]. Furthermore, the experiment room we used is not guaranteed to be free of magnetic interference and soft iron distortion. In [29] it is suggested that to overcome this problem, initialization must be done carefully to find out the exact magnitude and orientation of the magnetic field. This vector can be used during the experiment.

3.6.5 Mode 5

In our experiments, the accuracy of *Mode 5* outperformed *Mode 2* in Test B around 8.1% and 15.3% for pitch and roll, respectively (as shown in Table 3.13). This also occurs in Test C. As shown in Table 3.14, the estimation accuracy of *Mode* 5 is 4.5%

and 6% over *Mode 2'*s in pitch and roll estimation, respectively. However, in Test A, *Mode* 2 outperforms *Mode 5* in all λ and q_0 combinations.

The difference between *Mode 2* and *Mode 5* is in the softened part of the measurement error covariance matrix. *Mode 5* in Eq. (3-59) uses the absolute difference between measurement and predicted acceleration. However, in *Mode 2* we use the model of external acceleration as the softened part.

3.7 Limitation, Future Direction, and Affordable Error

In all tests the proposed *Mode 2* outperformed *Mode 1*. From these results we were able to ensure that a mechanism of external acceleration compensation has the influence to improve estimation accuracy. Even though there is an advantage to improving the estimation accuracy, some of the major limitations to the experiments will be described.

First is the limitation of measurement model. *Modes 1, 2,* and *3* used Euler representation. The model in *Mode 1* and *Mode 2* in Eq. (3-30) did not include the measurement from a gyroscope. With a slow motion sensor this measurement model might be not a problem, because it is not necessary to compensate the external acceleration. The setting of the measurement noise covariance matrix (R) in Eq. (3-50) primarily relies on the roll and pitch from accelerometer data. When the value of R becomes larger due to the presence of external acceleration, the estimation process in Kalman filtering is less affected by accelerometer, but at the same time we cannot increase the level of trust in the gyroscope. Furthermore, it is important to consider modification of the measurement model in the future work.

The second limitation is that the proposed external acceleration compensation in Eq. (3-44) did not include automatic calculation of parameter q_0. The model in Eq. (3-44) is used as an additional part for the measurement noise covariance in Eq. (3-50). This model relies on the frequency of the application that the model will use. Before using the model, the determination of the q_0 value is important. One prospective improvement of this model is the additional step of calculating the optimum value of q_0 from IMU data before the Kalman filtering process.

The third limitation is considering the application of *Mode 2* whenever the pitch angle (θ) reached the $\pi/2$ [rad], even though there is an advantage of Euler representation over the quaternion representation. The limitation of Euler representation in this experiment is that whenever pitch angle (θ) reaches $\pi/2$ [rad] the state in *Mode*

2 will be singular. This limitation need not be considered as long as the application is still able to accept the range of angle.

The fourth limitation is related to the linearization process in the process model of *Mode 2*, which leads to first order approximation error. *Mode 2* uses EKF based filtering that employs linearizing the nonlinear model. The first order linearization might be the cause of degraded accuracy in all modes that employed EKF; i.e., *Mode 1, Mode 2, Mode 3*, and *Mode 4*. However, *Mode 5* employs an unscented Kalman filter (UKF) that is free from linearizing through Jacobian. As a result, *Mode 5* outperformed almost all modes in Test B and outperformed *Mode 2* in Test C. One consideration to avoid the first order approximation error besides using UKF is using a direction cosine matrix (DCM) method [29].

The explanation about affordable error in our study is as follows. The reported MSE in Table 3.10 (one-direction test), Table 3.13 (multi directional test), and Table 3.14 (walking test) indicated that the MSE result of the proposed method is large but smaller than the standard EKF. The proposed method could work to improve the accuracy of attitude estimation in reducing the effect of external acceleration; therefore, the error is acceptable. However, improvement of accuracy is necessary in the future study by considering the modification of measurement model and the additional step of calculating the optimum model parameter.

3.8 Summary

In this chapter, the main contribution is the algorithm for external acceleration compensation, which aims to improve the attitude estimation accuracy. A Kalman filter-based attitude estimation using a compensating algorithm has been discussed. The experiment was performed using three types of tests: movement on one axis, multi directional movement, and walking. The employment of five different approaches to deal with the dynamic test and the proposed method is placed on *Mode 2*. The first approach is the standard KF model, without using external acceleration compensation (*Mode 1*). The second approach is the modified KF model, using the proposed compensating procedure (*Mode 2*); the third is a *weighted-switching* method (*Mode 3*); the fourth is a quaternion-based EKF using a *threshold-based* method (*Mode 4*); and the fifth (*Mode 5*) using an unscented Kalman filter and is *threshold-based combined with a softened part*.

The experiment results showed that by using the external acceleration compensation process, the estimation accuracy of the proposed algorithm is improved

when compared with the standard EKF procedure in *Mode 1* in all tests. *Mode 2* also outperformed all modes in Test A by using the optimal parameter setting. In dynamic Test B, *Mode 5* outperformed other modes; we suspect that this is caused by using UKF in *Mode 5*. The UKF was free from first order approximation of a nonlinear system. The advantage of *Mode 3* over other modes is presented in Test C. *Mode 3* used a measurement model that included accelerometer and gyroscope data, while the measurement model in *Mode 2* was related to accelerometer data.

There is a lack of efficiency comparison to some modes in the experiments. Compared to the other modes, the advantage of *Mode 2* over *Mode 3* is the number of parameters set; *Mode 2* has fewer parameters. *Mode 3* takes a two-step EKF, which leads to additional computational overhead. The advantage of *Mode 2* over *Mode 4* and *Mode 5* is the parameterized spatial rotation; quaternion as used in *Mode 4* and *Mode 5* is hardly used because it is a burden to update its four variables [29]. However, Euler needs to update two variables. Specifically, in comparing *Mode 2* and *Mode 5*, the computational time of the extended Kalman filter is much lower than in the unscented Kalman filter [38].

Nevertheless, as a future problem to be solved, in order to increase the estimation accuracy potential for other applications, it needs the addition of a step that can perform adaptive parameter settings (q_0 and λ) based on the present input from the IMU. Using UKF and DCM is also one consideration to improve accuracy in order to be free from linearization approximation error.

This page intentionally left blank

4. Ultrasonic Sensors Position and Step-Length Prediction using Artificial Neural Network in a Shoe-Type Gait Measurement Device

4.1 Introduction

The goals of this session were as follows: (1) to develop a method to determine the number, position, and angle of ultrasonic sensors under simulation for a shoe-type measurement device; (2) to implement the simulation results on an actual shoe-type measurement device and evaluate the measurement scope based on the results of previous simulations; and (3) to establish a method of processing the distance data from ultrasonic receivers to predict the step-length of human steps using an artificial neural network (ANN). The step-length is the distance between corresponding successive points of heel contact of the opposing feet.

Recently, an increasing amount of research has been driven by interests in gait-assessment systems [28, 39]. Some researchers use an inertial measurement unit (IMU) to measure stride length, an important spatial gait parameter, by processing temporal data [39]. Our previous shoe-type measurement device is for measuring gait performance such as step-length, step width, pressure distribution [40, 41], and attitude estimation during the swing phase using IMU [20]. As shown in Fig. 4.1, the previously designed shoe contains ultrasonic receivers and transmitters, pressure sensors, and IMU; it uses seven ultrasonic transmitters and twelve receivers. The sensors are perishable and fragile, so the measurement of gait parameters is prone to error. In order to streamline the sensors and reduce their number, the simulation technique was designed [21]. In the previous iteration, step-length was measured by integrating the ultrasonic sensors and gyro data using a particle filter algorithm.

In order to improve the step-length prediction accuracy, in this section we introduce the simulation method, the results of which are consist with the number of ultrasonic sensors, the optimal sensor angle, and the sensor's position. Thereafter, we discuss the actual implementation of the new shoe-type measurement device, including the scope of the measurement's test. Finally, we discuss the implementation of multi-layer perceptron (MLP) for step-length prediction using data from ultrasonic sensors.

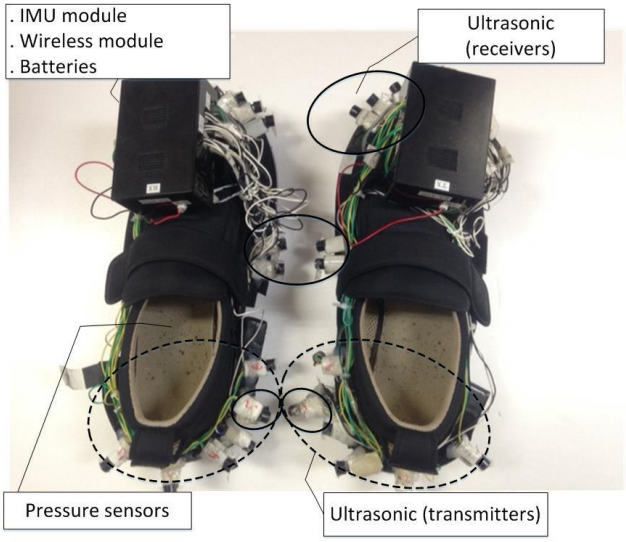

Figure 4.1 The shoe-type measurement device.

Table 4.1 Specification of Murata ultrasonic sensor

Part Number		**MA40S4R/S**
Construction		Open structure type
Using method		Receiver and Transmitter (dual use) type
Nominal frequency	[kHz]	40
Sound Pressure	[dB]	120±3 (20 [Pa])
Directivity	[deg]	80
Detectable range	[m]	0.2 – 4
Dimension	[mm]	9.9 ϕ x 7.1 height
Input voltage	[V] p-p	20 (40 [kHz]) continuous signal

4.2 Simulation Method

The acoustic wave that was produced by the ultrasonic sensor transmitter and the data from all receivers were simulated using a third-party MATLAB® toolbox called *k-Wave*. We took advantage of one particular feature of *k-Wave*, i.e., forward ultrasound wave simulation for homogeneous media in 2D. This simulation assumes a lossless and homogeneous fluid medium based on a pressure-density relationship and first-order partial differential equation in momentum conservation and mass conservation [42, 43]. There are four input structures used in the *k-Wave*: *kgrid, medium, source,* and *sensor*. The parameter settings of these structures will be used to simulate the MA40S4R/S ultrasonic sensor by Murata Co., Ltd., Japan. The MA40S4R is a receiver and the

MA40S4S is a transmitter. Table 4.1 lists several of the important specifications related to this simulation [44].

4.2.1 Defining the Grid Points (*kgrid*)

This determines how the continuous medium is divided into an evenly distributed mesh of grid points [43], with 1 x 1 [mm] representing one grid point. We determined 350 x 1000 grid points for simulation, which contains six regions of 165 x 295 grids as shown in Fig. 4.2. Regions I, III, and V, shown in Fig. 4.2 are used for the left foot and regions II, IV, and VI represent the right foot.

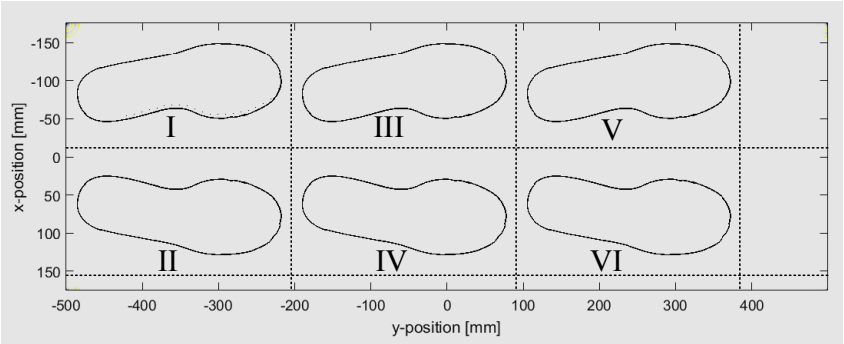

Figure 4.2 The grid point and region division [22]

Figure 4.3 shows several gait parameters, such as foot progression angle, step width, and step-length. The foot progression angle is the angle of the intersection between the foot axis and the line progression. This angle remains relatively stable at 8 to 12 [deg] of out-toeing throughout growth [45], as shown in Fig. 4.3(a). As this study is associated with the normal human gait, we use a constant 10 [deg] foot progression angle.

Figure 4.3(b) shows the step width (walking base) used in the simulation. This parameter represents the mediolateral distance between the heels in double support, although this may become evident only at faster paces. Normal step width varies with age and is commonly less than the pelvic width, i.e., 5 to 13 [cm] [45-47]. The other parameter shown in Fig. 4.3(c) is stride length, which is the distance between two successive placements of the same foot. The mean stride length during normal walking in adults ranges from 0.7 [m] [45, 48] to 1.3 [m] [28].

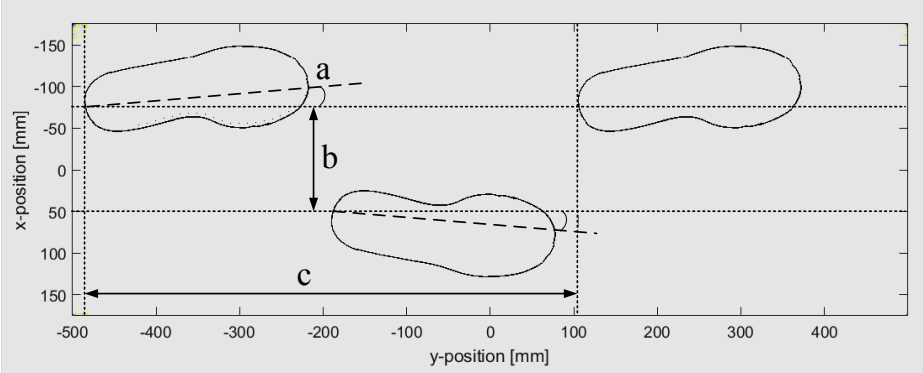

Figure 4.3 The representation of (a) foot progression angle, (b) step width, and (c) stride length [22].

4.2.2 Defining the Acoustic Medium

This input structure defines the material properties at each grid point. The structures include the determination of sound speed, ambient mass density, the nonlinearity parameter, power law absorption coefficient, and power law absorption exponent. We assumed the simulation is linear and lossless, so that the sound speed is the only structure that needs to be determined. Assuming a room temperature (T) of 25 [deg] Celsius, we determined the sound speed c = 346 [m/s] using Eq. (4-1) [49].

$$c = 331.4 + 0.607 \, x \, T \tag{4-1}$$

4.2.3 Defining the Acoustic Source

The source structure (transmitter) defines the properties and location of any acoustic source in the medium. There are three different types of source options, i.e., 1) an initial pressure distribution, 2) a time-varying pressure source, and 3) a time-varying particle velocity source. The first type is the most appropriate for simulating pulsed acoustic and thus does not correspond to our needs since we expect a continuous input signal according to the specifications in Table 4.1. The second type, the time-varying pressure source, aligns with the needs of this simulation. The third type uses a varying velocity of force, so it does not comply with our simulation because the pressure source that we used has a constant speed.

Using a time-varying pressure source, the design of the MA40S4S Murata ultrasonic transmitter is as follows. The two key field names were *source.p_mask* and *source.p*, which contain a binary matrix of the transmitter position and time-varying pressure signal at each position given by *p_mask*, respectively. To meet the frequency and sound pressure specifications detailed in Table 4.1, the value of *source.p* was

determined using a sinusoidal input with the frequency of 40000 [Hz] and magnitude of 20 [Pa] (equal to 120 [dB]).

To meet the directivity in sound pressure level of 80 [deg], as shown in Table 4.1, the shape and size of the transmitter needed to be determined on the *source.p_mask*. Since the desired acoustic pressure should spread within the directivity of 80 [deg] according to the specification, the form of source grid that this suite needs is a *line*. The next step involves how to determine the length of the source grid. In the simulation, this cannot be longer than the diameter of MA40S4S, which is approximately 10 [mm]. The length of the source grid was determined based on the method that follows, as shown in Fig. 4.4. A 120 independent grid Rx was laid serially in front of the Tx and the distance between Tx and Rx was simulated at 30 [cm] and 50 [cm] to refer to actual conditions, which is half the stride length of a normal adult (Fig. 4.4c). By using the trigonometric tangent function, the value of β will be 127 [deg] and 100 [deg] when the distance between Tx and Rx is 30 [cm] and 50 [cm], respectively. The simulation was executed with different lengths for the Tx grid and showed that a length of 10 grids (10 [mm]) satisfied the directivity specification of 80 [deg]. This model aligns with the physical size of MA40S4S. The result of this simulation will be presented in subsection 4.3.2.

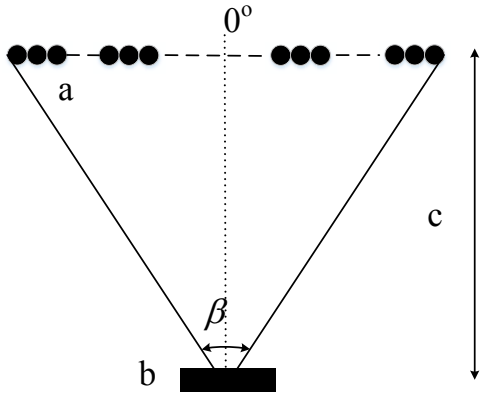

Figure 4.4 Source length and directivity determination. (a) 120 independent grid sensor (Rx); (b) ten grids source (Tx); (c) the distance between Tx and Rx; (β) angle.

4.2.4 Defining the Sensor

This structure defines the properties and location of the sensor points used to record the acoustic field at each simulation time-step [43]. Using the field name *sensor.mask,* we defined a binary grid as one sensor (Rx). In every simulation time-step, the acoustic pressure (*p*) was recorded using the *sensor.record* field name; one of the recorded results is shown in Fig. 4.5. The other important field name is *sensor.directivity_angle* and is

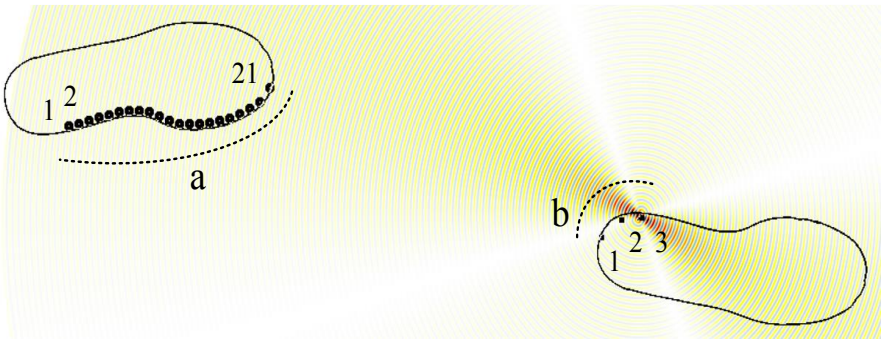

Figure 4.5 (a) The range of possible ultrasonic receiver positions; (b) ultrasonic transmitter positions. This capturing figure was taken when Tx_3 works and the right shoe is on the region VI.

useful for finding the greatest sensitivity for each sensor.

The sensor simulation method is based on the purpose of determining the sensor directivity angles, the number of sensors, and their positions on the shoe-type measurement device in the range of the human step.

In order to find the sensor angle, the simulation method is as follows. At the beginning of the simulation, three ultrasonic transmitters (MA40S4S) will be placed on the medial heel of the right foot with a 60 [deg] azimuth angle of the sensor grid lines. The default position and azimuth angle of the transmitters were determined by considering the previous study [40]. The transmitter position can reach the coverage of human walk by means of when one foot is in front of the opposite foot. As shown in Fig. 4.5, 21 ultrasonic receivers (MA40S4R) were installed along the medial heel next to the 2nd toe of the left foot. To find the greatest sensitivity for each sensor in the range of the human step, the sensor was rotated from -90 [deg] to 90 [deg] in 10 [deg] increments. One angle that has the greatest sensitivity is chosen as the best angle; therefore, 21 best angles were found from 21 sensors.

In order to find the number of sensors, the simulation method is as follows. From the 21 sensors that have the best angles, the sensors with the same angles will be eliminated by taking only one of them. The results of this work will be discussed in the subsection 4.3.3.

4.3 Simulation Results

4.3.1 Acoustic Pressure Signal

The series of sensors shown in Fig. 4.5 received the acoustic wave from each source (Tx_1, Tx_2, and Tx_3) after the time-of-flight had elapsed. We evaluated the sensitivity of each sensor using the maxima of the acoustic pressure in each degree of

sensor directivity.

Figure 4.6 is one example of acoustic pressure received in the 1st sensor (directivity angle: 60 [deg]) and the 21st sensor (directivity angle: 60 [deg]); the source is from Tx_3 when the right shoe is on region VI. As shown in Fig. 4.6, the acoustic pulse arrived at a different time on each sensor. The time-of-flight for the 1st sensor is longer than the time-of-flight for the 21st sensor. This is in line with the positions of those sensors from Tx_3, whereby the position of the 1st sensor is farther than the position of the 21st from Tx_3. The maxima of the acoustic pulse were counted after this time-of-flight elapsed, i.e., after the 983rd and 487th time-step on the 1st and 21st sensors, respectively.

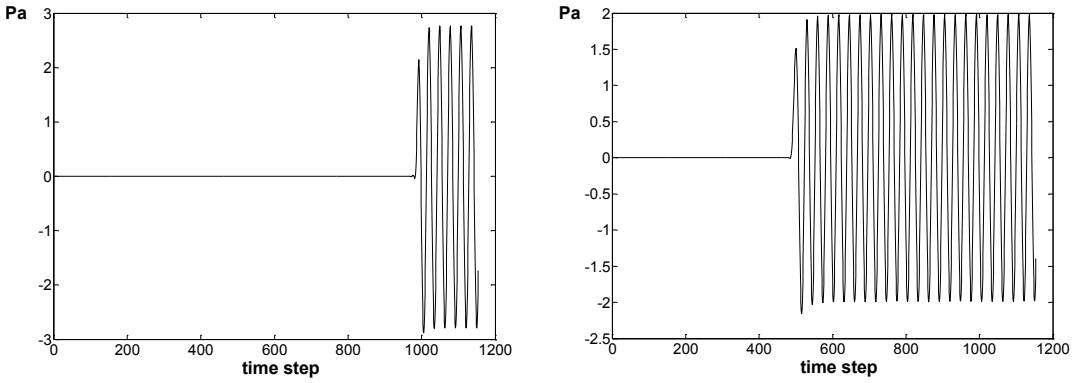

(a) (b)

Figure 4.6 The acoustic pressure on the sensors; (a) on the 1st sensor, the acoustic pressure arrived after the 983rd time-step; (b) on the 21st sensor, the acoustic pressure arrived after the 487th time-step. The acoustic source is from Tx_3, region VI.

Figure 4.7 shows the algorithm proposed to determine the maxima of the acoustic pulse that does not depend on the time-of-flight and the signal's spike.

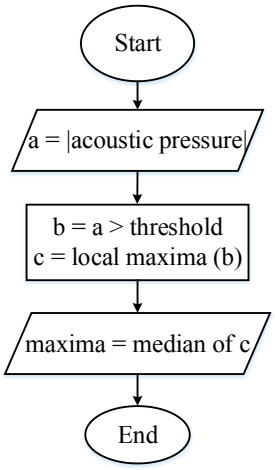

Figure 4.7 The maxima of the acoustic pulse calculation algorithm

4.3.2 Source (Transmitter) Directivity

This section will explore the simulation results of source grid length, as noted in section 4.2.3. Figure 4.8 shows the directivity map of 10 grids of the source grid; it is equivalent to 10 [mm] and equivalent to the diameter of the ultrasonic transmitter MA40S4S. The figure obtained by the maxima of time series acoustic pressure recorded at the sensors' points, located in the range of β = 100 [deg]. The distances between the 10 grids of sources and the sensors is 50 [cm]. Figure 4.9 represents the same plot as in Fig. 4.8 but for β = 127 [deg] and the distance between sources and sensors is 30 [cm].

As shown in Fig. 4.8 and Fig. 4.9, the results can cover an 80 [deg] directivity angle, which is in accordance with the specifications in Table 4.1.

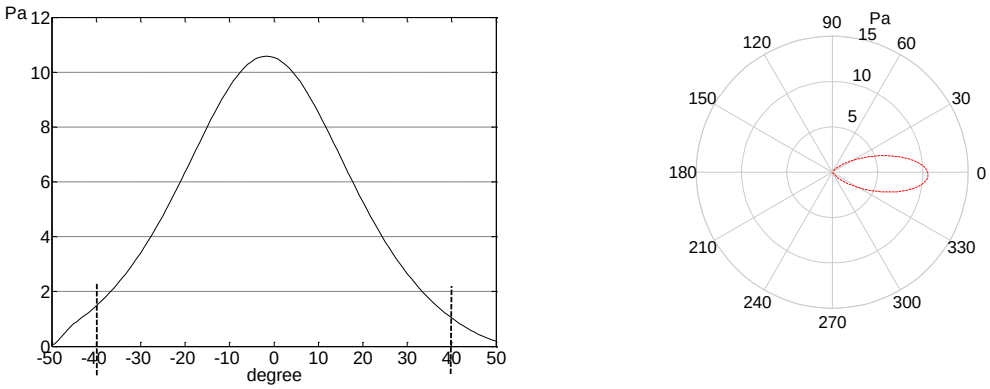

(a) (b)

Figure 4.8 The pressure level on each sensor when the distance between Tx and Rx is 50 [cm], based on the design in Fig. 4.4: (a) plotted on Cartesian; (b) plotted on polar plot.

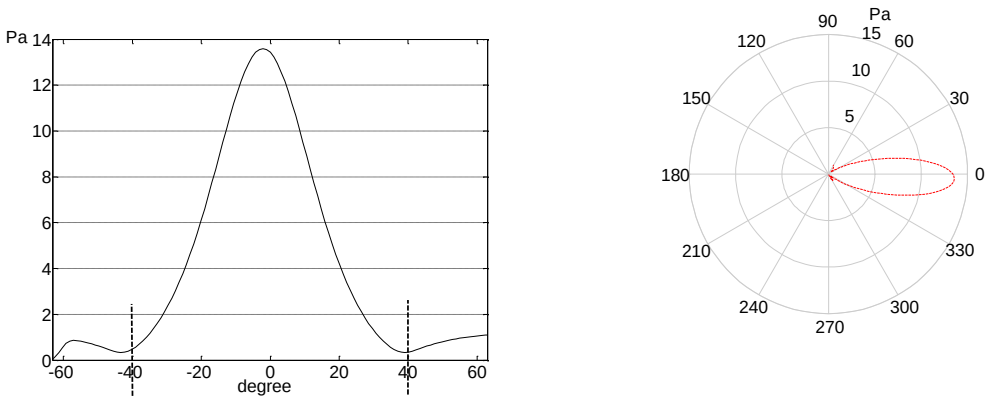

(a) (b)

Figure 4.9 The pressure level on each sensor when the distance between Tx and Rx is 30 [cm], based on the design in Fig. 4.4: (a) plotted on Cartesian; (b) plotted on polar plot.

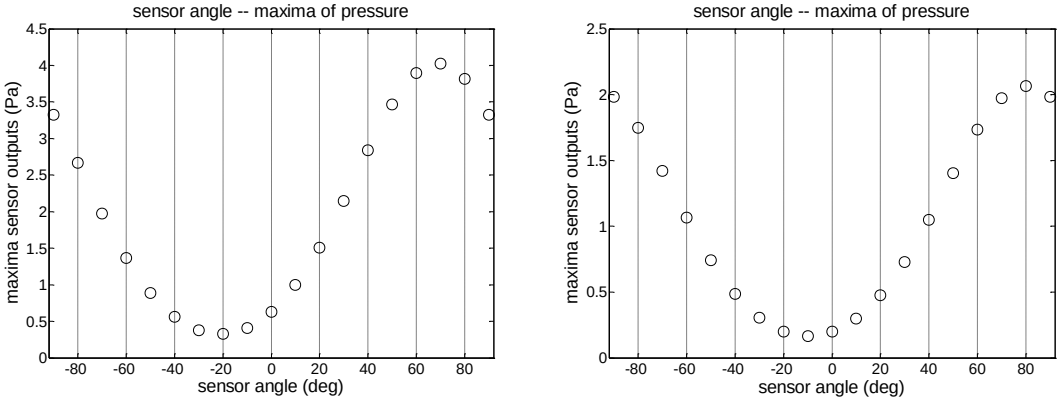

Figure 4.10 The maxima of acoustic pressure level on each directivity angle of sensor. These graphs represent the 3rd sensor and use the acoustic source from transmitter Tx_2. (a) When the right shoe is placed on the region IV, the best directivity angle is 70 [deg]. (b) When the right shoe is placed on region VI, the best directivity angle is 80 [deg].

4.3.3 Optimal Sensor Directivity Angle and the Number of Sensor Determinations

This section concerns about finding the optimal sensor (receiver) angle and reducing the receiver number. As we have sensor rotation, i.e., -90 to 90 [deg] in 10 [deg] increments, there will be 19 sensitivities available for each sensor.

Figure 4.10 shows one plot example of the maxima of acoustic pressure related to the receiver angle. It can be seen that the best angle shifts from 70 to 80 [deg], when the right shoe is moved from region IV to region VI. The directivity diagram is shown in detail in Fig. 4.11. A directivity angle of 0 [deg] corresponds to maximum sensitivity to waves traveling in the x (up/down) direction. A directivity of 90 (or -90) [deg] corresponds to maximum sensitivity in the y (left/right) direction [43].

Table 4.2 shows the complete data for the best receiver angle taken from the simulation at two positions of the right shoe, i.e., regions IV and VI. The last row represents the rounded average value that represents the optimal or acceptable degree for each sensor on the scope of region IV to region VI.

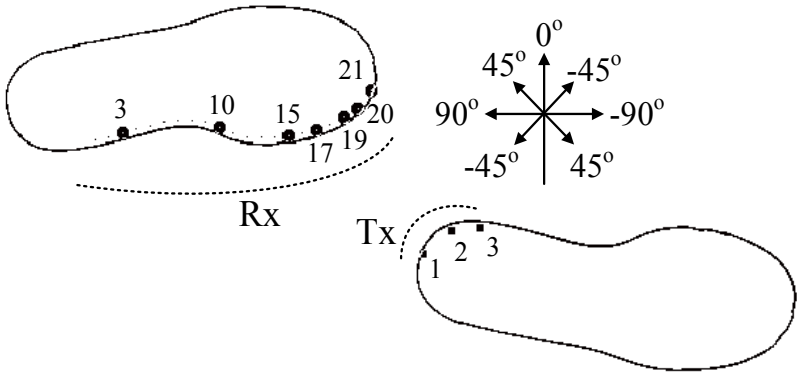

Figure 4.11 The final position of seven sensors based on the selection method shown in Table 4.2. The arrow direction shows the sensor directivity angle [22].

Table 4.2 The range of sensor directivity angles (in detail).

Directivity	**Sensor number**																				
[deg]	**1**	**2**	**3**	**4**	**5**	**6**	**7**	**8**	**9**	**10**	**11**	**12**	**13**	**14**	**15**	**16**	**17**	**18**	**19**	**20**	**21**
Tx_1[a]	70	70	60	60	60	60	60	50	50	50	50	50	50	40	40	40	30	30	20	20	20
Tx_1[b]	80	80	80	80	80	80	80	80	80	80	80	80	80	80	70	70	70	70	70	70	70
Tx_2[a]	70	70	70	70	70	60	60	60	60	60	60	60	60	50	50	50	40	40	40	30	20
Tx_2[b]	80	80	80	80	80	80	80	80	80	80	80	80	80	80	80	80	80	80	70	70	70
Tx_3[a]	70	70	70	70	70	70	70	60	60	60	60	60	60	60	60	50	50	50	40	40	30
Tx_3[b]	80	80	80	80	80	80	80	80	80	80	80	80	80	80	80	80	80	80	80	70	70
optimal	75	75	75	75	75	70	70	70	70	70	70	70	70	65	65	60	60	60	55	50	45

[a] When the right shoe is placed on the region IV
[b] When the right shoe is placed on the region VI

Finally, we can estimate the number of sensors that will be used in the implementation by reducing the number of sensors in this simulation. The reducing technique is based on the similarity of the optimal directivity angle on the last row of Table 4.2. As an example, the 1st through 5th sensors have the same optimal directivity angle, i.e., 75 [deg]; in this case, only the 3rd sensor will be retained. Seven sensors will be used as a result of this simulation: the 3rd, 10th, 15th, 17th, 19th, 20th, and 21st. The angles of those sensors are 75, 70, 65, 60, 55, 50, and 45 [deg], respectively (the shading cells in the last row of Table 4.2). The final positions of these sensors are shown in Fig. 4.11.

4.4 Implementation on the Actual Shoes

The simulation results from the previous section, i.e., Table 4.2 and Fig. 4.11, are implemented on the actual shoe-type measurement device. The implementation is shown in Fig. 4.13.

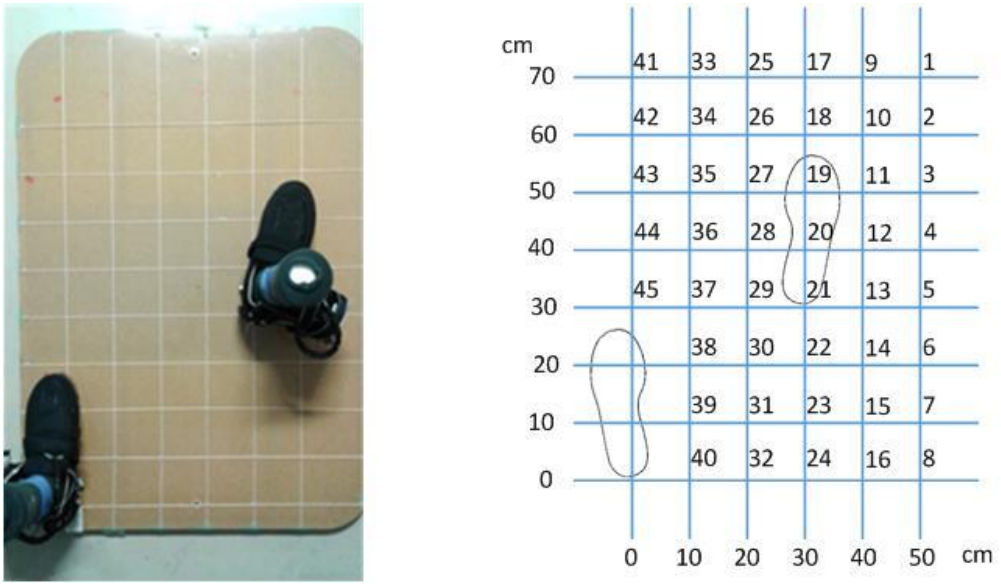

(a) (b)

Figure 4.12 Test setup and grid division for data retrieval. (a) the board as a testbed; (b) grid division and grid number 1 to 45 [22].

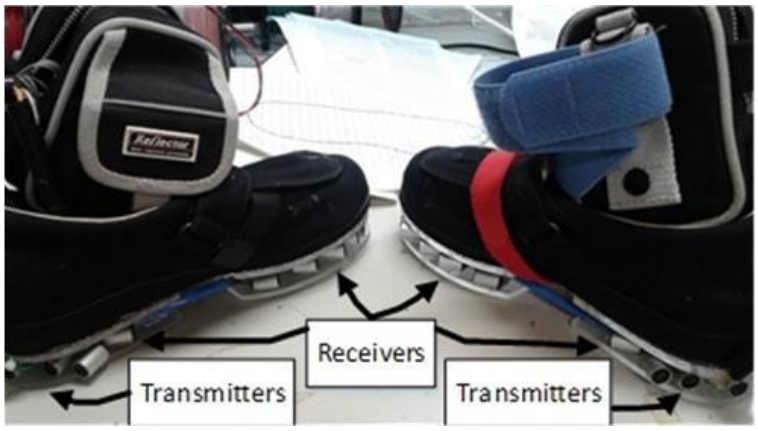

Figure 4.13 The implementation of the position and angle of ultrasonic sensors based on the simulation [22].

4.4.1 Test Setup and Experimental Design

To verify and validate the results of the simulation, the test was conducted using ultrasonic transmitters (MA40S4S) and ultrasonic receivers (MA40S4R). We used a plan board and made a 50x70 [cm] grid system, which is the grid size 10x10 [cm] as illustrated in Fig. 4.12.

The width of the board is determined based on the distance between two heels for an average person, that is, 5 to 13 [cm]. We implemented it using a 50 [cm] width of a plan board in order to test the measurement scope of the sensors. The length of the board is determined based on the average length of the adult human step, i.e., half of the stride length, and followed the simulation region. The mean stride length during normal walking in adults ranges from 0.7 [m] to 1.3 [m].

The C# acquisition data were used to collect the distances between ultrasonic transmitters and receivers. The data retrieval was conducted when the left shoe was on the grid (0,0) [cm] and the right shoe was moved sequentially from the 1st grid to the 45th grid. Assuming that all ultrasonic Tx and Rx are identical between the left and right shoes, we retrieved all data from one side of the human step, in this case, the right step. At every point grid, we retrieved the distance between each receiver and transmitter pair from 25 combinations of foot progression angles. The test of the measurement scope

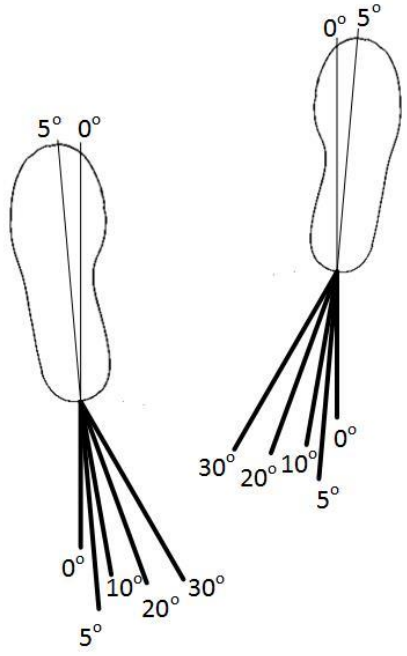

Figure 4.14 The combination of left and right foot progression angle during data retrieval. The capturing figure illustrates the 5 [deg] progression angle [22].

used the foot progression angle up to 30 [deg] which consists of five steps: 0, 5, 10, 20, and 30 [deg]. The 25 combinations came from these five steps of foot progression angles for each shoe. We used a protractor to determine the foot progression angle as shown in Fig. 4.14.

4.4.2 Measurement of Scope Result

Figure 4.15 shows the conclusion of the measurement scope. The test of measurement scope at every grid point using 25 shoe angle combinations resulted in almost all grid points with a measurement scope of 100%. This means that in all 25 shoe angle combinations, the distance data between all Tx and Rx pairs are available. However, in grid numbers 7, 8, 15, 16, 24, 32, and 40, we found that data are not available for all shoe angle combinations. In the 8th and 24th grids, the scope of measurement is 48%, whereas on the 16th grid, the scope of measurement is 56%. In the same way, we found that on the 7th grid the measurement scope is 68%, whereas on the 15th, 32nd, and 40th grids, the measurement scope is between 70% and 80%. The remaining grid points show 100% of measurement scope.

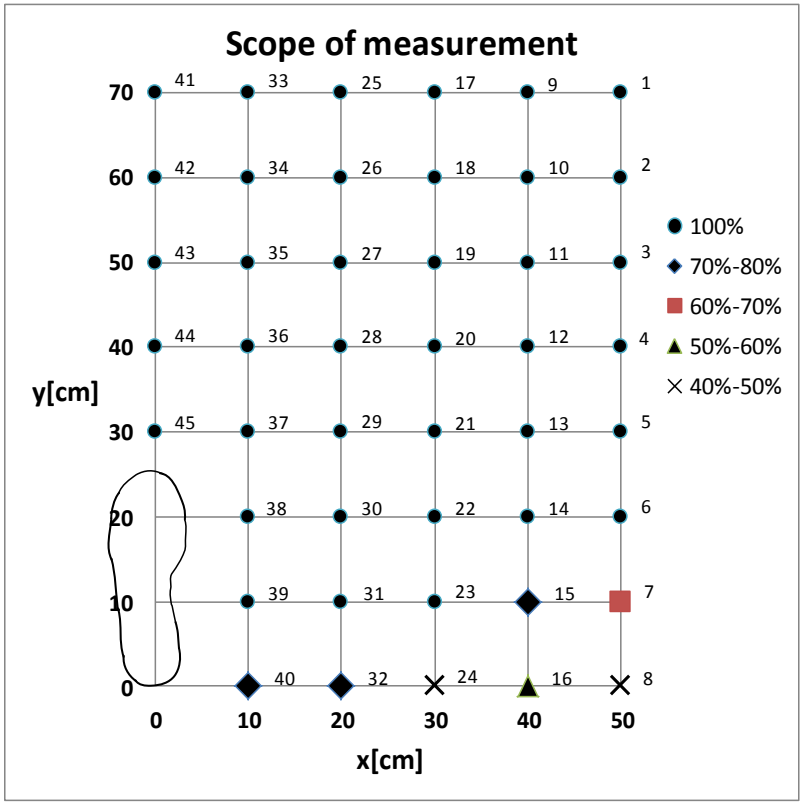

Figure 4.15 Final result of the measurement scope of ultrasound Tx-Rx pairs [22].

4.5 Step-Length Prediction

The step-length is one of the temporal gait parameters measured during the double support phase. We measured the step-length between the two heels of the left and right foot. In a pathological gait, it is possible that the two-step length is different; therefore, the step-length is one of the important gait parameters for clinical gait analysis.

The ultrasonic waves commonly display nonlinear propagation behavior due to the influence of angle direction and the relatively high amplitude to wavelength ratio. The measurement of distances between each pair of receivers and transmitters in our implementation in the previous section shows the tendency of unsteady value. In this case, a heuristic technique that can learn from the situation and provide results through intelligent guesswork is needed. We hypothesized that ANN (artificial neural network) has the ability to learn through training and provide results by generalizing broad categories from specific examples.

4.5.1 Data Preparation during the Development of ANN

At each grid point, we performed 25 combinations of the foot progression angle; for each combination angle, we retrieved 300 points of data. Therefore, we have 7500 points of data for each grid point for one pair of Tx-Rx. Therefore, having 21 pairs of Tx-Rx, we have a total of 21x7500 of measurement data points for each grid point. In the beginning, the total grid point was 45, as shown in Fig. 4.13 (b); therefore, we have 21*x*337500 data points. By observing the data, we found that some grids, as described in the previous section, are out of the measurement scope; therefore, we assume some of those data to be noise for the learning process in ANN. Although the learning process in the network can handle noise in the training data, too many erroneous training values may prevent the ANN from learning the desired model [50]. The filtered data now become 21*x*330600 from 21*x*337500 previously. The data will be divided randomly into three parts of samples within its proportion as follows: training (70%), validation (15%), and testing (15%). The 21 pairs of measurements between ultrasonic Tx and Rx were used as input to the ANN for training, validation, and testing.

The ANN output is based on its architecture type. The type A network output comes from the Euclidean distance between the positions of the left shoe's heel and the right shoe's heel. For example, the distance between coordinate (0,0) to the 27^{th} grid point, for which the coordinate is (20,50), is 53.85 [cm] (refer to Fig. 4.13 (b) for the grid numbers). On the other side, the output of the type B network is designed to be a multiplier coefficient for the actual step-length output, to be described in detail in the next subsection.

4.5.2 Network Architecture and Training Algorithm

We focus on a multilayer network rather than a single layer or recurrent network. The network is a two-layer neural network, the purpose of which is two-stage regression [51]. For regression, typically the number of nodes in the output layer is one [51]; however, in common the multiple nodes in the output layer can handle multiple quantitative responses. In accordance with these statements, two different suggestions for networks will be considered, as follows: a two-layer network with 1 node in the output layer (network A), and a two-layer network with 45 nodes in the output layer (network B). The parameters of the type A network are: (1) 21 input nodes, (2) 20 neurons in the hidden layer, (3) 1 output node, (4) the required training error (MSE) = 0.1, (5) 1000 training epochs, and (6) the maximum failures of validation check = 6. The total of learnable parameters (weights and biases) is 461 parameters. The one output node represents the Euclidean distance in linear representation. The stopping criteria were the training error, the number of epochs, or the maximum validation failures. We found that by using 20 neurons in the hidden layer, the number of training epochs was exceeded, and the validation checks never exceeded the maximum limit. When a small number of neurons were used, we noticed that the maximum failure of the validation checks occurred before 1000 epochs elapsed. Figure 4.16 represents the type A network.

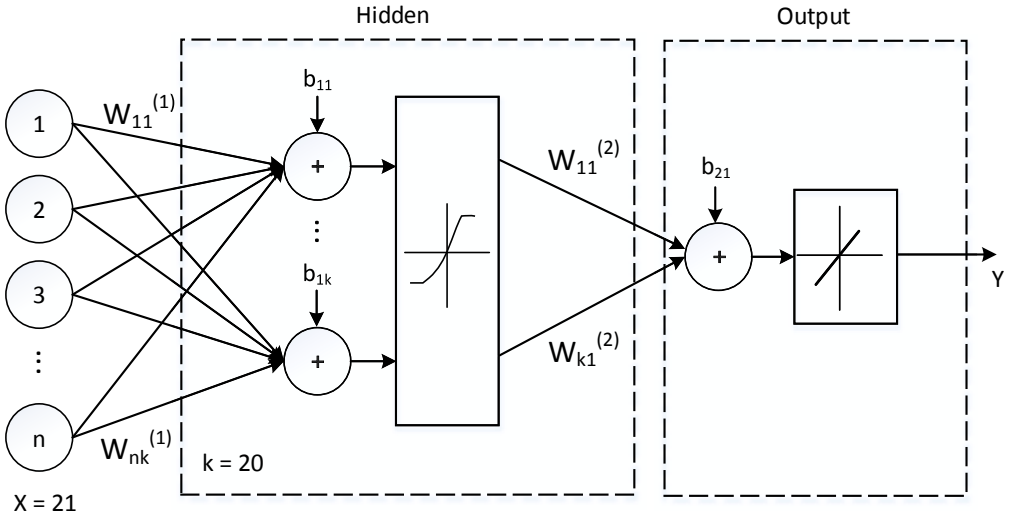

Figure 4.16 Network type A: two-layer neural network with hyperbolic tangent sigmoid and linear transfer function: X input corresponds to the number of data pair between ultrasonic Tx-Rx, W-weights from input layer to hidden layer and from hidden layer to output layer, b-biases of the neurons in hidden and output layer [22].

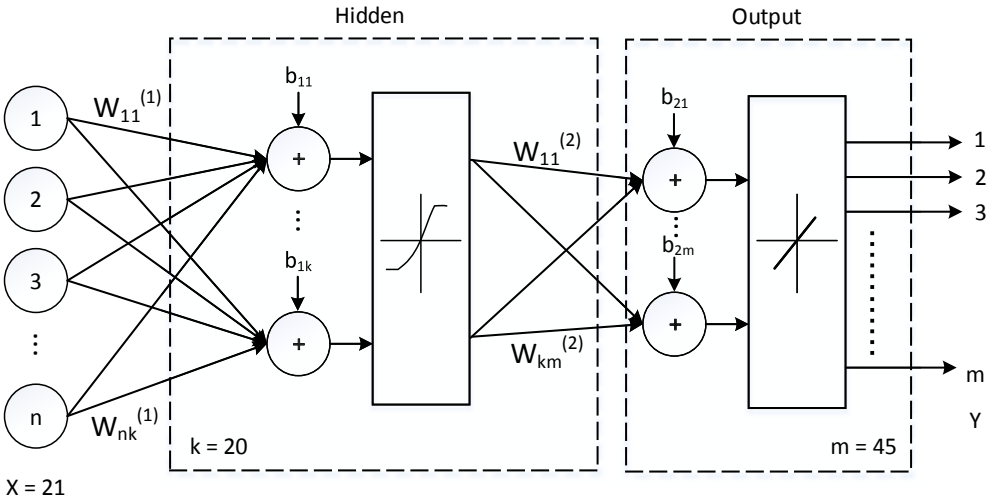

Figure 4.17 Network type B: two-layer neural network with 45 output nodes [22]

Regarding network B, the parameters are as follows: (1) 21 input nodes, (2) 20 neurons in the hidden layer, (3) 45 output nodes, (4) the required training error (MSE) = 0.015, (5) 1000 training epochs, and (6) the maximum failures of validation check = 6. During training, it was observed that after 200 epochs, the MSE requirement was fulfilled. The difference between network A and network B parameter settings is on the required MSE; this is because the output target is different for both networks. The 45 output nodes represent 45 grids as in the simulation design. The value of 0 or 1 was used in the output training data. The result of the network will be recognized as the multiplier coefficient (y_i), therefore the sum of all multiplication between each output node and its related Euclidean distance (E_i) on that node is the real output of the network (Y), as in Eq. (4-2). Figure 4.17 shows the type B network.

$$Y = \sum_{i=1}^{45} y_i E_i \tag{4-2}$$

The training process in the ANN has the purpose of updating the weight value in the connection between neurons. Many training algorithms have been found in the process of finding the minima in error space and speeding up the convergence. The multilayer network in this study was trained using the Levenberg-Marquardt (LM) algorithm. The LM algorithm blends the steepest descent method (error back-propagation) and the Gauss-Newton algorithm [52]. The LM algorithm integrates the speed advantage of the Gauss-Newton algorithm and the steepest descent's stability. It works by switching mechanisms; around the area with complex curvature, the LM algorithm uses the steepest descent algorithm; when the curvature is adequate to make a quadratic approximation, the LM algorithm uses the Gauss-Newton algorithm to speed up the convergence. In [52] it is shown that the Levenberg-Marquardt algorithm is

stable and fast, it surpasses the steepest descent algorithm, the Newton algorithm, and the Gauss-Newton algorithm.

The transfer function for the hidden layer is a hyperbolic tangent sigmoid, which compresses real numbers to range from [-1,1], while the transfer function in the output layer is linear.

4.5.3 Setup for the Experiment and Results

4.5.3.1 Setup for the Experiment

The MATLAB® program was used to execute the ANN training process and output calculation using network types A and B. The reliability test for those networks was also conducted using a MATLAB® program. The sensor data acquisition from ultrasonic receivers was made using C# program. The sampling rate for ultrasonic sensors and pressure sensor boards is 30 [Hz] in the specification of the controller as suggested in [74]; however, finally we got 26 [Hz] as final sampling rate due to the numbers of ultrasonic sensors and pressure sensors. To verify and validate the prediction of the step-length, we conducted a walking experiment using a shoe-type gait measurement device; data from one subject with 19 right steps and 18 left steps, the weight of the shoe was 1.2 [kg] including ultrasonic sensors, pressure sensors inside the insole board, IMU sensor, controller unit, wireless unit, and batteries. For a reference measurement, the measurement setup contained six OptiTrack® cameras as shown in Fig. 4.18(a). Reflective markers were placed on the heels in order to measure distance during walking as shown in Fig. 4.18(b). The real-time program in C# was made after all

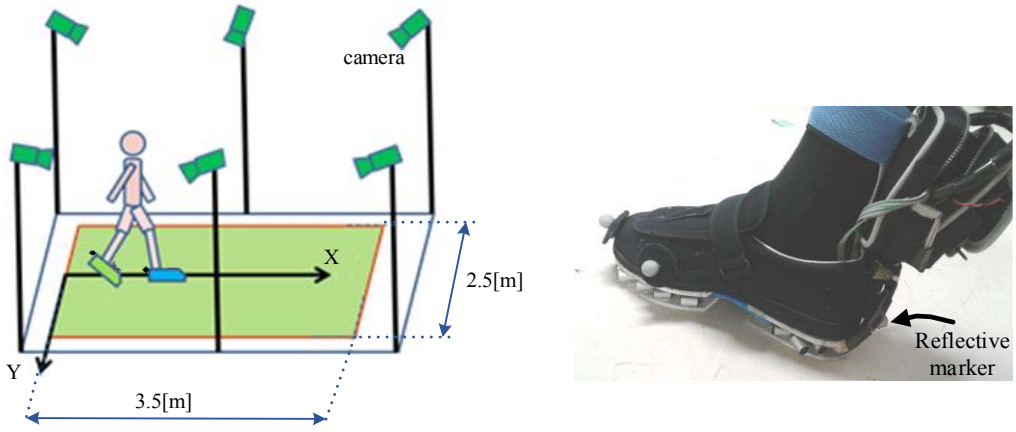

Figure 4.18 Measurement setup: (a) room setup for recording the markers distance; (b) shoe-type measurement device with reflective markers [22].

weights and biases have been resulted from the training process. The real-time program served as real application to the medics.

The experiment of walking as explained in the next subsection was conducted as a slow-walking type, using some observable conditions such as gait speed, cadence, and stance phase time, is described in Table 4.3.

Table 4.3 The experiment condition

Parameter	Value
Gait speed [m/s]	0.266
Cadence [steps/min]	42
Stance phase time [s]	0.73

4.5.3.2 Results of the Experiment

The first result is the training process for the networks. Network A took 55 minutes for the training process after 1000 epochs. As the learnable parameter number for network B is larger than that for network A, the training process for network B took 77 hours, and the performance MSE of 0.015 was reached after 200 epochs.

After finishing the training process for network A and network B, we conducted the reliability test to ensure that those networks were able to fit in all the data. The reliability-test data were chosen from trained and untrained data, and the performance was measured using RMSE (root mean square error). The result for network A indicates that the difference of RMSE between trained and untrained data is 3.86%, while in network B, the RMSE difference between trained and untrained is 0.83%.

The actual implementation experiment is the walking task. This experiment is derived from the average of six walking tasks. In each task of the walking experiment, we collected 3-4 steps from each foot. There are a total of 37 steps in this experiment, consisting of 19 right steps and 18 left steps. Figure 4.19 shows an example of one task in the walking experiment. In Fig. 4.19 (a), the marked numbers 1 to 6 indicate that there are six instances of step-length measurement. The corresponding distance between the markers on the heels is shown in Fig. 4.19 (b) by the motion-capturing measurement system. Overall, the performance of step-length prediction between network A and network B compared to the reference is shown in Table 4.4.

We also compared the results of the step-length prediction from the previous study when using the integration of gyro and ultrasonic sensors in the particle filter algorithm [40, 41]. The second comparison is from the work of B. Mariani, et al. [39] with the

prediction of stride length using temporal IMU data. In the third comparison of prediction using 5 [Hz] differential GPS (DGPS) as in [53], the step-length error was calculated using step duration (0.53±0.01 [s]) times the speed error per step (0.8 [cm/s]), which is 0.42 [cm] in the results. Table 4.5 shows the comparison results between ANN, particle filter, temporal IMU data, and DGPS.

Table 4.4 The result of walking task experiment in details and a comparison between networks A and B; mean absolute error is presented as mean (standard deviation) with all data in *cm*.

	Network A			**Network B**			Change in step
	Reference [cm]	Prediction [cm]	error [cm]	Reference [cm]	Prediction [cm]	error [cm]	
Right step	58.95	56.77	2.18	58.95	56.13	2.82	-
	57.19	55.33	1.86	57.19	55.62	1.57	1.76
	51.64	49.6	2.04	51.64	49.54	2.1	5.55
	51.4	50.15	1.25	51.4	49.8	1.6	0.24
	47.61	44.97	2.64	47.61	43.9	3.71	3.79
	50.45	49.37	1.08	50.45	49.82	0.63	2.84
	49.16	47.34	1.82	49.16	48.4	0.76	1.29
	50.3	48.05	2.25	50.3	47.2	3.1	1.14
	31.36	30.82	0.54	31.36	29.62	1.74	18.94
	47.71	45.42	2.29	47.71	43.49	4.22	16.35
	45.21	43.45	1.76	45.21	42.22	2.99	2.5
	47.23	45.78	1.45	47.23	43.66	3.57	2.02
	32.5	31.84	0.66	32.5	29.71	2.79	14.73
	38.93	36.73	2.2	38.93	40.92	1.99	6.43
	44.13	44.75	0.62	44.13	42.83	1.3	5.2
	39.42	37.2	2.22	39.42	41.11	1.69	4.71
	42.94	41.11	1.83	42.94	42.08	0.86	3.52
	37.33	35.56	1.77	37.33	41.73	4.4	5.61
	45.67	43.45	2.22	45.67	43.31	2.36	8.34
	Mean absolute error (sd)		1.72 (0.6)	Mean absolute error (sd)		2.33 (1.11)	

Table 4.4 continued							
	Network A			**Network B**			Change in step
	Reference [cm]	Prediction [cm]	error [cm]	Reference [cm]	Prediction [cm]	error [cm]	
Left step	49.53	47.83	1.7	49.53	44.7	4.83	3.86
	45.45	44.23	1.22	45.45	42.34	3.11	4.08
	38.93	35.14	3.79	38.93	32.94	5.99	6.52
	44.45	42.75	1.7	44.45	42.11	2.34	5.52
	46.83	43.99	2.84	46.83	40.55	6.28	2.38
	44.97	43.07	1.9	44.97	42.49	2.48	1.86
	44.9	42.94	1.96	44.9	42.12	2.78	0.07
	46.2	44.28	1.92	46.2	43.16	3.04	1.3
	39.57	35.94	3.63	39.57	35.01	4.56	6.63
	40.35	38.35	2	40.35	37.32	3.03	0.78
	43.51	41.73	1.78	43.51	41.81	1.7	3.16
	46.78	44.86	1.92	46.78	42.25	4.53	3.27
	43.46	45.02	1.56	43.46	36.77	6.69	3.32
	43.7	38.16	5.54	43.7	32.29	11.41	0.24
	44.45	41.67	2.78	44.45	45.6	1.15	0.75
	36.55	32.55	4	36.55	30.78	5.77	7.9
	39.94	36.62	3.32	39.94	33.12	6.82	3.39
	46.59	39.11	7.48	46.59	37.81	8.78	6.65
	Mean absolute error (sd)		2.84 (1.56)	Mean absolute error (sd)		4.74 (2.57)	Change in step mean= 4.63 (4.3)
Mean absolute error (sd) of all steps	Network A		2.26 (1.3)	Network B		3.50 (2.3)	

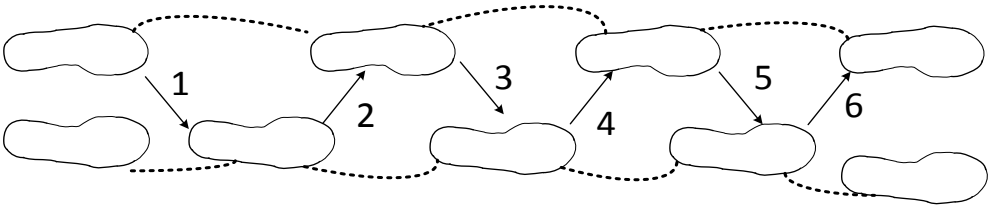

(a)

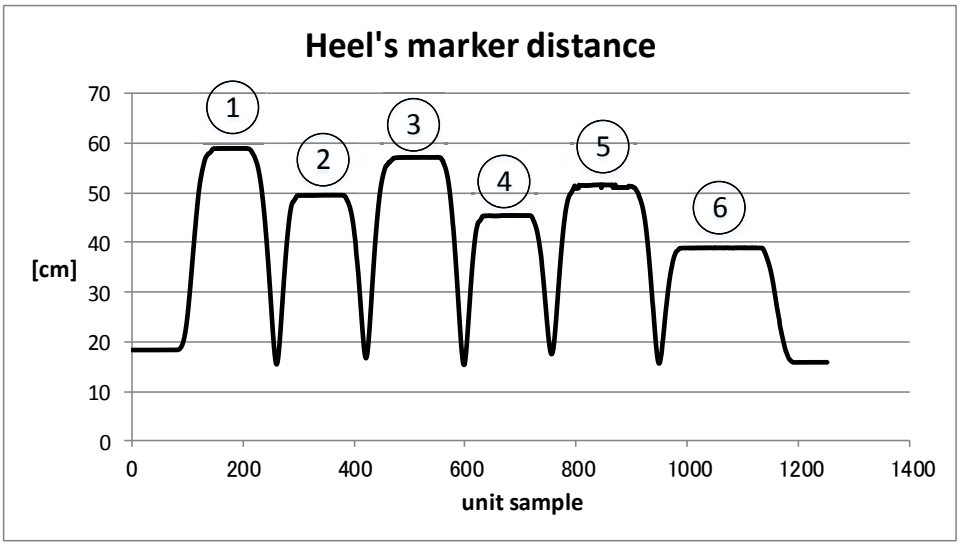

(b)

Figure 4.19 The illustration of one set of walking experiment: (a) One task of experiment consist of 3-4 steps of each foot. (b) the distance between two heels as a reference measurement from motion captures system [22].

Table 4.5 The comparison of average error of step-length prediction using four different methods; presented as mean (standard deviation).

Methods	Average error [cm]
ANN	2.26 (1.3)
Particle filter [40],[41]	4.00 (2.0)
Inertial sensor [39]	1.50 (6.8)
DGPS [53]	0.42 (0.01)

4.6 Discussion

The simulation was designed by moving the right shoe from region IV to VI (see region division in Fig. 4.2) and by rotating each ultrasound Rx to find the optimum heading angle. The results of the sensor position and angle have been concluded in Table 4.2, resulting in seven ultrasonic receivers and three ultrasonic transmitters. Using these sensors, the number and its angle; the implementation has been conducted as shown in Fig. 4.13. A test bed of 50x70 [cm] board area was used in the implementation. The result of the measurement scope in Fig. 4.15 shows some blank areas when the shoe position is on the straight line, for example, the left shoe on the coordinate (0,0) and the right shoe either on the (10,0), (20,0), (30,0), (40,0), or (50,0). This result was in line with the simulation design that the normal human steps fall either in the region IV or region VI. The straight-line position of two feet in the frontal axis is not found in normal walking. The distance between all ultrasonic receivers and transmitters was detected well until the coordinate of (50,70) or grid number 1, as shown in Fig. 4.15; this shows that the distance between two feet of the normal human step can be detected using this system.

In the simulation the foot progression angle that was used is 10 [deg] because the normal foot progression angle is 8-12 [deg]. The implementation results show that up to 30 [deg] of foot progression angle, the system still works well.

Comparing the training process between network A and network B, it was found that the type A network has a shorter training time and a smaller mean absolute error for all foot step than network B. Network B has more learning parameters to be updated in each epoch and showed that it needed to be standardized by Eq. (4-2). By using the reliability test, both types of networks were shown to be able to make prediction generalizations. The differences in RMSE between the untrained and trained data in both networks were below 5%. In regard to reliability, both networks are ready to be used for the shoe-type measurement device. Observing Table 4.4, it can be seen that network A has a better performance than network B in the left step, right step, and also in all step criteria. Finally, network A was chosen due to its efficacy.

By using our combined data from ultrasonic transmitters and receivers as inputs and by choosing the Levenberg-Marquardt algorithm as a training algorithm, we were able to solve our problem in step-length prediction. The error of the prediction as concluded in Table 4.4 indicates that the error of the left step is larger than the error in the right step. We presume that between the left and right shoe, the position and angle of sensors

is not exactly identical; this is due to the manual construction or hand-made construction. Since the training data come from one side of the step, that is, the right step; so we found that the prediction performance of the right step surpasses the performance of the left step. This is also a remarkably counsel for our experience in using artificial neural networks for solving the shoe-type measurement device problems in future study.

The comparison study of the step-length prediction has been shown in Table 4.5. At a glance, the prediction using DGPS by P. Terrier, et al. [53] surpasses other methods. However, GPS has shortcomings such as the high cost of professional equipment and is recommended only for outdoor analysis. The second-best prediction performance was proposed using inertial sensor by B. Mariani, et al. [39]. However, the complexity of inertial sensor data processing, *off-line* processing, and additional computational time might be one of the reasons to choose the ultrasonic sensor and ANN as a processing method for the shoe-type measurement device. Using the same kind of sensor as inputs, the ANN method surpasses the particle filter method; however, we do not claim that this condition is a global case, as many factors might influence reducing the particle filter method, such as the synchronization with gyro data as in [40], the difference of experimental conditions, and the number of sensors used.

4.7 Limitation and Affordable Error

The results of the simulation and implementation have succeeded in determining the position and angle of ultrasonic sensors. Likewise, the step-length prediction results showed an improvement of performance. From these results, we were able to ensure that the mechanism of simulation, implementation, and ANN architecture design have the influence to improve our shoe-type measurement device. Despite these improvements, there are several major limitations of the experiment that are described below.

The first limitation of the experiment is in the area of its scope. In this study, we used a 50x70 [cm] board based on a normal human walking area. In addition, we used the 30 [deg] of maximum foot progression angle (out-toeing). However, in the case of some gait impairments due to disease or injury, the foot progression angle is possibly in-toeing; it is also possibly that the walking base is more than 50 [cm]. For the time being, the shoe-type measurement device is suitable for the step-length measurement of a normal gait.

The second limitation is the design position of the ultrasonic transmitter on the medial heel of both feet with a 60 [deg] azimuth angle. This position, despite its efficacy to measure the distance on the range of the human step, has its flaws. It cannot precisely measure the distance between the two heels when the position of the foot is in a straight line of frontal axis to the body. This has been shown in Fig. 4.15 on grid numbers 8, 16, 24, 32, and 40.

The third limitation is related to the use of an artificial neural network as the two-stage regression. The step-length prediction using an artificial neural network has its flaws. One problem is that the ANN is like a black box; i.e., the mathematic model of the prediction cannot be defined. Another problem is that we cannot know which the final network is the best overall; it depends on the initial weight and biases in every training process.

The explanation of affordable error in this study is as follows. The empirical data refers to Table 4.4: 1) the mean absolute error is 2.26 [cm], 2) the average change of step-length is (4.6±4.3) [cm]. The step-length change is (4.6±4.3) [cm]; it means that in this range the common person walking did not consider or unconscious of his walking behavior that impact the change of step-length. On the other hand, the study error is 2.26 [cm] which is less than the average change of step-length. It means that the study error is still under common behavior of change, the present error is acceptable and not so big influence to gait monitoring. However, the effort to increase the accuracy should be headed in the future study.

4.8 Summary

One of the main contributions of this chapter is the presentation of techniques to simulate the ultrasonic sensor transmitter-receiver using *k-Wave*. The simulation aims to determine the number of sensors, the optimal sensor angle, and the sensor positions to be used in the shoe-type measurement device. By using the proper simulation parameter values, the position of sensors, the number of sensors, and the optimal sensors angles have been achieved, as shown in Table 4.2. The measurement scope has been validated by implementing the simulation result as an actual shoe-type measurement device. The range of the human step and foot progression angle were successfully cope using the number of sensors and its angle based on the actual measurement; the results of implementation have been concluded in Fig. 4.15 as the measurement scope diagram.

One of the real-world applications already mentioned as an objective is the prediction of step-length. By using our shoe-type measurement device, the prediction of human step-length can be achieved by implementing an artificial neural network to solve the nonlinearity of ultrasonic data. Despite the efficiency of the method, it still has its flaws; the step-length prediction error of the human walking experiment has been shown in Table 4.5 for ANN method and some others method. Nevertheless, as a future problem to be solved, we hypothesized that another spatial parameter of gait other than step-length, such as foot progression angle is possible to predict using these ultrasonic receivers' data.

This page intentionally left blank

5. Pressure Sensing

The shoe-type measurement device also equipped with pressure sensor in order to assess the pressure distribution when people walk. This chapter deals with 1) the background of pressure sensor selection; 2) the design of sensors' placement; 3) the calibration of load cell as a reference apparatus and sensors' calibration procedure, and 4) the in-shoe center of pressure measurement.

5.1 Related Technologies

Pressure is the measurement of force over an area. The three technologies to consider when measuring force or pressures are: 1) load cells, 2) pressure indicating film, and 3) tactile pressure mapping system; but for basic applications, it is considered using a tactile force sensor to replace the tactile pressure system [54]. The discussion below will explore each of those technologies in order to determine the best choice sensing pressure for the shoe-type measurement device.

The load cell is the famous one among the sensing pressure systems. Some technologies used in load cell are strain gauges, piezoelectric elements, and variable capacitance. Figure 5.1(a) illustrate the inside view of a load cell.

One of the limitations of load cells is its form factor; it is a bulky device. However, load cells give a very high reliability and accuracy. Some applications need more than one load cells to anticipate the limitation to measure the pressure on a surface, as shown in Fig. 5.1(b).

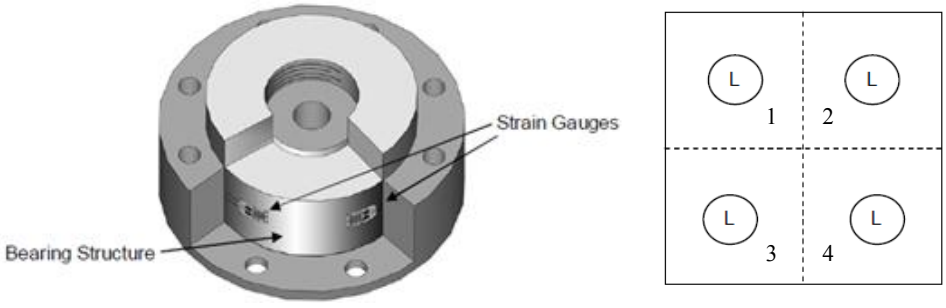

(a) (b)

Figure 5.1 (a) Inside view of a load cell; (b) one example of a measurement using multiple load cells [54]

Another technology in sensing pressure is the pressure indicating film that measures the pressure based on the intensity of the color on the film. The construction

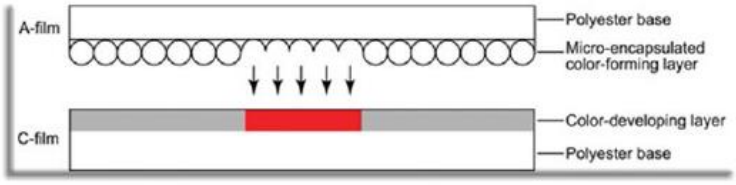

Figure 5.2 Components of pressure indicating film [54]

of the pressure-indicating film is shown in Fig. 5.2. Between two polyester base layers, a color developing material and micro-encapsulated color-forming part are next to the others. When pressure is applied to the polyester base layer, the proportional microcapsule will break suddenly and distribute ink where pressure is applied. Figure 5.2 shows components of the pressure-indicating film. The nature of the film only provides the peak pressure during pressure measurements; this limits the measurement of dynamic applications. The advantage of this type is in the flexibility of the film, it needs no wires or expensive electronics.

The tactile pressure sensor and the tactile force sensor work based on the piezo resistive material sandwiches between two pieces of flexible polyester [55]. On each layer, a conductive material (silver) is applied, followed by a layer of pressure-sensitive ink. The difference between tactile pressure and tactile force sensor is in its silver trace. The former used a matrix form of sensing traces, but the latter used a uniformly sensing area to measure the total force. Figure 5.3(a) illustrates the construction of a tactile pressure sensor and Fig. 5.3(b) is one example of tactile force sensor. The uses of flexible polyester material and silver ink result in an extremely thin sensor. But like a load cell, a tactile force sensor will only provide information of the total force applied to the sensing area.

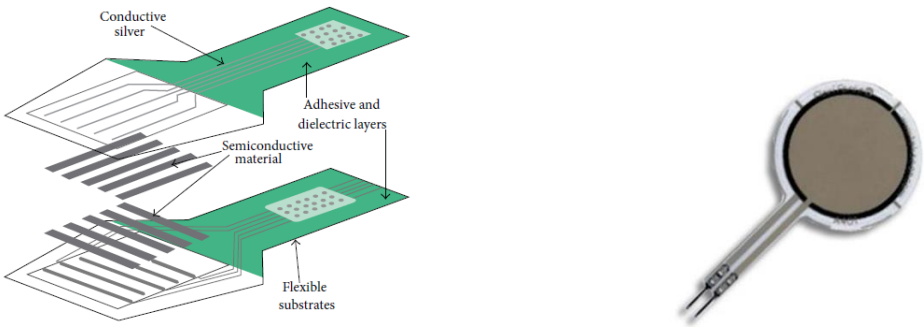

(a) (b)

Figure 5.3 (a) Construction of a tactile pressure sensor; (b) tactile force sensor [54]

To summary, based on the three technologies that have been discussed, the load cells form factor restrict the using of load cell in shoe-type measurement device, although load cells provide the most reliable data. Also, we found that the pressure-indicating film could not provide the range of forces applied in dynamic applications; this will also restrict the using of this technology in the shoe-type measurement device. The tactile pressure sensor and the tactile force sensor promising to be used in the shoe-type measurement device due to its flexibility form, the ability to provide detailed dynamic measurement, and relatively low cost. The using of the tactile force sensor needs to be properly calibrated to provide accurate data.

In this study, we choose a tactile force sensor based on the discussion above to measure the force applied on a shoe sole when people walk. A tactile force sensor manufactured by Tekscan, Inc., FlexiForce sensor, model A201 is used. Table 5.1 lists the relevant parameters of FlexiForce sensor.

Table 5.1 The selected standard FlexiForce sensor Model A201 [55]

Thickness	0.208 [mm]
Length	102 [mm]
Width	14 [mm]
Sensing area (diameter)	9.53 [mm]
Connector	3-pin male
Force range	0-100 [lbs] (440 [N] = 45.36 [kg])
Operating temperature	-9^{o} [C] to 60^{o} [C]
Linearity (Error)	+/- 3%
Repeatability	+/- 2.5% of full scale (conditioned sensor, 80% force applied)
Hysterisis	< 4.5% of full scale (conditioned sensor, 80% force applied)
Drift	< 5% per logarithmic time scale (constant load of 90% sensor rating)
Response Time	< 5 [μs]
Output Change/Degree	Up to 0.2% (~0.36% / ^{o}[C]). Loads < 10 [lbs], operating temperature can be increased to 74^{o} [C]

5.2 Placement of the Tactile Force Sensor

We place the sensor under the foot inside the shoe beneath the tarsals, metatarsals, and phalanges. The plantar surface was divided to be four regions as shown in Fig. 5.4:

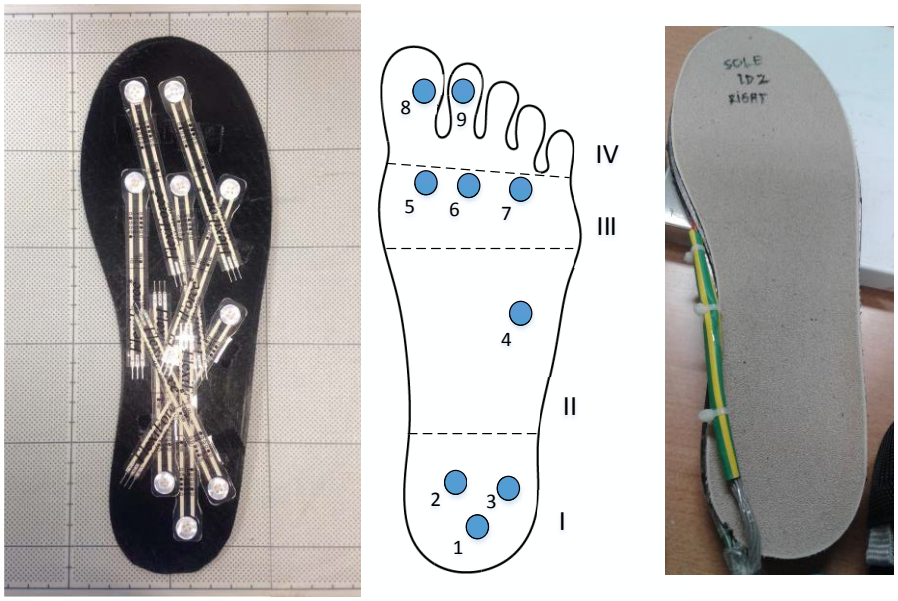

(a) (b) (c)

Figure 5.4 (a) The sensors position on the first insole board; (b) graphical representation of the plantar surface regions and sensors numbers: I) heel region, II) midfoot region, III) forefoot region, and IV) toes region; (c) final insole board

1) heel region, 2) midfoot region, 3) forefoot region, and 4) toes (big toe and lesser toes), in order to detect the pressure in gait phases [56].

Figure 5.4(b) illustrates the position and sensors number. The presence of forces only in sensors number 1, 2, and 3 indicate the "heel strike" phase; all sensors numbers 1 to 9 are for "loading response/foot flat" phase; sensors numbers 4 to 9 is for detecting "terminal stance/heel off" phase; and sensors number 8 and 9 are for "preswing/toe off" phase.

The pressure or force applied to the plantar surface is larger than the sensing area of the sensor. Therefore, it is necessary to use a "puck." We use a button as a puck and paste it above the sensing area and make sure that all button surface smaller than the sensing area of the sensor. In order to protect the "puck" surface and user comfortability, the second insole board covered all sensors as shown in Fig. 5.4(c) as a final insole board.

5.3 Calibration Procedure and Results

5.3.1 Load Cell Calibration

To measure the force applied as a reference, the load cell manufactured by Toyo Sokki, Co., Ltd Type PLP-10L-180/cap.10 [kg], Kyowa's strain amplifier DPM-711B, DAQ NI USB-6212, and stainless steel precision weight by Murakami Koki, Co., Ltd. were used, as shown in Fig. 5.5.

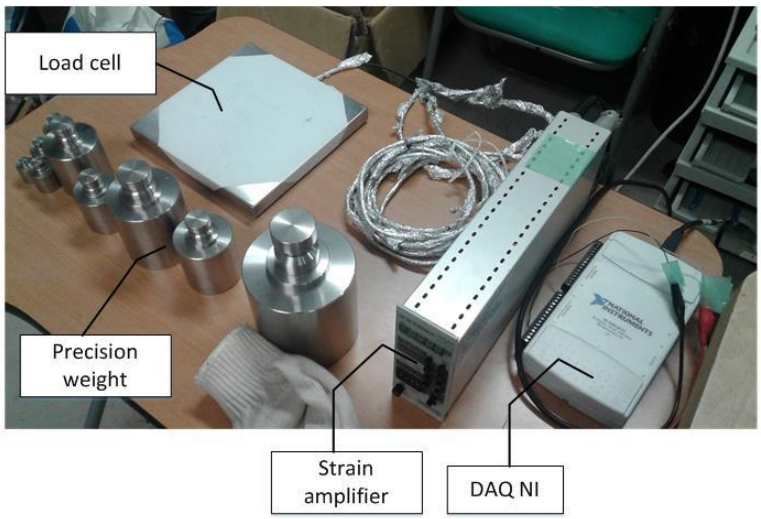

Figure 5.5 Apparatus for load cell calibration

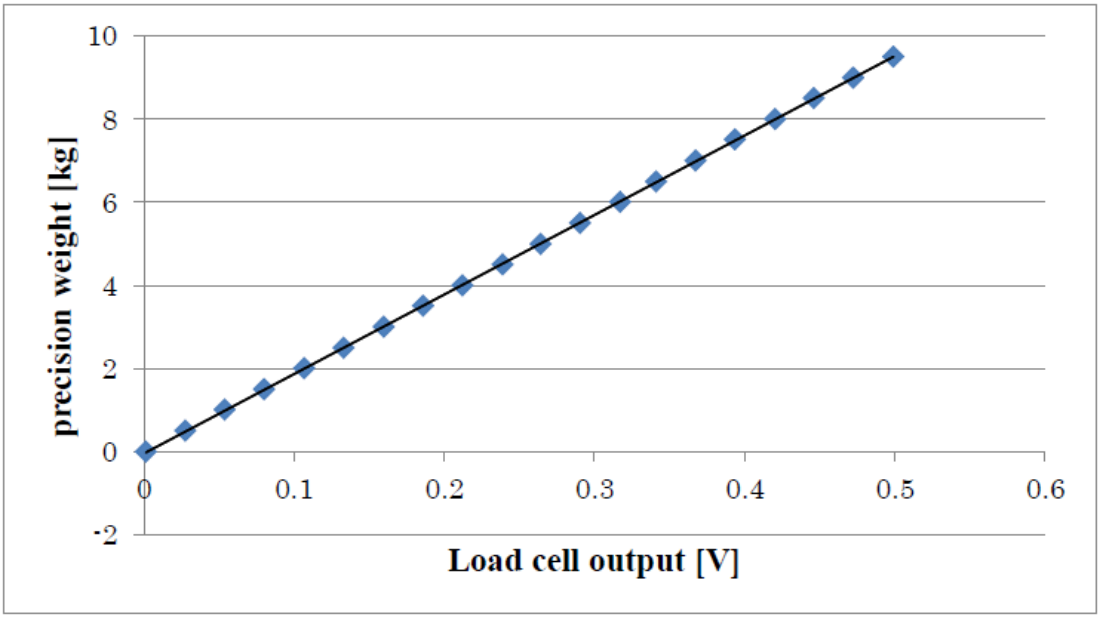

Figure 5.6 Load cell calibration curve

The Murakami's precision weight was used to apply the force every 0.5 [kg] from 0.5 [kg] to 9.5 [kg]. Then the output of strain amplifier will be record by C# acquisition program through a National Instrument DAQ. Figure 5.6 shows the line fit to the precision weight, the relationship between the load cell outputs in volts, V_L, and the applied precision weight in kg, Y, is described in (1). The coefficient of determination (R^2) is a number that indicates the proportion of the variance in the variable Y that is predictable from the variable V_L; the value 1 indicates that Eq. (5-1) is 100% fit:

$$Y = 19.119V_L - 0.0436 \qquad R^2=1 \qquad (5\text{-}1)$$

5.3.2 Tactile Force Sensor Calibration

A tactile force sensor's output is non-linear, indicated by the report in Table 5.1. The repeatability is from $\pm 2.5\%$ of full scale. The calibration and sensor performance characteristics are related each other, such as: repeatability, linearity, hysteresis, drift, and temperature sensitivity. We tried to calibrate as the standard procedure and paid attention to keep the performance of the sensor. The result of this calibration is in units of applied force in kg will be used to calculate center of pressure in the next subsection.

Repeatability is the ability of the sensor to respond in the same way to a repeatedly applied force [55]. To ensure the repeatability, the sensor needs to be "conditioning" or "exercising" before calibrating it. The sensor that was used, had a force range of 0 to 440 [N] (0 to 45 [kg]); to condition this sensor, we press the sensor until 110% of 45

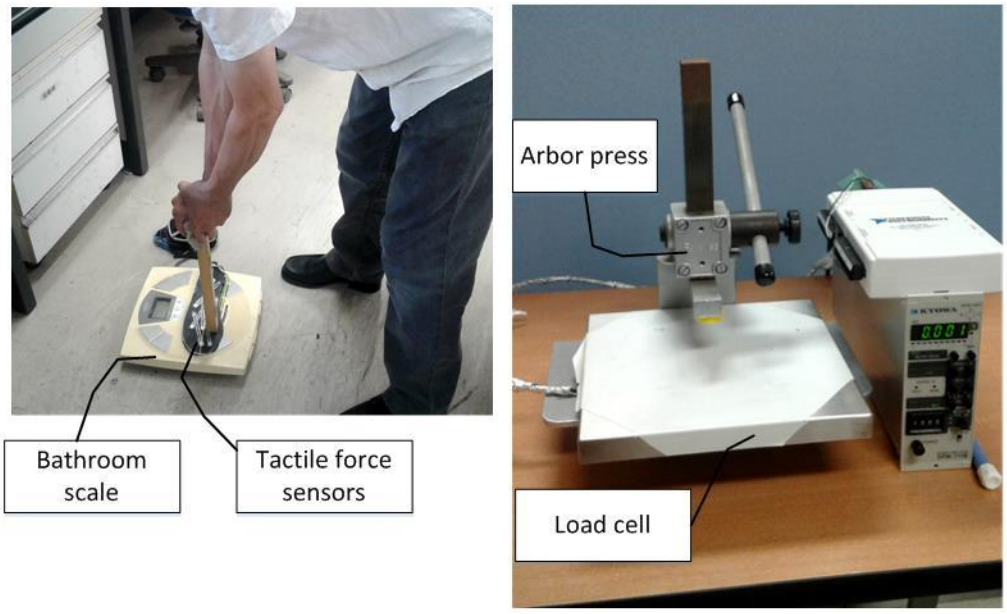

Figure 5.7 (a) Conditioning sensors before calibration; (b) calibration process apparatus

[kg], which is around 49.5 [kg], using a wooden stick and a bathroom scale around four to five times, as shown in Fig. 5.7 (a).

Another sensor performance characteristic is "drift." Drift is the change in sensor output when a constant force is applied over a period of time. To take drift into account when calibrating the sensor, the sensor calibration performs in a time frame similar to that, which will be used in the application. The force from human gait impact the sensors periodically, as there are stance and swing phase of gait; therefore, the calibration of each sensor will be imitate this pattern, and the pressing and releasing action will be applied to each sensor using an arbor press, which is the reversible arm applies up to 227 [kg] of pressure. This tool is manufactured by Pana Vise Product, Inc., as shown in Fig. 5.7 (b). To calibrate each sensor, the force was applied to each sensor on both insoles. Each sensor was placed on the top of load cell and will be pressed ten times in order to find the line fit. The excitation circuit transforms the resistance to voltage, and a 12-bit digital output in the range 0-4095 was produced by an ADC. One example of the experiment's raw data from sensor number 5 on the left shoe is shown in Fig. 5.8. This shows that two curves are almost identical.

The consideration of temperature is also one of the concerns in calibrating the sensors. As long as our shoe-type measurement device will be used in indoor operation, the calibration process also done in the room temperature, that is 25^{o}–26^{o} [C].

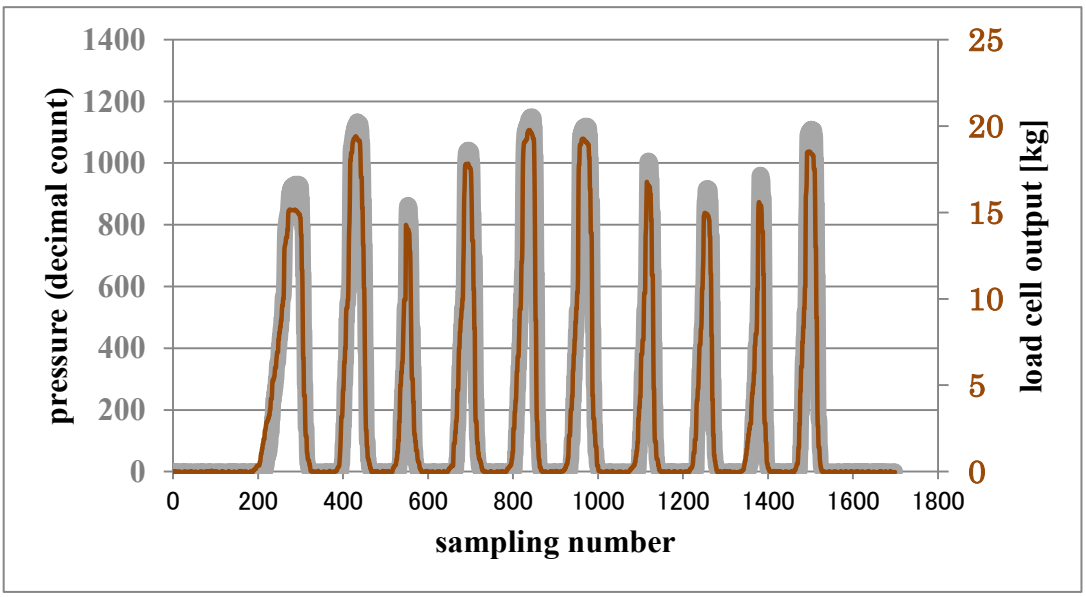

Figure 5.8 Sample tactile force sensor and load cell calibration data, example in sensor number 5 of left shoe.

Linearity refers to the sensor's response to the applied load, over the range of the sensor. A calibration is performed to "linearize" the sensor's output as much as possible [55]. The comparison of RMSE (root mean square error) from polynomial *p(x)* of degree 1, 2, and 3 will be counted to find the best fit for the data in *y*. The RMSE formula as in Eq. (5-2) and polynomial *p(x)* as in Eq. (5-3) will be used:

$$RMSE = \sqrt{\frac{\sum_{k=1}^{n} (\hat{y}_k - y_k)^2}{n}} \tag{5-2}$$

where $\hat{y}_k$ is the predicted value from polynomial in (3), y_k is scale value, all unit is in [kg].

$$p(x) = p_1 x^3 + p_2 x^2 + p_3 x + p_4 \tag{5-3}$$

Figure 5.9 shows one example of a calibration curve; it was taken from sensor number 5 of the left shoe. The curves in Fig. 5.9 are related to the first-degree and third-degree of the polynomial line-fit. The RMSE values of the polynomials of degree 1, 2, and 3 for each sensor are presented in Table 5.2, which calculates RMSE values

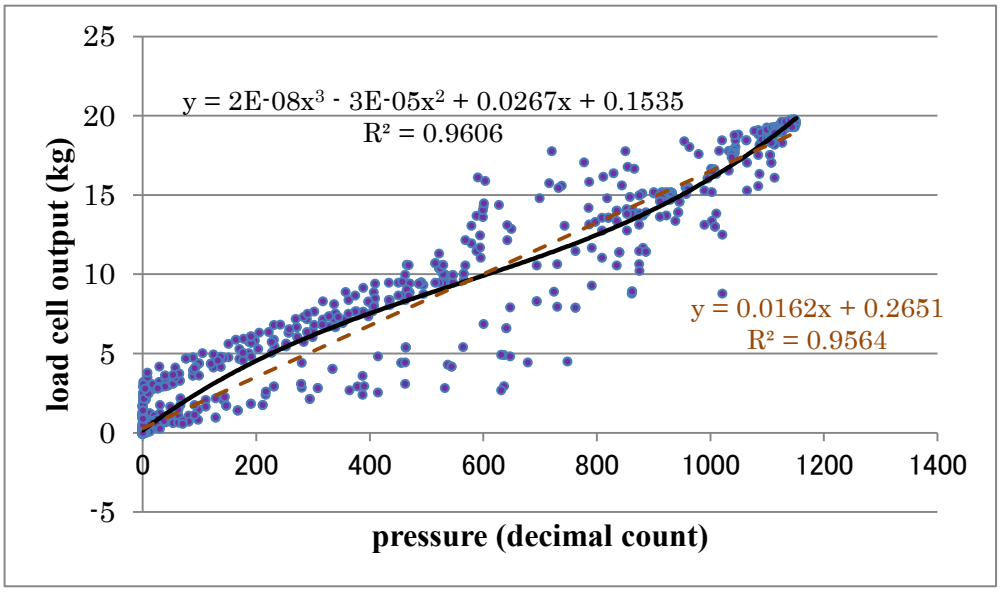

Figure 5.9 One-degree and the third-degree of polynomial line-fit to the tactile force sensor. based on Eq. (5-2).

Table 5.2 A comparison table of RMSE on each sensors

Insole board	Sensor number	RMSE of polynomial		
		Degree 1 [kg]	Degree 2 [kg]	Degree 3 [kg]
left	1	2.88	2.55	2.47
	2	1.08	1.07	1.06
	3	1.43	1.43	1.33
	4	1.13	1.08	1.07
	5	1.25	1.24	1.19
	6	1.02	0.97	0.95
	7	1.26	1.03	0.97
	8	1.96	1.64	1.58
	9	1.14	1.14	1.04
right	1	2.10	2.06	2.05
	2	1.39	1.39	1.36
	3	1.60	1.60	1.59
	4	1.99	1.97	1.95
	5	1.40	1.40	1.39
	6	1.71	1.70	1.61
	7	1.90	1.83	1.83
	8	1.19	1.15	1.15
	9	1.63	1.54	1.52

Table 5.3 presents the polynomial *p(x)* of degree-3 and degree-1 of each sensor on the left and right shoe as a comparison. The zero offset value that represents when the sensor encounters no load was not required. During the swing phase of walking, the sensors are not expected to be zero, because the shoelaces are tied snugly, causing pre-loaded force. The last column in Table 5.3 was used in a calibration program for each sensor.

Table 5.3 A comparison table of polynomial of degree 3 and 1.

Insole board	Sensor number	Degree 3 - polynomial	Degree 1 - polynomial	Degree 1 without offset
left	1	$p(x) = 8E\text{-}8x^3\text{-}0.00013x^2\text{+}0.0717x\text{+}1.5162$	$p(x) = 0.025x + 2.031$	$p(x) = 0.0285x$
	2	$p(x) = 2E\text{-}8x^3\text{-}3E\text{-}5x^2\text{+}0.032x\text{+}0.1236$	$p(x) = 0.025x + 0.217$	$p(x) = 0.025x$
	3	$p(x) = 1E\text{-}8x^3\text{-}2E\text{-}5x^2\text{+}0.022x\text{+}0.2256$	$p(x) = 0.012x + 0.366$	$p(x) = 0.0127x$
	4	$p(x) = 2E\text{-}9x^3\text{-}2E\text{-}6x^2\text{+}0.008x\text{-}0.0538$	$p(x) = 0.009x - 0.149$	$p(x) = 0.0088x$
	5	$p(x) = 2E\text{-}8x^3\text{-}3E\text{-}5x^2\text{+}0.0267x\text{+}0.1535$	$p(x) = 0.016x + 0.265$	$p(x) = 0.0166x$
	6	$p(x) = 4E\text{-}9x^3\text{-}6E\text{-}6x^2\text{+}0.0121x\text{+}0.0526$	$p(x) = 0.011x - 0.011$	$p(x) = 0.0113x$
	7	$p(x) = 4E\text{-}9x^3\text{-}6E\text{-}6x^2\text{+}0.0092x\text{+}0.0316$	$p(x) = 0.010x - 0.140$	$p(x) = 0.0096x$
	8	$p(x) = 8E\text{-}8x^3\text{-}0.00012x^2\text{+}0.066x\text{+}0.46$	$p(x) = 0.031x + 0.821$	$p(x) = 0.0329x$
	9	$p(x) = 7E\text{-}9x^3\text{-}1E\text{-}5x^2\text{+}0.0195x\text{+}0.2634$	$p(x) = 0.012x + 0.321$	$p(x) = 0.0126x$
right	1	$p(x) = 9E\text{-}9x^3\text{-}2E\text{-}5x^2\text{+}0.0252x\text{-}0.0571$	$p(x) = 0.015x + 0.139$	$p(x) = 0.0151x$
	2	$p(x) = 4E\text{-}9x^3\text{-}9E\text{-}6x^2\text{+}0.0142x\text{-}0.0312$	$p(x) = 0.009x + 0.037$	$p(x) = 0.0095x$
	3	$p(x) = 4E\text{-}9x^3\text{-}8E\text{-}6x^2\text{+}0.0132x\text{+}0.0428$	$p(x) = 0.010x + 0.076$	$p(x) = 0.0098x$
	4	$p(x) = -2E\text{-}8x^3\text{+}2E\text{-}5x^2\text{+}0.0127x\text{-}0.0286$	$p(x) = 0.016x - 0.008$	$p(x) = 0.0164x$
	5	$p(x) = -1E\text{-}8x^3\text{+}2E\text{-}5x^2\text{+}0.0135x\text{-}0.0421$	$p(x) = 0.019x - 0.111$	$p(x) = 0.0188x$
	6	$p(x) = 2E\text{-}8x^3\text{-}4E\text{-}5x^2\text{+}0.0305x\text{+}0.1080$	$p(x) = 0.015x + 0.260$	$p(x) = 0.0153x$
	7	$p(x) = 1E\text{-}9x^3\text{-}1E\text{-}5x^2\text{+}0.0217x\text{-}0.0278$	$p(x) = 0.014x + 0.136$	$p(x) = 0.0142x$
	8	$p(x) = 2E\text{-}9x^3\text{-}1E\text{-}6x^2\text{+}0.0095x\text{-}0.0314$	$p(x) = 0.011x - 0.118$	$p(x) = 0.0105x$
	9	$p(x) = 6E\text{-}9x^3\text{-}7E\text{-}6x^2\text{+}0.0127x\text{-}0.0169$	$p(x) = 0.013x - 0.124$	$p(x) = 0.0126x$

5.4 In-Shoe Center of Pressure

In-shoe pressure measurement systems allow for the calculation of center of pressure (CoP) between the foot and the shoe or the foot and the orthosis inside the shoe [63]. The foot's CoP is the average location of all pressures acting on the foot at any given time [60]. During the stance phase, a means of averaging CoP paths is located at the medial point of the hind foot during initial contact and moves anteriorly, curving laterally at mid-stance and progressing medially to the first two metatarsal heads at terminal stance [60, 61]. According to another definition, the CoP is the point at which the resultant force of all ground reaction forces acts [59]. The CoP formula is presented as a weighted pressure formula in Eq. (5-4) and (5-5) [58, 59, 62, 63].

$$CoP(x) = \frac{\sum_{i=1}^{n} X_i P_i}{VRF}, \quad CoP(y) = \frac{\sum_{i=1}^{n} Y_i P_i}{VRF} \tag{5-4}$$

The term VRF (vertical reaction force) is defined as the sum of all pressure in sensors.

$$VRF = \sum_{i=1}^{n} P_i \tag{5-5}$$

P_i represents the measurement of pressure in the i^{th} sensor, and X_i and Y_i are the corresponding coordinates of each sensor position in the x and y axis. Figure 5.10 and Table 5.4 represent the distance between X_i and Y_i related to the sensors' numbers.

The implementation of CoP calculation in Eq. (5-4) results in a CoP path. Implementation is performed using C# program, and the coordinates of CoP path can be recorded to a file for gait analysis by a physician. Figure 5.11 shows a capture of the foot pressure display location, including CoP path in slow walking.

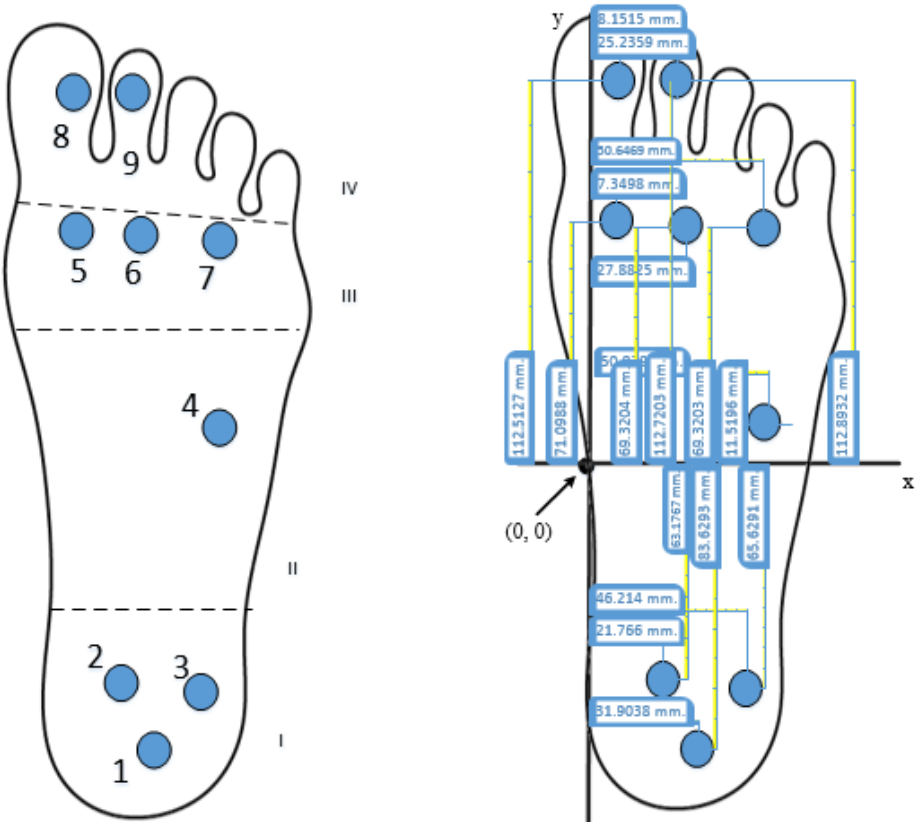

(a) (b)

Figure 5.10 (a) The sensors position and its numbers; (b) graphical representation of the X and Y between each sensor and the origin point (0,0)

Table 5.4 The horizontal (X) and vertical (Y) coordinates of sensor position to origin point (0,0) as in Fig. 5.10.

coordinate	Sensors' number								
	1	2	3	4	5	6	7	8	9
x [mm]	35.71	24.36	51.72	57	8.23	31.21	56.68	9.12	28.24
y [mm]	-94.05	-71.05	-73.80	12.95	79.95	77.95	77.95	126.53	126.95

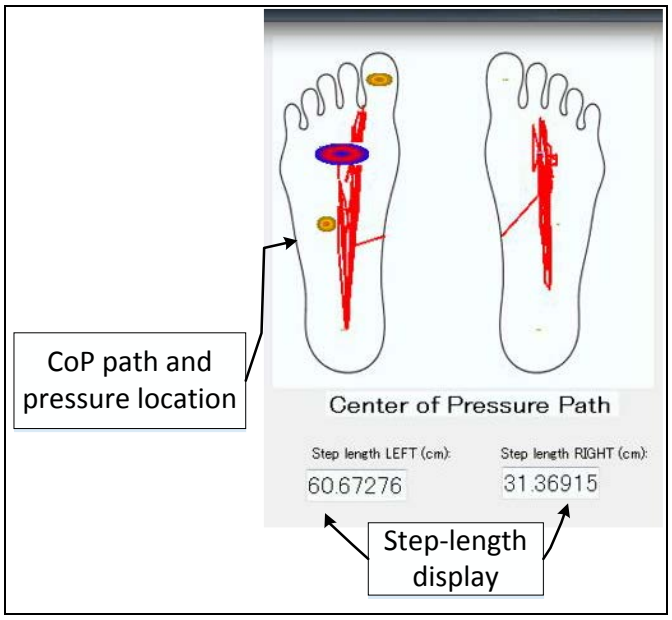

Figure 5.11 The pressure location and center of pressure display.

5.5 Implementation Results

5.5.1 Test Setup

To validate the in-shoe CoP system, the conducted experiment used in-shoe pressure sensors, an OptiTrack® motion capture system, and an Advanced Medical Technology Inc. (AMTI) force plate (AMTI, Watertown MA, USA) were used.

The two AMTI model OR6-7-2000 force plates measured the instantaneous pressure of each foot (CoP-FP), and the motion capturing system recorded the markers position at a sampling rate of 100 [Hz]. During the data analysis, only the CoP-FP from the second platform will be used. The CoP from the in-shoe (in-shoe CoP) was recorded using the C# program at a sampling rate of 30 [Hz]. The cubic spline interpolation was used to normalize time between both systems. Figure 5.12 shows the measurement

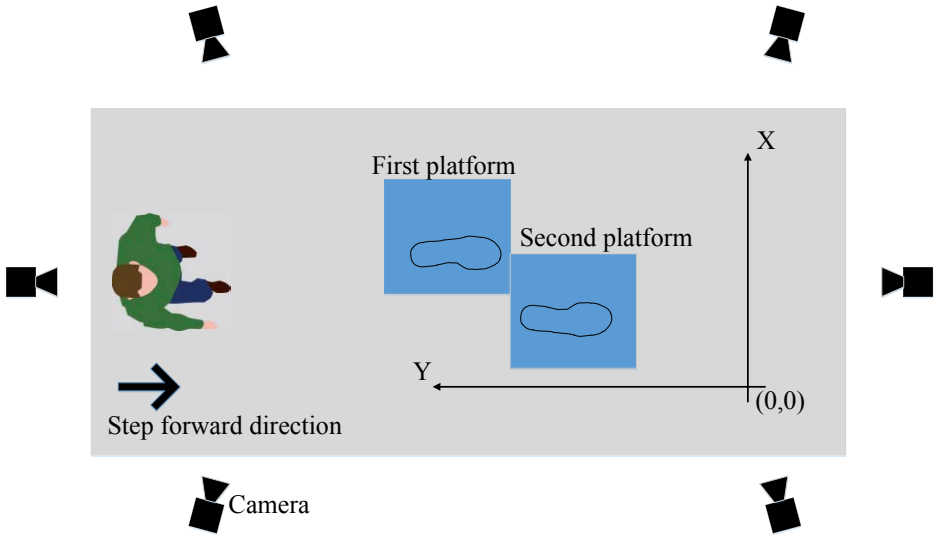

Figure 5.12 Experimental setup: a walkway that equipped with two force plates in semi tandem.

Figure 5.13 Five calibration markers position on the right shoe and four markers on the force plate

setup for validating the in-shoe CoP. Figure 5.13 shows five reflective markers position on the right shoe, and four markers on the corner of the second force platform.

The experimental design is as follows: Two healthy male and two female students (aged 22 to 27) volunteered for the study. The subjects were instructed to walk six times along a walkway, as in Fig. 5.12. However, during analysis, we only used half of the data due to bad data collection. Data were saved simultaneously by the C# program and the motion capture system, including force plate data. Only the steps of the right foot on the second platform were used for analyzing.

5.5.2 The Coordinate System and Experimental Results

The validation of the CoP path between in-shoe pressure system and force plate was executed in the global coordinate system (GCS); for this purpose, there were two steps: 1) The first, calculate the rotation matrix to transform the ground reaction force (GRF) from the force plate coordinate system (FCS) into the GCS. The calculation follows the ordering marker number as in Fig. 5.13.

The origin of the force plate is as follows:

$$\mathbf{O}_{FP} = 0.25(\mathbf{M}_6 + \mathbf{M}_7 + \mathbf{M}_8 + \mathbf{M}_9) \tag{5-6}$$

A unit vector along the *x*-axis of the second platform as follows:

$$\hat{\mathbf{i}}' = \frac{\mathbf{M}_8 - \mathbf{M}_7}{|\mathbf{M}_8 - \mathbf{M}_7|} \tag{5-7}$$

Another unit vector along the platform surface as follows:

$$\hat{\mathbf{v}} = \frac{\mathbf{M}_8 - \mathbf{M}_9}{|\mathbf{M}_8 - \mathbf{M}_9|} \tag{5-8}$$

The surface normal vector, derived from the cross product of the $\hat{\mathbf{i}}'$ and $\hat{\mathbf{v}}$ unit vectors:

$$\hat{\mathbf{k}}' = \hat{\mathbf{i}}' \times \hat{\mathbf{v}} \tag{5-9}$$

The last unit vector derived from the cross product:

$$\hat{\mathbf{j}}' = \hat{\mathbf{k}}' \times \hat{\mathbf{i}}' \tag{5-10}$$

The rotation matrix to convert the coordinates of a point **P** in the laboratory coordinate system (GCS), into **P'** in the force plate coordinate system (LCS), can be expressed as:

$$\mathbf{R}_{FP} = \begin{bmatrix} \hat{\mathbf{i}}'_x & \hat{\mathbf{i}}'_y & \hat{\mathbf{i}}'_z \\ \hat{\mathbf{j}}'_x & \hat{\mathbf{j}}'_y & \hat{\mathbf{j}}'_z \\ \hat{\mathbf{k}}'_x & \hat{\mathbf{k}}'_y & \hat{\mathbf{k}}'_z \end{bmatrix} \tag{5-11}$$

To transform the CoP from the FCS into the GCS:

$$\mathbf{CoP}_{FP} = \mathbf{R}'_{FP}\mathbf{CoP}'_{FP} + \mathbf{O}_{FP} \tag{5-12}$$

2) The second conversion was from the shoes coordinate system (SCS) to GCS in order to transform the in-shoe CoP coordinate from SCS to GCS. The conversion follows the ordering marker number, as in Fig. 5.13.

The origin of the in-shoe pressure is the fifth marker position ($\mathbf{M}_5$), as in Fig. 5.13, and in accordance to the designed coordinate system in Fig. 5.10. In the implementation, we added an offset of 2 [cm], assuming there was distance between the coordinates of marker $\mathbf{M}_5$ and the true origin of the in-shoe pressure system in the medio-lateral direction.

$$\mathbf{O}_{shoe} = \mathbf{M}_5 + offset \tag{5-13}$$

A unit vector along the medio-lateral (ML) of the right shoe:

$$\hat{\mathbf{i}}'_{shoe} = \frac{\mathbf{M}_4 - \mathbf{M}_3}{|\mathbf{M}_4 - \mathbf{M}_3|} \tag{5-14}$$

Another unit vector along the sole surface of the shoe:

$$\hat{\mathbf{v}}_{shoe} = \frac{\mathbf{M}_1 - \mathbf{M}_2}{|\mathbf{M}_1 - \mathbf{M}_2|} \tag{5-15}$$

Same as Eq. (5-9), the surface normal vector was created from the cross product of the $\hat{\mathbf{i}}'_{shoe}$ and $\hat{\mathbf{v}}_{shoe}$ unit vectors.

$$\hat{\mathbf{k}}'_{\mathbf{shoe}} = \hat{\mathbf{i}}'_{\mathbf{shoe}} \mathbf{x} \hat{\mathbf{v}}_{\mathbf{shoe}} \tag{5-16}$$

The last unit vector derived from the cross product:

$$\hat{\mathbf{j}}'_{\mathbf{shoe}} = \hat{\mathbf{k}}'_{\mathbf{shoe}} \mathbf{x} \hat{\mathbf{i}}'_{\mathbf{shoe}} \tag{5-17}$$

The rotation matrix from GCS into SCS can be expressed as:

$$\mathbf{R}_{\mathbf{shoe}} = \begin{bmatrix} \hat{\mathbf{i}}'_{\mathbf{shoe},x} & \hat{\mathbf{i}}'_{\mathbf{shoe},y} & \hat{\mathbf{i}}'_{\mathbf{shoe},z} \\ \hat{\mathbf{j}}'_{\mathbf{shoe},x} & \hat{\mathbf{j}}'_{\mathbf{shoe},y} & \hat{\mathbf{j}}'_{\mathbf{shoe},z} \\ \hat{\mathbf{k}}'_{\mathbf{shoe},x} & \hat{\mathbf{k}}'_{\mathbf{shoe},y} & \hat{\mathbf{k}}'_{\mathbf{shoe},z} \end{bmatrix} \tag{5-18}$$

To transform the in-shoe CoP path from the SCS to GCS, the rotation matrix is as follows:

$$\mathbf{CoP}_{in-shoe} = \mathbf{R}'_{shoe}\mathbf{CoP}'_{in-shoe}+\mathbf{O}_{shoe} \quad (5\text{-}19)$$

where the $\mathbf{CoP}'_{in-shoe}$ was determined by a weighted pressure formula in Eq. (5-4) and (5-5).

All comparisons in the experiment results were taken along the same coordinates of the anterior-posterior location between the force plate and the in-shoe pressure system, by omitting the undetected area. The results are shown in Table 5.5, which consists of the root mean square (RMS) error comparison between the in-shoe CoP, and the CoP-FP on the *x*-axis direction (medio-lateral) and on the *y*-axis direction (anterior-posterior). Table 5.5 also presents the Pearson Correlation Coefficient (PCC) of the medio-lateral and anterior-posterior locations between both systems.

Table 5.5 The RMS error and Pearson Correlation comparison of the medio-lateral and anterior-posterior locations of the in-shoe CoP and CoP-FP.

	Medio-lateral	Anterior-posterior
RMS error [cm]	0.86±0.27	2.67±1.35
Pearson correlation	0.64±0.39	0.90±0.08

Illustration of the experimental data from one subject will be presented in the time domain, as shown in the Fig. 5.14 for the *x*-axis and *y*-axis, respectively. The local coordinate system consists of the force-plate coordinate system and the shoes coordinate system, while the global coordinate system is derived from Eq. (5-12) and (5-19).

Figure 5.15(a) presents the *x-y* graph or combination graph of Fig. 5.14, while Fig. 5.15(b) presents another example of data from the other subject.

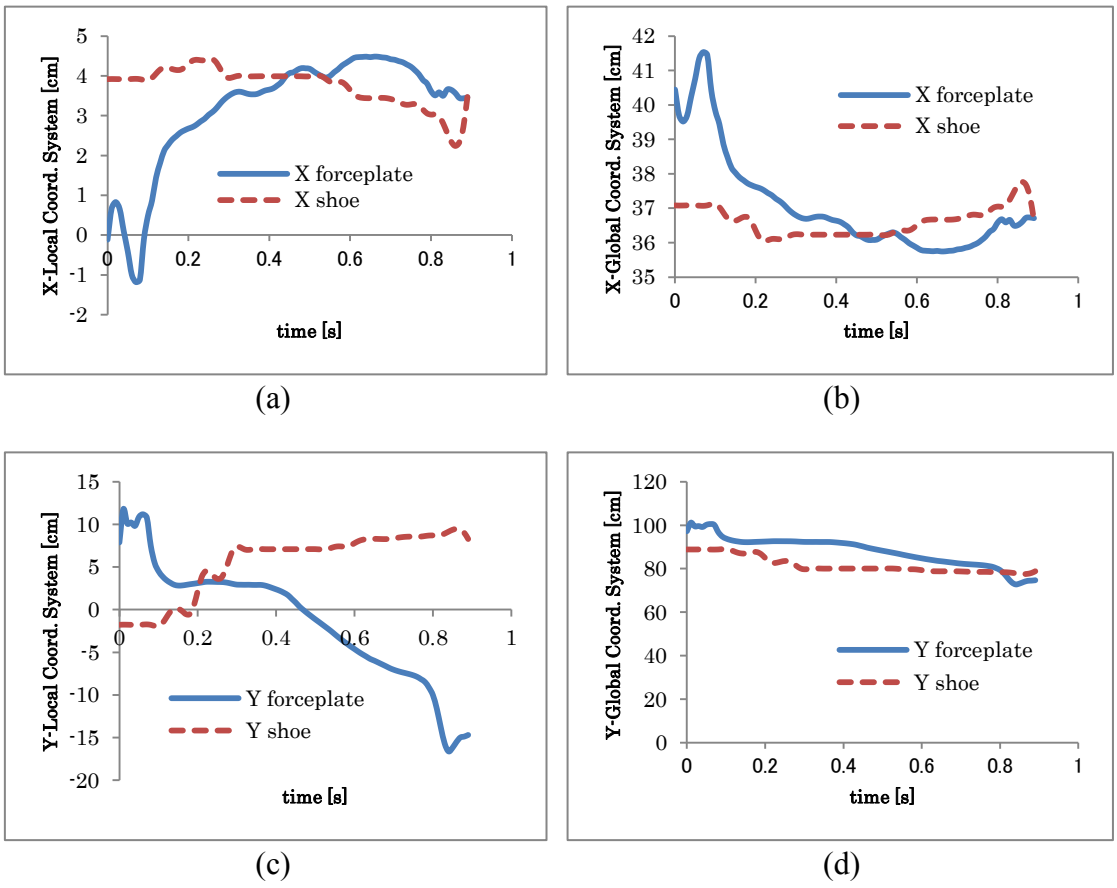

Figure 5.14 The example of the x-axis and y-axis CoP path: (a) and (c) CoP in the local coordinate system, (b) and (d) CoP in the global coordinate system.

5.6 Discussion

The calibration of the load cell in section 5.3.1 (Fig. 5.6) indicates that load cell output is linearly related to precision weight. The result ensures that the load cell and strain amplifier can be used as a reference system to calibrate each tactile force sensor.

In the section calibration of the tactile force sensor, the data presented in Table 5.2 shows that a third-degree polynomial has a relatively small RMSE value, providing a good fit with the data. However, in Table 5.3, the coefficients of polynomials x^3 and x^2 are almost zero, and the R^2 (coefficient of determination) in the polynomial of degree 3 and polynomial of degree 1 is not significantly different, which leads to the decision to

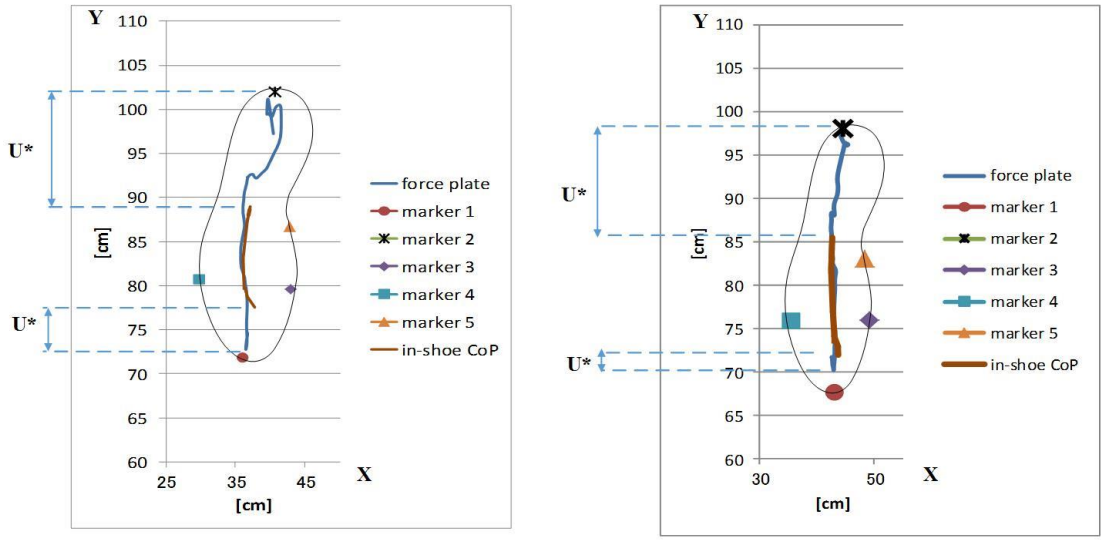

(a) (b)

Figure 5.15 The examples result of CoP path of force plate and in-shoe pressure system in global coordinate system. The shoe sole frame is an additional figure for the purpose of ease visualization. U* is the undetected measurement area.

choose a polynomial of degree 1 as the final fitting line. The present study limits the analysis to polynomials of degree 3 because higher-order polynomials can be oscillatory between the data points, leading to a poorer fit to the extrapolated data. The last column of Table 5.3 presents the polynomial of degree 1, which was used to calibrate each sensor in this study.

In section 5.4 (In-shoe center of pressure), the nine pressure sensors were distributed on the four regions of the foot: heel, midfoot, forefoot, and toes region. The number of sensors is in accordance with the number of inputs in the present controller unit of our shoe-type measurement device. The number of pressure sensors is few compared to other manufactured in-shoe pressure measurement systems such as: ParoTec System (Paromed, Germany) with 24 or 36 measuring points [64], Pedar-X system (Novel, Germany) with 85 to 99 sensors [65], F-scan system (Tekscan, Co., Ltd) with 3.9 sensels®/[cm^2] [66] and FSA FT1020-InShoe Mat (Vista Medical, Canada) with 128 sensors [67].

The result of the Pearson correlation (PCC) in Table 5.5 shows that the PCC in the medio-lateral (ML) and anterior-posterior (AP) directions between force plate and in-shoe system were (0.64 ± 0.39) and (0.90 ± 0.08), which indicates that the AP correlation is higher than in the ML direction; these results are similar to those obtained by Debbi et al. with the Pedar-X system [60], and Chesnin et al. with the ParoTec sole

system [63]. This may be due to the different characteristics between pressure sensors and force plates as follows: in the force plate, the calculation of the origin of the ground reaction force vector included shear and normal forces; however, the pressure sensor only measures pressure due to the normal forces applied to the sensor surface.

The results of RMS error are (0.86±0.27) [cm] and (2.67±1.35) [cm] for ML and AP, respectively. Table 5.6 presents the comparison result among in-shoe pressure measurement systems compared with the force plate systems.

Table 5.6 The comparison of the CoP path RMS error and Pearson correlation (PCC) to the force plate using certain manufactured products, presented as (mean±standard deviation). ML stands for medio-lateral, AP stands for anterior-posterior.

In-shoe pressure	ML RMSE [cm]	AP RMSE [cm]	ML PCC	AP PCC	Undetected area
Pedar®-X [56]	0.16±0.14	0.61±0.29	0.91±0.09	0.99±0.01	Not reported
ParoTec® in-sole [59]	0.56±0.30	1.37±0.59	0.70	0.90	Not reported
In-shoe pressure system in this study	0.86±0.27	2.67±1.35	0.64±0.39	0.90±0.08	Available

By using a weighted pressure formula in Eq. (5-4) and (5-5), it was possible to estimate the CoP to some degree of accuracy. However, poor results were found in the RMS error of AP direction (*y*-axis); this result might have been caused by the undetected area (U*), as shown in Fig. 5.15. We presume that the limitation of instrumentation and experiment limitation might be the cause of the undetected area, such as: 1) the low sampling rate of the control unit (30 [Hz]) had not been able to manage the measurements during single limb stance, that is around 30/100 – 80/100 [s] based on the empirical data in this experiment; 2) the slipping motion between the socks and the in-sole pressure board while the subject walked; and 3) the effects of foot wobble during single limb support.

5.7 Limitation and Affordable Error

The results of calibration and implementation have succeeded in calculating the center of pressure. Despite this improvement, there were three limitations, as described in this subsection, while the last part of this subsection will present the affordable error explanation in this study.

The first limitation is the number of force sensors that were attached on the insole board. The nine sensors on each insole board were limited in presenting the details of the pressure of foot plantar, which refers to the limitation of the spatial sensitivity area of measurement. In the future, an increased rigorous measurement area needs to be provided by increasing the number of force sensors.

The second limitation is related to the characteristics of the FlexiForce sensor. The piezo resistive material had various disadvantages, including a nonlinear response to the temperature change. The present study did not include the self-calibration, regarding the change of temperature. This will be noted when using the sensor implementation and automatic calibration before measurements are taken in subsequent studies.

The third limitation is related to the sampling rate of the pressure sensor controlling unit. By using 30 [Hz] of sampling rate, the single limb support time was approximately 30/100 to 80/100 [s], resulting in 10 to 25 points of data. As the number of data points is assumed to be lower, therefore, this needs to be increased. Increasing the sampling rate to minimum 60 [Hz] in future studies might provide better results in avoiding undetected areas.

The affordable error of the in-shoe pressure system regarding the CoP measurement will be explained using the relation of CoP and CoM (center of mass) or body sway. Many studies related to balance measurement during single stance, while the force platform was used to measure the posture balance, such as one study by Nejc, et al. [70] and Hoogvliet et.al [71]. However, the single stance phase in gait is different from single stance measurement in posture balance; this is because there is the effect of velocity in walking. The following two studies will support the relation between CoP and CoM: 1) the study by Schepers et al. [72] explains the estimation of CoM from CoP; some methods were introduced, such as: double integration of ground reaction force, the CoP low-pass filter method, and the fusion between CoP trajectory and CoM acceleration. Those method introduced by Schepers et al. showed that there is a relation between CoP and CoM during walking; 2) the other study by Hasan et al. [73] drew a conclusion that the amplitude and frequency between CoP and CoM were correlated in double and single stance.

The study by Orendurff et al. [74], explained the effect of walking speed on CoM

displacement. The data from ten healthy subjects at self-selected walking speed showed the CoM mediolateral (ML) displacement is (3.29 ± 1.29) [cm]. Our CoP mediolateral measurement error is (0.86±0.27) [cm], the 0.86 [cm] is less than the standard deviation of CoM displacement that was reported in Orendurff et al. i.e.: 1.29 [cm]; the present error is acceptable and not so big influence to CoP monitoring in ML direction. However, in AP direction, the reported empirical walking CoM was not found during literature study; therefore we could not get the comparison, however, the effort to increase the accuracy is important in the future study by accessing the suggestion on the previous paragraphs.

5.8 Summary

In this chapter, the tactile force sensor was chosen in our shoe-type gait measurement device among load cells and pressure-indicating films, due to its flexibility form and acceptable range of accuracy to present the in-shoe CoP path. The calibration of sensors in order to curve fit between the pressure data and the applied force was executed using the first, second, and third polynomials; in the end, the first order of polynomials was chosen in the implementation.

Using a weighted pressure formula and coordinate system transformation, we have succeeded in measuring the validity of our in-shoe CoP system, in that the calibration of each sensor through the data processing method was properly managed. The results show that, throughout the detected area, the RMSE is below 1 [cm] in the medio-lateral direction and below 3 [cm] in the anterior-posterior direction. However, despite its simplicity, we conclude this study with some suggestions to improve the in-shoe pressure system: instrumentation issues must be considered, such as the sampling rate and the number of sensors of our in-shoe pressure system, in order to minimize the undetected areas and to increase the spatial sensitivity areas.

This page intentionally left blank

6. Conclusions and Future Direction

6.1 Conclusion

The information of gait, including spatial and temporal, are important for rehabilitation and other medical purposes. The three features of information for the medics have been achieved in this study, that is, attitude determination, step-length prediction, and foot pressure information.

In attitude determination, the roll and pitch angle was determined using a sensor fusion technique, such as the extended Kalman Filter. The proposed method to compensate external acceleration was used to modify the measurement noise covariance matrix in order to set the level of trustworthiness to the measurement. The set of tests includes one-direction, multi-directional, and walking test that have been conducted in this study. In all kind of tests, the proposed algorithm overpass the standard EKF as presented in Table 3.10 (one-direction test), Table 3.13 (multi directional test), and Table 3.14 (walking test). On comparing the proposed method to other methods in other studies, the proposed method displayed an advantage in the number of model parameter to be tuned and the number of parameterized spatial rotation. Despite its efficacy, in the multi-directional and walking test, the proposed method has moderate outcome compared to the other method in the study.

In the step-length prediction, all work in this scope begins at the ultrasonic sensor simulation in order to redesign the number, the position, and the angle of each ultrasonic sensor. The result of simulation has been succeeded to implement in the actual shoe-type measurement device. The scope of measurement is 50x70 [cm], and it shows that the normal human step can be detected using this system. The step-length prediction is a fitting problem for abundant ultrasonic data that was solved using a two-layer neural network. The accuracy improvement has been achieved from the previous study as presented in Table 4.5.

In providing plantar center of pressure information, the tactile force sensor has been calibrated to the SI unit. The force sensors were very valuable regarding its shape and elasticity. The designed in-shoe pressure system has succeeded to measure plantar center of pressure. The validation has been done using the force plate system. However, increasing the system accuracy and decreasing the undetected area are the consideration for the future study by taking into account: 1) the limitation of instrumentation such as sampling rate; 2) increasing the number of sensor or using a tactile pressure sensor that contains matrix structure of the detection area might provide better results.

6.2 Future Direction

Separate data from three main sensors system was collected to provide information about gait parameters; however, the principal area about complete gait analysis was not addressed in this dissertation. The existence of an estimator, such as the Kalman filter, could be utilized to conduct correspondence problems in future studies.

The existence of the external acceleration model is possible to reduce the effects of disturbances while walking. Another consideration that might provide better results is using both a gyro and an accelerometer as a measurement model in an extended Kalman filter, rather than using the accelerometer only. Furthermore, using the direction cosine matrix, rather than the Euler representation, in order to avoid the first order approximation error in the process model might provide better estimation results.

Given the successful method in step-length prediction, the next step would be to find another spatial parameter of gait other than step-length, such as foot progression angle from ultrasonic sensor data. The capability of artificial neural networks in real-time application while walking has been proven in this study. Conducting studies about different artificial neural network architecture might provide better computational time in subsequent studies. The other issue is the trajectory or distance between feet in the swing phase; the capability of Kalman filter in fusing many sensors is possible to be used in combining ultrasonic data and IMU sensor data to be used in predict the foot trajectory during swing phase.

Another issue in presenting the plantar center of pressure is the number of pressure sensors distributed on the in-shoe sole. Increasing the number of sensors and increasing the sampling rate of acquisition program is an important consideration for future developments. Increasing the number of sensors might provide better accuracy, and increasing the sampling rate would reduce the undetected area, as well.

A trivial, but important, issue regarding user comfort while walking is the weight of the shoe-type gait measurement device. Lightweight materials need to be sought for further development, especially to replace the present material for the sole of the shoe.

It is my sincere hope that this work will provide the foundation for using estimators and artificial intelligence machine learning in processing data for gait parameters information and gait analysis in future studies.

References

[1] C. Wada, D. Takigawa, F. Wada, K. Hachisuka, T. Ienaga, and Y. Kimuro, "Improvement Research of Shoe-Type Measurement Device for a Walking Rehabilitation Support System," in *Cross-Cultural Design. Cultural Differences in Everyday Life*, vol. 8024, pp. 157-164, P.L.P. Rau, Eds. Springer Berlin Heidelberg, 2013.

[2] S.J.M. Bamberg, A.Y. Benbasat, D.M. Scarborough, D.E. Krebs and J.A. Paradiso, "Gait Analysis using a Shoe-Integrated Wireless Sensor System," in *IEEE Transactions on Information Technology in Biomedicine*, vol. 12, no. 4, pp. 413-423, 2008. doi: 10.1109/TITB.2007.899493.

[3] Y. Huang; W. Jirattigalachote; M. Cutkosky; X. Zhu; P. Shull, "Novel Foot Progression Angle Algorithm Estimation via Foot-Worn, Magneto-Inertial Sensing," in *IEEE Transactions on Biomedical Engineering* , vol. 63, no. 11, pp. 2278-2285. doi: 10.1109/TBME.2016.2523512.

[4] B. Mariani, M.C. Jiménez, F.J.G. Vingerhoets and K. Aminian, "On-Shoe Wearable Sensors for Gait and Turning Assessment of Patients With Parkinson's Disease," in *IEEE Transactions on Biomedical Engineering*, vol. 60, no. 1, pp. 155-158, 2013. doi: 10.1109/TBME.2012.2227317.

[5] K. Jahn, A. Zwergal, and R. Schniepp, “Gait Disturbances in Old Age: Classification, Diagnosis, and Treatment from a Neurological Perspective,” in *Medicine*, vol. 107, no. 17, pp. 306-316, 2010.

[6] D.C. Kerrigan, M.K. Todd, U.D. Croce, L.A. Lipsitz, and J.J. Collins, “Biomechanical Gait Alterations Independent of Speed in the Healthy Elderly: Evidence for Specific Limiting Impairments,” in *Arch Phys Med Rehabil*, vol. 79, March, pp. 317-322, 1998.

[7] A.H. Snijders, B.P. van de Warrenburg, N. Giladi, and B.R. Bloem, “Neurological Gait Disorders in Elderly People: Clinical Approach and Classification,” in *The Lancet Neurology*, vol. 7, no. 1, pp. 63-74, 2007.

[8] C. Alvarez, M.D. Vera, R. Beauchamp, V. Ward, and A. Black, “Classification of Idiopathic Toe Walking Based on Gait Analysis: Development and Application of the ITW Severity Classification,” in *Gait & Posture*, vol. 26, pp. 428-435, 2007.

[9] C. Kirtley, *Clinical Gait Analysis: Theory and Practice,* Elsevier Churchill Livingstone, China, 2006.

[10] Y.S. Suh, S.K. Park, H.J. Kang, and Y.S. Ro, "Attitude Estimation Adaptively

Compensating External Acceleration," in *JSME International Journal Series C*, vol. 49, no. 1, pp. 172–179, 2006.

[11] Y.S. Suh, "Orientation Estimation using a Quaternion-Based Indirect Kalman Filter with Adaptive Estimation of External Acceleration," in *IEEE Trans. on Instrumentation and Measurement*, vol. 59, no. 12, pp. 3296–3304, 2010.

[12] J.K. Lee, E.J. Park, and S.N. Robinovitch, "Estimation of Attitude and External Acceleration using Inertial Sensor Measurement during Various Dynamic Conditions," in *IEEE Trans. on Instrumentation and Measurement*, vol. 61, no. 8, pp. 2262–2272, 2012.

[13] H.J. Luinge and P.H. Veltink, "Measuring Orientation of Human Body Segments using Miniature Gyroscopes and Accelerometers," in *Medical & Biological Engineering & Computing*, vol. 43, pp. 273–282, 2005.

[14] P.D. Groves, *Principles of GNSS, Inertial, and Multisensor Integrated Navigation Systems*, Second Edition, Artech House (Horizon House Publications, Inc.), London, 2013.

[15] S. Romaniuk and Z. Gosiewski, "Kalman Filter Realization for Orientation and Position Estimation on Dedicated Processor," in *Acta Mechanica et Automatica*, vol. 8, no. 2, pp. 88–94, 2014.

[16] A.M. Sabatini, "Quaternion-Based Extended Kalman Filter for Determining Orientation by Inertial and Magnetic Sensing," in *IEEE Trans. on Biomedical Engineering*, vol. 53, no. 7, pp. 1346–1356, 2006.

[17] T. Harada, T. Mori, and T. Sato, "Development of a Tiny Orientation Estimation Device to Operate Under Motion and Magnetic Disturbance," in *The International Journal of Robotics Research*, vol. 26, no. 6, pp. 547–559, 2007.

[18] R.B. Widodo, H. Edayoshi, and C. Wada, "Complementary Filter for Orientation Estimation: Adaptive Gain Based on Dynamic Acceleration and Its Change," in *IEEE SCIS & ISIS*, pp. 906–909, 2014.

[19] J. Calusdian, X. Yun, and E.R. Bachmann, "Adaptive-Gain Complementary Filter of Inertial and Magnetic Data for Orientation Estimation," in *IEEE Int. Conference on Robotics and Automation*, pp. 1916–1922, 2011.

[20] R.B. Widodo and C. Wada, "Attitude Estimation Using Kalman Filtering: External Acceleration Compensation Considerations," in *Journal of Sensors*, vol. 2016, Article ID 6943040, 24 pages, 2016. doi:10.1155/2016/6943040.

[21] R.B. Widodo and C. Wada, "Simulation of Ultrasonic Sensors in a Shoe-Type Measurement Device," in *Proc. of the SICE Annual Conference*, Tsukuba, pp. 1490-1493, 2016.

[22] R.B. Widodo and C. Wada, "Artificial Neural Network Based Step-Length Prediction Using Ultrasonic Sensors from Simulation to Implementation in Shoe-Type Measurement Device," in *Journal of Advanced Computational Intelligence and Intelligent Informatics*, vol. 21, no. 2, 2017.

[23] J.O. Nilsson, I. Skog, P. Händel, and K.V.S. Hari, "Foot-Mounted INS for Everybody - an Open-Source Embedded Implementation," in *IEEE/ION Position Location and Navigation Symposium*, pp. 140–145, 2012.

[24] T. Watanabe, H. Saito, E. Koike, and K. Nitta, "A Preliminary Test of Measurement of Joint Angles and Stride Length with Wireless Inertial Sensors for Wearable Gait Evaluation System," in *Computational Intelligence and Neuroscience*, vol. 2011, Article ID 975193, 12 pages, 2011. doi:10.1155/2011/975193.

[25] D. McGrath, B.R. Greene, C. Walsh, and B. Caulfield, "Estimation of Minimum Ground Clearance (MGC) using Body-Worn Inertial Sensors," in *Journal of Biomechanics*, vol. 44, no. 6, pp. 1083–1088, 2011.

[26] B. Mariani, H. Rouhani, X. Crevoisier, and K. Aminian, "Quantitative Estimation of Foot-Flat and Stance Phase of Gait using Foot-Worn Inertial Sensors," in *Gait & Posture*, vol. 37, pp. 229–234, 2013.

[27] A.M. Herran, B.G. Zapirain, and A.M. Zorrilla, "Gait Analysis Methods: An Overview of Wearable and Non-Wearable Systems, Highlighting Clinical Applications," in *Sensors*, vol. 14, pp. 3362–3394, 2014.

[28] F. Dadashi, B. Mariani, S. Rochat, C. J. Büla, B. Santos-Eggimann, and K. Aminian, "Gait and Foot Clearance Parameters Obtained using Shoe-Worn Inertial Sensors in a Large-Population Sample of Older Adults," in *Sensors*, vol. 14, pp. 443–457, 2014.

[29] N.H.Q. Phuong, H.J. Kang, Y.S. Suh, and Y.S. Ro, "A DCM Based Orientation Estimation Algorithm with an Inertial Measurement Unit and a Magnetic Compass," in *Journal of Universal Computer Science*, vol. 15, no. 4, pp. 859–876, 2009.

[30] P. Kim, *Rigid Body Dynamics for Beginner: Euler angles and Quaternions*, CreateSpace Independent Publishing Platform, ISBN: 1493598201, 2013.

[31] T.S. Yoo, S.K. Hong, H.M. Yoon, and S. Park, "Gain-Scheduled Complementary Filter Design for a MEMS Based Attitude and Heading Reference System," in *Sensors*, vol. 11, pp. 3816-3830, 2011.

[32] D. Gebre-Egziabher, R.C. Hayward, and J.D. Powell, "Design of Multisensory Attitude Determination Systems," in *IEEE Trans. on Aerospace and Electronic*

Systems, vol. 40, no. 2, pp. 627-648, 2004.

[33] P. Kim and L. Huh, *Kalman Filter for Beginners: with MATLAB Examples*, A-JIN Publishing, ISBN: 1463648359, 2011.

[34] M.S. Grewal and A.P. Andrews, *Kalman Filtering Theory and Practice Using MATLAB*, John Wiley & Sons, Hoboken, NJ, USA, 3rd edition, 2008.

[35] J.J.D'Azzo, C.H. Houpis, and S.N. Sheldon, *Linear Control System Analysis and Design with MATLAB*, Marcel Dekker, 5th edition, 2003.

[36] T. Ozyagcilar, *Implementing a Tilt-Compensated eCompass using Accelerometer and Magnetometer Sensors*, Application Note AN4248. Freescale Semiconductor, 2012.

[37] J.C.F. de Winter, "Using the Student's *t*-test with Extremely Small Sample Sizes," in *Practical Assessment, Research & Evaluation*, vol. 18, no. 10, pp. 1–12, 2013.

[38] J.J. LaViola, "A Comparison of Unscented and Extended Kalman Filtering for Estimating Quaternion Motion," in *American Control Conference* vol. 3, pp. 2435–2440, 2003.

[39] B. Mariani, C. Hoskovec, S. Rochat, C. Büla, J. Penders, and K. Aminian, "3D Gait Assessment in Young and Elderly Subjects using Foot-Worn Inertial Sensors," in *Journal of Biomechanics*, vol. 43, pp. 2999–3006, 2010.

[40] C. Wada, F. Wada, K. Hachisuka, T. Ienaga, Y. Kimuro, and T. Tsuji, "Improvement Study for Measurement Accuracy on Wireless Shoe-Type Measurement Device to Support Walking Rehabilitation," in *Proc. of Int. Conf. on Complex Medical Engineering*, pp. 471-474, 2012.

[41] S. Ikeda and C. Wada, "Estimation of Foot Placement during Walking by Particle Filter Method," in *The 28th Symposia of SICE Sensing Forum Measurement Division*, pp. 105-108, 2011. (in Japanese).

[42] B.E. Treeby and B.T. Cox, "k-Wave: MATLAB Toolbox for the Simulation and Reconstruction of Photoacoustic Wave Fields," in *Journal of Biomedical Optics,*" vol. 15, no. 2, pp. 21314-1 – 21314-12, 2010.

[43] B.E. Treeby, B.T. Cox, and J. Jaros, "k-Wave: A MATLAB Toolbox for the Time Domain Simulation of Acoustic Wave Fields," in *User Manual*, Ver. 1.0.0, 2012.

[44] Murata. Ultrasonic Sensors MA40 Series, Datasheet. URL: https://www.murata.com/en-eu/products/productdata/8797589274654 [accessed March 12, 2016]

[45] D.J. Magee, *Orthopedic Physical Assessment*, 6th edition, Elsevier Saunders Canada, 2014.

[46] C. Kirtley, *Clinical Gait Analysis: Theory and Practice*, Elsevier Churchill

Livingstone, China, 2006.

[47] D. Levine, J. Richards, and M.W. Whittle, *Gait Analysis*, 5th edition. Elsevier Churchill Livingstone, China, 2012.

[48] B. Abernethy, V. Kippers, S.J. Hanrahan, M.G. Pandy, A.M. McManus, and L. Mackinnon, *Biophysical Foundations of Human Movement*, 3rd edition. Human Kinetics, Macmillan Education, Australia, 2013.

[49] B. McCarthy, *Sound Systems: Design and Optimization*, 3rd edition, 2016.

[50] S. Walczak and N. Cerpa, "Heuristic Principles for the Design of Artificial Neural Networks," in *Information and Software Technology,*" vol. 41, pp. 107 – 117, 1999.

[51] T. Hastie, R. Tibshirani, and J. Friedman, "The Elements of Statistical Learning: Data Mining, Inference, and Prediction," 2nd edition, Springer, 2008.

[52] H. Yu and B.M. Wilamowski, *Levenberg-Marquardt Training*, Industrial Electronics Handbook, vol. 5, Intelligent Systems, 2nd edition, chapter 12, pp. 12-1 to 12-15, CRC Press 2011.

[53] P. Terrier, Q. Ladetto, B. Merminod, and Y. Schutz, "High-Precision Satellite Positioning System as a New Tool to Study the Biomechanics of Human Locomotion," in *Journal of Biomechanics*, vol. 33, issue 12, pp. 1717-1722, 2000. ISSN 0021-9290.

[54] Tekscan, "Comparison of Interface Pressure Measurement Options," 2016, URL: https://www.tekscan.com/resources/whitepaper/comparison-interface-pressure-measurement-options

[55] Tekscan, "FlexiForce Sensors User Manual, " 2008.

[56] J. Grampp, J. Willson, and T. Kernozek, "The Plantar Loading Variations to Uphill and Downhill Gradients During Treadmill Walking," in *Foot and Ankle International*, vol. 21, no. 3, 2000.

[57] A. Hadi, A. Razak, A. Zayegh, R.K. Begg, and Y. Wahab, "Foot Plantar Pressure Measurement System: A Review," in *Sensors*, vol. 12, pp. 9884-9912, 2012.

[58] L. Shu, T. Hua, Y. Wang, Q. Li, D.D. Feng and X.Tao, "In-Shoe Plantar Pressure Measurement and Analysis System Based on Fabric Pressure Sensing Array," in *IEEE Transactions on Information Technology in Biomedicine*, vol. 14, no. 3, pp. 767-775, 2010. doi: 10.1109/TITB.2009.2038904.

[59] J.H. Kim, J.W. Han, D.Y. Kim, and Y.S. Baek, "Design of a Walking Assistance Lower Limb Exoskeleton for Paraplegic Patients and Hardware Validation using CoP," in *International Journal of Advanced Robotic Systems*, vol 10, no. 2, pp. 1-13, 2013.

[60] E.M. Debbi, A. Wolf, Y. Goryachev, Z. Yizhar, E. Luger, R. Debi, and A. Haim,

"In-Shoe Center of Pressure: Indirect Force Plate vs. Direct Insole Measurement," in *The Foot*, vol. 22, pp. 269-275, 2012.

[61] D.G.E. Robertson, G.E. Caldwell, J. Hamill, G. Kamen, and S.N. Whittlesey, *Research Methods in Biomechanics,* Human Kinetics, 2014. ISBN: 0-7360-9340-0.

[62] M. Tokunaga, "Study of Estimating Sit-To-Stand Movement from Foot Plantar Pressure and Human Body Link Model," *Thesis*, Kyushu Institute of Technology (in Japanese), 2012.

[63] K.J. Chesnin, L.S. Silverstein, and M.P. Besser, "Comparison of an In-shoe Pressure Measurement Device to a Force Plate: Concurrent Validity of Center of Pressure Measurements," in *Gait and Posture*, vol 12, pp. 128-133, 2000.

[64] Paromed, "ParoTec High-Precision Foot Pressure Measurement System User Manual."

[65] Novel, "Pedar-x Mobile Pedography-User Manual."

[66] Tekscan, "In-Shoe Analysis System-User Manual."

[67] Vista Medical. FSA Foot Assessment Product Specifications: InShoe Mat FT1020. Available online: http://www.pressuremapping.com/ (accessed on 24 December 2016).

[68] N. Saade, "Whole-Body Vibration Transmission Barefoot and with Shoes in Athletes and Sedentary Individuals," *Thesis*, Concordia University, 2013.

[69] A.F.J. Abercromby, W.E. Amonette, C.S. Layne, B.K. McFarlin, M.R. Hinman, and W.H. Paloski, "Vibration Exposure and Biodynamic Responses during Whole-Body Vibration Training," in *Medicine & Science in Sports & Exercise*, pp. 1794-1800, 2007. doi: 10.1249/mss.0b013e3181238a0f.

[70] S. Nejc, R. Jernej, S. Loefler, and H. Kern, “Sensitivity of Body Sway Parameters during Quiet Standing to Manipulation of Support Surface Size,” in *Journal of Sports Science and Medicine*, vol. 9, pp. 431-438, 2010.

[71] P. Hoogvliet, W.A van Duyl, J.V. de Bakker, P.G.H. Mulder, and H.J. Stam, “A Model for the Relation between the Displacement of the Ankle and the Center of Pressure in the Frontal Plane, during One-leg Stance,” in *Gait & Posture*, vol. 6, pp. 39-49, 1996.

[72] H.M. Schepers, E.H.F. van Asseldonk, J.H. Buurke, and P.H. Veltink, “Ambulatory Estimation of Center of Mass Displacement during Walking,” in *IEEE Transactions on Biomedical Engineering*, vol. 56, no. 4, pp. 1189-1195, 2009. doi: 10.1109/TBME.2008.2011059.

[73] S.S. Hasan, D.W. Robin, D.C. Szurkus, D.H. Ashmead, S.W. Peterson, and R.G. Shiavi, “Simultaneous Measurement of Body Center of Pressure and Center of

Gravity during Upright Stance. Part II: Amplitude and Frequency Data" in *Gait & Posture*, vol. 4, pp. 11-20, 1996.

[74] M.S. Orendurff, A.D. Segal, and N.J. Kadel, "The Effect of Walking Speed on Center of Mass Displacement," in *Journal of Rehabilitation Research & Development,* vol. 41, no. 6A, pp. 829-834, 2004.

This page intentionally left blank